AD_____
(Leave blank)

Award Number: W81XWH-06-1-0235

TITLE: Automated Patient Positioning Guided by Cone-Beam CT for Prostate Radiotherapy

PRINCIPAL INVESTIGATOR: Ming Chao, Ph.D.

CONTRACTING ORGANIZATION: Stanford University
Stanford, CA 94305-5401

REPORT DATE: January 2009

TYPE OF REPORT: Final

PREPARED FOR: U.S. Army Medical Research and Materiel Command
Fort Detrick, Maryland 21702-5012

DISTRIBUTION STATEMENT: (Check one)

× Approved for public release; distribution unlimited

□ Distribution limited to U.S. Government agencies only; report contains proprietary information

The views, opinions and/or findings contained in this report are those of the author(s) and should not be construed as an official Department of the Army position, policy or decision unless so designated by other documentation.

REPORT DOCUMENTATION PAGE

Form Approved
OMB No. 0704-0188

1. REPORT DATE *(DD-MM-YYYY)*	2. REPORT TYPE	3. DATES COVERED *(From - To)*
31-01-2009	Final	1 JAN 2006 - 31 DEC 2008

4. TITLE AND SUBTITLE

Automated Patient Positioning Guided by Cone-Beam CT for Prostate Radiotherapy

5a. CONTRACT NUMBER

5b. GRANT NUMBER
W81XWH-06-1-0235

5c. PROGRAM ELEMENT NUMBER

6. AUTHOR(S)
Ming Chao, Ph.D.

Tianfang Li, Ph.D.

5d. PROJECT NUMBER

5e. TASK NUMBER

5f. WORK UNIT NUMBER

7. PERFORMING ORGANIZATION NAME(S) AND ADDRESS(ES)

Stanford University
875 Blake Wilbur Drive, Rm G200
Stanford, CA 94305

8. PERFORMING ORGANIZATION REPORT NUMBER

9. SPONSORING / MONITORING AGENCY NAME(S) AND ADDRESS(ES)
U.S. Army Medical Research And Materiel Command
504 Scott Street
Fort Detrick, MD 21702

10. SPONSOR/MONITOR'S ACRONYM(S)
USAMRMC

11. SPONSOR/MONITOR'S REPORT NUMBER(S)

12. DISTRIBUTION / AVAILABILITY STATEMENT
Approved for public release
Distribution unlimited

13. SUPPLEMENTARY NOTES

14. ABSTRACT

Target localization, especially for soft-tissue target such as prostate, is a big concern in cancer radiotherapy due to its possible non-rigid internal motion relative to bony structures or external landmarks. The prostate target localization could be potentially done more accurately with the aid of the on-board kV cone-beam CT (CBCT) imager. In this project the PI group developed a novel technique of automatic patient positioning for prostate cancer radiation therapy. A few important milestones have been achieved toward the goal of the project. These include: (1) developed and clinically implemented an automated patient positioning strategy and tested with phantom experiments; (2) developed image-to-projection deformable registration algorithm to improve the CBCT image quality by reducing the view-aliasing artifacts; (3) established a novel technique to enhance on-board cone-beam CT and to effectively reduce the radiation dose incurred in the scanning process; (4) developed an innovative narrow shell technique for better target localization and model the critical structure; (5) established the method for auto-propagation of contours from planning CT to CBCT based on feature based spline deformable registration. The data and experiences we accumulated in this project are well documented, and server as a good reference for effectively utilizing CBCT imager, and will definitely enhance the outlook of the onboard CBCT in guiding radiation therapy as a whole.

15. SUBJECT TERMS
Prostate Cancer

16. SECURITY CLASSIFICATION OF:			17. LIMITATION OF ABSTRACT	18. NUMBER OF PAGES	19a. NAME OF RESPONSIBLE PERSON
a. REPORT	b. ABSTRACT	c. THIS PAGE			Lei Xing
Unclassified	Unclassified	Unclassified	Unlimited	69	19b. TELEPHONE NUMBER *(include area code)* (650)498-7896

Table of Contents

INTRODUCTION

This postdoctoral traineeship grant (W81XWH-06-1-0235, entitled "Automated patient positioning guided by cone-beam CT (CBCT) for prostate radiotherapy") was awarded to Dr. Tianfang Li, the original principal investigator (PI) on January 1st, 2006. Dr. Tianfang Li left Stanford University and accepted a faculty position at the University of Texas Southwestern Medical Center at Dallas in the end of 2006. The award was transferred to the current PI, Ming Chao Ph.D. It took a few months for the transition paper work to complete. A no-cost-extension was filed to extend the period of the project for one year, namely, through December 31st, 2008. This is the final report for the entire funding period (January 1st, 2006 – December 31st, 2008).

The goal of this project is to develop a clinically practical technique for prostate patient positioning based on newly emerged CBCT on-board imaging system. Under the generous support from the U.S. Army Medical Research and Materiel Command (USAMRMC), the PIs have gained a tremendous amount of knowledge on prostate cancer and prostate cancer management. The support has also made it possible for the PIs to contribute significantly to prostate cancer research. A number of conference abstracts and peer-reviewed publications have been resulted from the support. In this report, the PIs' research activities in the funding years are summarized and the accomplishments of the proposed tasks in the Statement of Work are presented.

BODY

I. Introduction

Modern radiotherapy equipment is capable of delivering high precision conformal dose distributions to the target. However, how to precisely locate the target prior to each treatment fraction, especially for soft tissue, remains a problem, due to possible non-rigid internal motion relative to bony structures or external landmarks. For this reason, gold-seed implants have been often used, for example in prostate, to enhance the visibility of the target in the portal film or EPID (electronic portal image device) image. Recently, a new technology of kilo-voltage cone-beam CT (CBCT) has been integrated onboard with the linear accelerator treatment machine. Figure 1 shows a CBCT on-board imager on a Varian Trilogy™ system. Superior to the common approach based on the two orthogonal images provided by the mega-voltage EPID, CBCT can provide high-resolution three-dimensional (3D) information of the prostate and other pelvic structures[1]. Thus the prostate target localization could be potentially done more accurately with the aid of the on-board CBCT imager, even without using any implanted fiducials. However, in practice, there is currently still a general lack of efficient method to utilize the 3D CBCT images for accurate patient positioning. The two major inherent difficulties in the task of prostate localization are: (1) the inter-fraction organ motions are more pronounced at pelvis than other sites, due to the involuntary physiological motions

Figure 1. Varian Trilogy oncology system with on-board CBCT imager

of the involved organs (such as the rectum and bladder)[2, 3] (Appendices 5 and 6); (2) the prostate has relatively low contrast resolution in CT images, which is likely to cause more errors in target delineation or localization[4] (Appendices 1 and 2). Extensive efforts have been made in utilizing CBCT for prostate target positioning, for instance, to position the patient using bony landmarks. Since the prostate gland can move independently to the bony structures and its shape may change from time to time, this commonly used positioning technique results in large uncertainties in prostate targeting. Manually matching the prostate target is possible but it is very time consuming and will introduce significant inter/intra-operator uncertainties. The goal of this research project is to develop effective volumetric image guidance techniques to facilitate the patient positioning for prostate radiation therapy.

II. New Patient Positioning Technique

We have developed a novel automated patient positioning technique for prostate cancer patients using deformable image registration. The significant advantage of this technique over traditional method is two-fold. First, it accounts for the complex non-rigid motion of the soft-tissue organs; Secondly, it considers both the prostate target and the organs at risk (OARs) simultaneously, thus a better clinical decision can be made in term of balancing the displacements of the target and OARs. In brief, the method first registers the 3D CBCT image acquired in the treatment room, to the 3D planning CT image using B-Spline deformable model, so that a point-to-point correspondence for the patient over the time (the period from planning to treatment) or the "deformation field" can be established. The displacement of every point in the target and sensitive structures are subsequently calculated and used to determine the final couch shifts by a weighted sum[1].

We have verified our positioning technique using a Varian Trilogy™ system (Varian Medical Systems, Palo Alto, CA) installed in our clinic, which is equipped with a kilo-voltage CBCT imager (see Figure 1). To test the technique, we have also built a pelvis phantom consisting of bladder, prostate, rectum, and bony structures, as illustrated in Figure 2. The phantom was first scanned with a clinical CT (General Electric Medical Systems, Waukesha, WI), with which a four-field 3D conformal treatment plan was generated. After deformation, it was scanned again with both the regular CT and a The planning CT was acquired at 120 kV, 380 mA, 2.5mm slice thickness using helical mode, while the positioning CT (and CBCT) were acquired at 80 mA with other scan parameters kept the same. The position of the "prostate" target was then derived using these images by three different approaches, including the proposed one based on deformable registration, one based on bony anatomy alignment, and one based on minimizing CT-number difference (MCD) via rigid translation of the target[5].

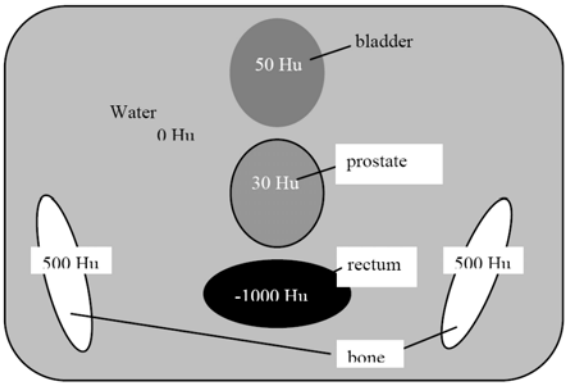

Figure 2. Schematic Drawing of a deformable pelvic phantom.

It was found that both the proposed and the MCD methods showed clear differences from bony anatomy alignment, reflecting the fact that the target had an internal motion independent to the bony structures. However, significant discrepancies were also observed between the proposed and the MCD methods, specifically, 12mm in x, 9mm in y, and 5mm in z axis in this study. Comparing Figures 3(a) and 3(b), we found that the proposed method presented much better accuracy for the target localization. In each of the two figures, positioning parameters were also calculated by using the regular CT images of the deformed phantom instead of CBCT, in which consistent results were achieved by the proposed one (see Figure 3b), while the MCD method generated different parameters (see Figure 3a). One of the reasons for MCD generating varied results when CBCT was replaced by clinical CT for positioning, is because that the clinical CT and the onboard CBCT have observable CT-number difference for the same tissue.

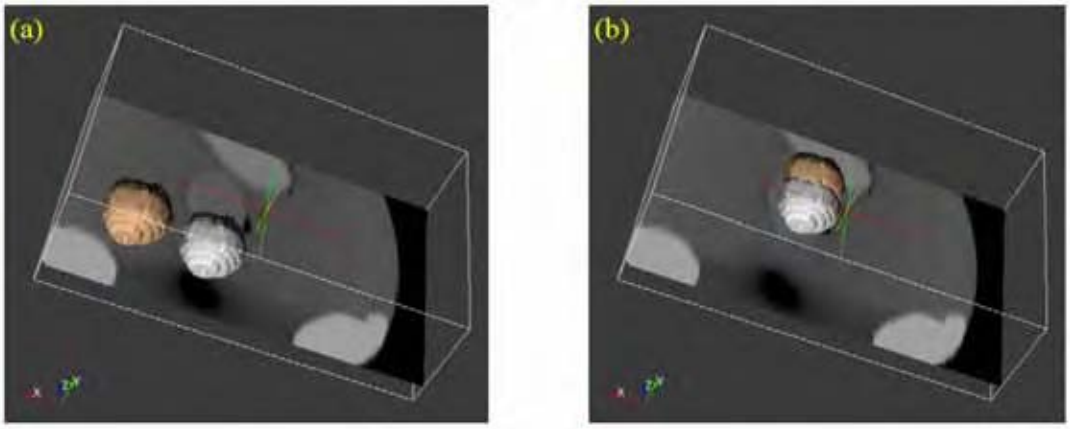

Figure 3. Positioning with (a) minimum CT-number difference and (b) deformable registration. The box outlines the volumetric image of the phantom in the treatment position. The color contour shows the same target after CBCT-guided repositioning, and the gray contour is the target after regular CT-guided repositioning. The CT-number difference between clinical CT and on-board CBCT resulted in discrepancy in the positioning parameters by this method.

The proposed registration-based CBCT repositioning is quite robust to noise and system errors of the imaging modalities. With this technique, the uncertainties of soft-tissue target localization could be greatly reduced, which ensures conformal dose distribution to be precisely delivered as planned. This will also enable the implementation of conformal radiotherapy for prostate tumor with much smaller margins than currently applied, leading to less complications and side effects and improved outcome of radiotherapy. The technique provides an outstanding opportunity for prostate dose escalation study.

III. Registration Technique Refinement

III.A Theoretical investigation

One of the most important issues of using CBCT images is to accurately register it with the planning CT image, which is not only essential to patient positioning, but also critical to various applications such as treatment planning and delivered dose verification or adaptive radiotherapy. Currently, the CBCT imaging system is far from being perfect.

Many image degrading factors such as the scatters, the beam hardening, and the approximate reconstruction algorithm etc, adversely affect the final image quality and may subsequently lead to inaccurate registration. Generally speaking, the CBCT 3D image is an artifacts-contaminated image compared with the diagnostic CT image. To improve the registration accuracy, we have been investigating a novel image space-to-projection space registration technique. The method has been validated with computer simulation, and the clinical study is under progress.

Since the reconstruction process often complicates the property of various artifacts, we may avoid the drawback of using low-quality reconstructed image in deriving the motion model by registering the 3D planning CT directly to the CBCT raw data. The unique problem with this method is that the two images being registered are in different spaces, *i.e.* one in the image domain, and the other in the projection domain. We have developed an efficient algorithm for such a registration task using a BSpline model, and one example of the advantage of such method is shown in Figure 4.

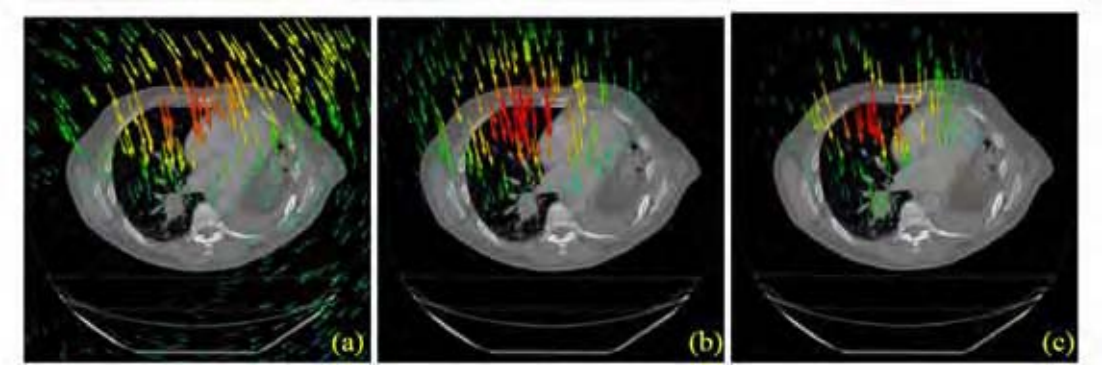

Figure 4. Deformation field resulted from different registration technique. (a) direct CT to CBCT image registration, where view-aliasing artifacts causes the registration error; (b) CT image to CBCT raw data registration; (c) true deformation field.

III.B Refinement of image registration technique

The novel automated patient positioning technique was developed for prostate cancer patients using deformable image registration. Compared to the conventional approach, the new technique accounts for the complex non-rigid motion of the soft-tissue organs and balances the prostate target and the organs at risk simultaneously. The method was verified using a pelvis phantom consisting of bladder, prostate, rectum and bony structures. We have further refined the registration technique and significantly improved the computational efficiency of the technique, thus making it possible for future clinical application. Briefly, our efforts were focused on improving the registration technique by using different similarity measures such as normalized cross correlation and mutual information (Appendices 1, 3, and 4). We found that by using the Mattes Mutual Information (MMI) metric, not only significant amount of computing time was saved, but also precision of the registration was achieved[2]. The central concept of mutual information (MI) is the calculation of entropy. For an image A, the entropy is defined as $H(A) = -\int p_A(a) \log p_A(a) da$, where $p_A(a)$ (also termed as marginal probability density function (PDF)) is the probability distribution of grey values (image intensities)

which is estimated by counting the number of times each grey value occurs in the image and dividing those numbers by the total number of occurrences. Given two images, A and B, their joint entropy is $H(A,B) = -\int\int p_{AB}(a,b)\log p_{AB}(a,b)dadb$, where $p_{AB}(a,b)$ is the joint PDF defined by a ratio between the number of grey values in the joint histogram (feature space) of two images and the total entries. The mutual information is generally expressed as $MI(A,B) = H(A) + H(B) - H(A,B)$. MI measures the level of information that a random variable (e.g., $\mathbf{I}_a(\mathbf{x})$) can predict about another random variable (e.g. $\mathbf{I}_b(\mathbf{x})$). Different from the conventional MI, where two separate intensity samples are drawn from the image, the Mattes implementation, MMI, uses only one set of intensity to evaluate both the marginal and joint PDFs at discrete positions or bins that uniformly spread within the dynamic range of the images[6]. Entropy values were computed by summing over all the bins. The introduction of the mutual information metric has showed significant improvement on the registration precision and helped reducing the impact of scatter and other factors inherent in CBCT imaging.

IV. Novel strategies of enhancing the quality of CBCT images

Onboard CBCT imaging plays an essential role in the success of prostate IMRT[7-9]. Unfortunately, the image quality of currently available CBCT is far from satisfactory due to a number of issues specific to the CBCT scan and image reconstruction. Factors that adversely affect the CBCT performance include scatter photons, motion artifacts, and excessive radiation dose. We were among the first in developing method to utilize the prior knowledge of the system to improve the resultant CBCT images. Generally, the patient has already had a planning CT (and possibly one or more CBCTs) before an on-treatment CBCT is acquired. These imaging data can be utilized as *a priori* knowledge to enhance the image quality and to reduce the radiation dose in routine CBCT imaging process. This has been successfully demonstrated in our previous studies on CT and PET imaging[10]. For CBCT imaging, due to the significantly reduced number of projections per reconstruction, the quality of the phase-resolved CBCT images is greatly degraded by the view-aliasing artifacts. Most commonly, acquisitions using multiple gantry rotations or slow gantry rotation can increase the number of projections and subsequently improve the image quality. However, the price to pay here is the significant increase of scanning time. Our CBCT image enhancement method effectively circumvent this problem through effective utilization of the information contained in other phases and/or even previously obtained planning CT (fan beam CT). By registering the prior data to the CBCT (in either image space or projection space), we were able to enhance the contrast-to-noise ratio (CNR) of the CBCT images by 5~10 fold, without noticeable compromise in the spatial resolution of the resultant images. The developed technique significantly reduces the view-aliasing artifacts in CBCT images and leads to high quality images for therapeutic guidance. This technique also dramatically decreases the radiation dose of CBCT acquisition. The image quality enhancement makes it possible to directly use CBCT for accurate dose calculation and IMRT planning.

In summary, along the direction of Task 4 in the Statement of Work, we have done substantial work on improving the performance of the CBCT system. We developed methods for enhancing the performance of CBCT and reducing radiation dose incurred during frequent CBCT scans[4, 11]. These accomplishments are attached in the Appendices (items 1 and 2), which conclude the task 4 in the Statement of Work.

V. Exploration of Low-Dose CBCT Imaging

Due to the repeated daily use of CBCT for a patient, the radiation exposure of the imaging system has been of great concern. For patient positioning purpose, the strategies to reduce the CBCT radiation exposure that we have developed during this training period are using the lowest possible x-ray tube current and low number of projections. The issues associated with low x-ray tube current is mainly the dramatically increased statistical noise, and with low number of projection, the undersampling (view-aliasing) artifacts become prominent in CBCT images. Apparently, simple reduction of the radiation dose results in bad image quality. In order to maintain an acceptable image quality or a minimal patient positioning error, we have proposed general CBCT enhancing techniques, which are based on the deformable registration of all available information (CT or CBCT images) of the same patient at different time. The extra information borrowed from other images helps to improve the statistics, and the data sampling rate as well. As one of the examples we have studied, in Figure 5 it is shown the improvement of our enhancing technique with low-dose CBCT acquisition strategy.

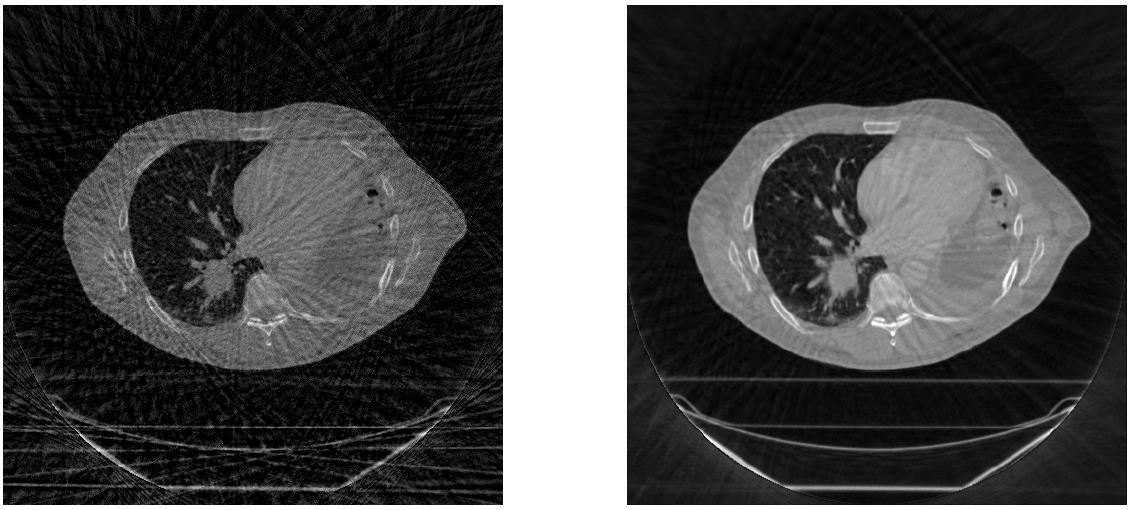

Figure5. Left: CBCT image with low number of projections showing under-sampling streak artifacts; Right: the improved CBCT image with our enhancing technique based on deformable registration.

VI. Contour propagation from planning CT to CBCT

Large interfraction organ motion exists in radiation therapy of pelvic diseases, such as prostate and cervical cancers. Adaptive therapy provides a viable option to ensure an adequate dose coverage of the tumor target while sparing the sensitive structures[12, 13]. Toward the general goal of more accurate patient positioning and clinically implementation of adaptive therapy of prostate cancer, we developed an effective regional contour mapping technique to automatically propagate rectum and prostate contours from planning CT to CBCT[2, 14-16] (Appendices 3, 4, 5, and 6). This effort is based on the precise deformable registration between planning CT and CBCT images. Different from disease sites, such as the lungs and liver, the contour mapping here in prostate radiation therapy is complicated by two factors: (i) the physical one-to-one correspondence may not exist due to the insertion or removal of some image contents within the rectum; and (ii) reduced signal to contrast ration of the CBCT images due to increased scatter in CBCT scanning. A solution customized to rectum mapping is

proposed to overcome the above two limitations and allow us to take advantage of the regional calculation algorithm yet avoiding the nuisance of rectum/bladder filling. The implementation of the contour propagation was achieved with the narrow shell technique. The shell was constructed outside the manually delineated contours on planning CT including the region of 1 ~ 2 cm. The central idea here is to exclude the volume inside the rectum because its content may change from day to day. Prostate contour can be mapped similarly, but the shell spans the regions both inside and outside the manually segmented prostate. Figure 6 illustrates the planning CT and the template contours for the ROIs such as prostate and rectum. Based on the narrow shell technique, various deformable models such as B-Spline and Thin Plate Spline models were employed to achieve the goal of contour propagation[17, 18]. A feature based model using the Scale Invariant Feature Transformation (SIFT) was also explored for higher registration accuracy[16, 19, 20] (Appendix 5). The mapped rectal contour is illustrated in Figure 7. This task was completed during the second funding period – one manuscript reporting the use of narrow shell based contour mapping strategy has been accepted by Physics in Medicine and Biology for publication. In addition, a paper reporting the use of SIFT method to auto-identify the tissue features for robust deformable registration and contour mapping in the pelvic region has been conditionally accepted by Medical Physics for publication (Appendices 5 and 6).

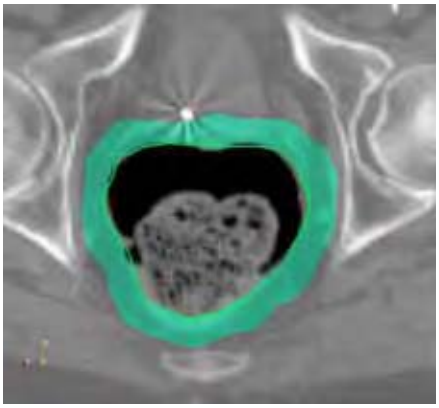

Figure 6. Narrow shell representation of regions of interest.

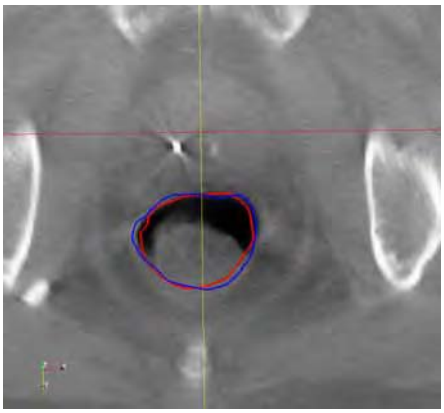

Figure 7. Mapped rectal contours (in red). Manual contour is overlaid (blue)

KEY RESEARCH ACCOMPLISHMENTS

- Developed a new image-to-projection deformable registration algorithm for CBCT/CT image matching, which is more accurate than conventional image-to-image registration method and more robust to various image artifacts such as view-aliasing or truncations (Task 1 of SOW).
- Developed and clinically implemented a novel automatic patient positioning strategy, which accounts for non-rigid organ motion, and balance the displacements of various organ structures (Task 2 of SOW).

- Improved the CBCT imaging quality and therefore made it possible to use low radiation dose CBCT for daily use, significantly reduced the risk of radiation-induced secondary cancer for patients (Task 4 of SOW).
- Established a novel technique to enhance on-board CBCT and to effectively reduce the radiation dose (Task 4 of SOW)
- Improved the registration technique by investigating various similarity measures including both the normalized cross correlation metric and the Mattes mutual information metric (Task 2 of SOW)
- Developed a novel technique of narrow shell representation of the regions of interest better target localization and critical structure modeling to account for the large inter-fraction (Task 3 of SOW)
- Established the framework of contour propagation from planning CT to CBCT based on the narrow shell technique for the adaptive prostate radiation therapy (Task 3 of SOW)

REPORTABLE OUTCOMES

The following is a list of publications resulted from the grant support. Copies of the publication materials are enclosed with this report.

Refereed Publications

The following is a list of peer reviewed publications.

- T. Li, A. Koong, L. Xing, "Enhanced 4D cone-beam CT with inter-phase motion model", *Medical Physics*, **34** 3688-3695, 2007
- T. Li, L. Xing, "Optimizing 4D cone-beam CT acquisition protocol for external beam radiotherapy", *International Journal of Radiation Oncology, Biology, Physics*, **67** 1211-1219, 2007
- M. Chao, E. Schreibmann, T. Li, N. Wink, L. Xing, "Automated contour mapping using sparse volume sampling for 4D radiation therapy", *Medical Physics*, **34** 4023-4029, 2007
- N. Wink, M. Chao, J. Antony, L. Xing, "Individualize treatment margin in respiration-gated radiation therapy", *Physics in Medicine and Biology*, **53** 165-175, 2008
- M. Chao, T. Li, E. Schreibmann, A. Koong, L. Xing, "Automated contour mapping with a regional deformable model", *International Journal of Radiation Oncology, Biology, Physics*, **70** 599-608, 2008
- Y. Xie, M. Chao, P. Lee, L. Xing, "Feature-based rectal contour propagation from planning CT to cone beam CT for adaptive radiotherapy", *Medical Physics*, **35** 4474-4487**,** 2008
- M. Chao, Y. Xie, L. Xing, "Auto-propagation of contours for adaptive prostate radiation therapy", *Physics in Medicine and Biology*, **53** 4533-4542, 2008

Published Abstracts

The PI's group has also been active in disseminating the research results. The following are some of the presentations given in various national and international conferences.

- T Li, E. Schreibmann, A. Koong, Q. Xu, R. Hamilton and L. Xing, "Verification of gated radiation therapy using pre-treatment 4D CBCT," International Journal of Radiation Oncology Biology Physics, **66**(3), S604, 2006.

- W. Mao, T. Li, P. Munro, M. Chao, and L. Xing, "Individualizing 4D CBCT acquisition protocol for external beam radiotherapy," International Journal of Radiation Oncology Biology Physics, **66**(3), S146-S147, 2006.
- L. Xing, A. de la Zerd, M. Cao, T. Li, B. Armbrush, Y. Yang, P. Lee, T. Pawlicki, S. Hancock and C. King, "On-Board Volumetric CT-based Adaptive IMRT For Improved Prostate Cancer Treatment," International Journal of Radiation Oncology Biology Physics, **66**(3), S624-S625 , 2006.
- M. Chao, E. Schreibmann, T. Li, A. Koong, K.A. Goodman and L. Xing, "Automatic Contouring in 4D Radiation Therapy," International Journal of Radiation Oncology Biology Physics, **66**(3), S649, 2006.
- E. Elder, E. Schreibmann, T. Li, T. Fox, L. Xing, J. Crocker and J. Landry, "Registration of 4D CBCT and 4D CT for Extracranial Stereotactic Treatments," International Journal of Radiation Oncology Biology Physics, **66**(3), S651, 2006.
- P. Peng, M. Chao, Q. Le, T. Li, A. Hsu, T.A. Pawlicki and L. Xing, "Auto Contour Mapping in CBCT for Adaptive Therapy Treatment Planning," International Journal of Radiation Oncology Biology Physics, **66**(3), S651-S652, 2006.
- T. Li, L Xing, P. Munro et al, "4D Cone-Beam CT (CBCT) Using An On-Board Imager," Med. Phys. **33**, 2234, 2006.
- M. Chao, T. Li, and L. Xing, "Enhanced 4D CBCT Imaging for Slow-Rotating On-Board Imager ," Med. Phys. **33**, 2269, 2006.
- M. Chao, E. Schreibmann, T. Li, and L. Xing, "Knowledge-Based Auto-Contouring in 4D Radiation Therapy," Med. Phys. **33**, 2171, 2006.
- M. Chao, E. Schreibmann, T. Li, and L. Xing, "Automatic Contour Mapping in 4D Radiation Therapy", Proceedings of the XVth International Confenrence on the Use of Computers in Radiation Therapy (ICCR), June 4-6, 2007, Toronto, Canada
- C. Wang, M. Chao, L. Xing, "Electron density mapping for MRI-based treatment planning", *Medical Physics* **34**, 2592, 2007
- T Li, L Papiez, R Timmerman, H Choy, A Koong, L Xing, "High-Quality Four-Dimensional CBCT Reconstruction with Virtual Projections**",** *Medical Physics* **34**, 2638, 2007
- M. Chao, E. Schreibmann, T. Li, L. Xing, "Automated propagation of region-of-interest contours between 4DCT Images using a regional deformable model", *Medical Physics* **34**, 2515, 2007
- N. Wink, M. Chao, L. Xing, "Individualized gating windows based on four-dimensional CT information for respiration gated radiotherapy", *Medical Physics* **34**, 2384, 2007
- M. Chao, L. Xing, "Auto-recontouring of CBCT images for adaptive therapy", *Medical Physics* **34**, 2352, 2007
- A. de la Zerd, M. Chao, B. Armbrush, Y. Yang, S. Hancock, C. King, T. Li, L. Xing, "Adaptive IMRT for improved prostate cancer treatment", Proceedings of the U.S. Department of Defense (DOD) Prostate Cancer Research Program (PCRP) Innovative Minds in Prostate Cancer Today (IMPaCT) meeting, September 5 – 8, 2007, Atlanta, Georgia
- M. Chao, Y. Xie, Q. Le, L. Xing, "Modeling the volumetric change of head and neck tumor in response to radiation therapy", *International Journal of Radiation Oncology * Biology * Physics*, **69**(3), S741, 2007
- T. La, M. Chao, L. Xing, Q. Le, "Evaluation of intrafraction motion in head and neck cancer during radiotherapy", *International Journal of Radiation Oncology * Biology * Physics*, **69**(3), S681 – S682, 2007

- L. Xing, L. Lee, M. Chao, P. Keall, T. La and Q. Le, "Clinical implementation of on-board CBCT-based adaptive IMRT for head and neck cancer", *International Journal of Radiation Oncology * Biology * Physics*, **69**(3), S446, 2007
- J. Wang, M. Chao, L. Xing, "Toward clinical implementation of adaptive treatment planning: auto-propagation of contours from planning CT to cone beam CT", *International Journal of Radiation Oncology * Biology * Physics*, **69**(3), S43, 2007
- L. Chen, M. Chao, Y. Xie, L. Xing, "Tumor shrinkage modeling: towards adaptive radiation therapy for head and neck cancer", *International Journal of Radiation Oncology * Biology * Physics*, **72**(1), S598, 2008
- Y. Xie, M. Chao, L. Xing, "Modeling the deformation and sliding motion of lungs", *International Journal of Radiation Oncology * Biology * Physics*, **72**(1), S620, 2008
- M. Chao, L. Lee, L. Xing, "Functional lung sparing using 4D-CT and intensity-modulated radiation therapy", *International Journal of Radiation Oncology * Biology * Physics*, **72**(1), S621, 2008
- J. Antony, G. Luxton, L. Lee, M. Chao, D. Carlson, L. Xing, "Biological modeling indices for 4D radiation therapy", *International Journal of Radiation Oncology * Biology * Physics*, **72**(1), S629, 2008
- M. Chao, Y. Xie, L. Xing, "Image-based modeling of tumor shrinkage or growth: towards adaptive radiation therapy of head-n-neck cancer", *Medical Physics* **35**, 2924 (2008)
- M. Chao, L. Xing, "Functional lung preservation using four-dimensional computed tomography and intensity-modulated radiation therapy for lung cancer", *Medical Physics* **35**, 2701, 2008
- Y. Xie, M. Chao, L. Xing, "4D CT image-based modeling the deformation and sliding motion of lungs", *Medical Physics* **35**, 2914, 2008

CONCLUSIONS

Despite the well-appreciated fact that onboard CBCT system can provide 3D anatomical information of a patient in the treatment position, its clinical applications have been hindered by the deficiencies in image quantitative accuracy and by the lack of a comprehensive image analysis procedure. This is evidenced by that very few institutions are using CBCT routinely for prostate cancer treatment. A challenge here is how to achieve automatic and accurate patient positioning with consideration of the non-rigid motions of the prostate and surrounding structures.

During the funding years, the PIs have contributed greatly to development of novel prostate cancer patient positioning technique. They have also gained improved knowledge on prostate cancer and prostate radiation therapy treatment. Various factors affecting the final positioning decisions are addressed. A few important milestones have been achieved toward the goal of the project. These include: (1) developed and clinically implemented an automated patient positioning strategy and tested with phantom experiments; (2) developed image-to-projection deformable registration algorithm to improve the CBCT image quality by reducing the view-aliasing artifacts; (4) established a novel technique to enhance on-board CBCT and to effectively reduce the radiation dose incurred in the scanning process; (5) developed a robust registration model with improved metric function; (6) developed an innovative narrow shell technique for better

target localization and model the critical structure; and (7) Established the method for auto-propagation of contours from planning CT to CBCT based on feature based spline deformable registration. The data and experiences accumulated in this project are well documented, and serve as a good reference and guidance for effective use of volumetric CBCT imaging technology. The research improves volumetric image guided prostate radiation therapy and enhances the outlook of the onboard CBCT in clinical practice as a whole.

The DOD Postdoctoral Training Award not only helped the PIs focus their efforts in the field of radiation therapy of prostate cancer, but it also provided them opportunities to obtain better understanding and gain significant experiences in prostate cancer research and substantially promoted their career development in the area. Under the outstanding mentorship of Professor Lei Xing, both PIs were successful in their careers. The initial PI, Dr. Tianfang Li was offered a tenure track assistant professor position at the University of Texas Southwestern Medical Center at Dallas in late 2006. The successor of the Award, Dr. Ming Chao, was appointed assistant professorship at the University of Arkansas for Medical Sciences in 2008. The prostate research program was very successful in training junior researchers and helping them achieve their career goal in prostate research.

REFRENCES

1. Xing L, Thorndyke B, Schreibmann E, *et al.* Overview of image-guided radiation therapy. *Med Dosim* 2006;31:91-112.
2. Chao M, Li T, Schreibmann E, *et al.* Automated contour mapping with a regional deformable model. *Int J Radiat Oncol Biol Phys* 2008;70:599-608.
3. Xie Y, Chao M, Lee P, *et al.* Feature-based rectal contour propagation from planning CT to cone beam CT. *Med Phys* 2008;35:4450-4459.
4. Li T, Koong A, Xing L. Enhanced 4D cone-beam CT with inter-phase motion model. *Med Phys* 2007;34:3688-3695.
5. Berbeco RI, Jiang SB, Sharp GC, *et al.* Integrated radiotherapy imaging system (IRIS): design considerations of tumour tracking with linac gantry-mounted diagnostic x-ray systems with flat-panel detectors. *Phys Med Biol* 2004;49:243-255.
6. Mattes D, Haynor DR, Vesselle H, *et al.* Non-rigid multi-modality image registration. *Medical Imaging 2001: Image Processing* 2001:1609-1620.
7. Xing L, de la Zerd A, Chao M, *et al.* On-board volumetric CT-based adaptive IMRT for improved prostate cancer treatment. *Int J Radiat Oncol Biol Phys* 2006;66:S624-S625.
8. Yang Y, Schreibmann E, Li T, *et al.* Evaluation of on-board kV cone beam CT (CBCT)-based dose calculation. *Phys Med Biol* 2007;52:685-705.
9. Lee L, Le QT, Xing L. Retrospective IMRT dose reconstruction based on cone-beam CT and MLC log-file. *Int J Radiat Oncol Biol Phys* 2008;70:634-644.
10. Li T, Schreibmann E, Thorndyke B, *et al.* Radiation dose reduction in four-dimensional computed tomography. *Med Phys* 2005;32:3650-3660.
11. Li T, Xing L. Optimizing 4D cone-beam CT acquisition protocol for external beam radiotherapy. *Int J Radiat Oncol Biol Phys* 2007;67:1211-1219.

12. Oldham M, Letourneau D, Watt L, *et al.* Cone-beam-CT guided radiation therapy: A model for on-line application. *Radiother Oncol* 2005;75:271-278.
13. Court LE, Dong L, Lee AK, *et al.* An automatic CT-guided adaptive radiation therapy technique by online modification of multileaf collimator leaf positions for prostate cancer. *Int J Radiat Oncol Biol Phys* 2005;62:154-163.
14. Chao M, Schreibmann E, Li T, *et al.* Automated contour mapping using sparse volume sampling for 4D radiation therapy. *Med Phys* 2007;34:4023-4029.
15. Chao M, Xie Y, Xing L. Auto-propagation of contours for adaptive prostate radiation therapy. *Physics in Medicine and Biology* 2008:submitted.
16. Xie Y, Chao M, Lee P, *et al.* Feature-based rectal contour propagation from planning CT to cone beam CT for adaptive radiotherapy. *Med Phys* 2008:conditionally accepted.
17. Schreibmann E, Xing L. Narrow band deformable registration of prostate magnetic resonance imaging, magnetic resonance spectroscopic imaging, and computed tomography studies. *Int J Radiat Oncol Biol Phys* 2005;62:595-605.
18. Schreibmann E, Chen GT, Xing L. Image interpolation in 4D CT using a BSpline deformable registration model. *Int J Radiat Oncol Biol Phys* 2006;64:1537-1550.
19. Lowe DG. Object recognition from local scale-invariant features. Proceedings of International Conference on Computer Vision; 1999. pp. 1150-1157.
20. Bookstein FL. Thin plate splines and the decomposition of deformations. *IEEE Trans. Pattern Anal Mach Intell* 1989;11:567-585.

APPENDICES: MANUSCRIPTS PUBLISHED

1. T. Li, A. Koong, L. Xing, "Enhanced 4D cone-beam CT with inter-phase motion model", *Medical Physics*, **34** 3688-3695, 2007
2. T. Li, L. Xing, "Optimizing 4D cone-beam CT acquisition protocol for external beam radiotherapy", *International Journal of Radiation Oncology, Biology, Physics*, **67** 1211-1219, 2007
3. M. Chao, E. Schreibmann, T. Li, N. Wink, L. Xing, "Automated contour mapping using sparse volume sampling for 4D radiation therapy", *Medical Physics*, **34** 4023-4029, 2007
4. M. Chao, T. Li, E. Schreibmann, A. Koong, L. Xing, "Automated contour mapping with a regional deformable model", *International Journal of Radiation Oncology, Biology, Physics*, **70** 599-608, 2008
5. Y. Xie, M. Chao, P. Lee, L. Xing, "Feature-based rectal contour propagation from planning CT to cone beam CT for adaptive radiotherapy", submitted to *Medical Physics*, **35** 4474-448**7,** 2008
6. M. Chao, Y. Xie, L. Xing, "Auto-propagation of contours for adaptive prostate radiation therapy", *Physics in Medicine and Biology*, **53** 4533-4542, 2008

Enhanced 4D cone-beam CT with inter-phase motion model

Tianfang Li, Albert Koong, and Lei Xing[a)]
Department of Radiation Oncology, Stanford University School of Medicine, Clinical Cancer Center, 875 Blake Wilbur Drive, Stanford, California 94305-5847

(Received 9 November 2006; revised 6 July 2007; accepted for publication 9 July 2007; published 27 August 2007)

Four-dimensional (4D) cone-beam CT (CBCT) is commonly obtained by respiratory phase binning of the projections, followed by independent reconstructions of the rebinned data in each phase bin. Due to the significantly reduced number of projections per reconstruction, the quality of the 4DCBCT images is often degraded by view-aliasing artifacts easily seen in the axial view. Acquisitions using multiple gantry rotations or slow gantry rotation can increase the number of projections and substantially improve the 4D images. However, the extra cost of the scan time may set fundamental limits to their applications in clinics. Improving the trade-off between image quality and scan time is the key to making 4D onboard imaging practical and more useful. In this article, we present a novel technique toward high-quality 4DCBCT imaging without prolonging the acquisition time, referred to as the "enhanced 4DCBCT". The method correlates the data in different phase bins and integrates the internal motion into the 4DCBCT image formulation. Several strategies of the motion derivation are discussed, and the resultant images are assessed with numerical simulations as well as a clinical case. © *2007 American Association of Physicists in Medicine*.
[DOI: 10.1118/1.2767144]

Key words: cone-beam, 4D CT, on-board imager, IGRT, organ motion

I. INTRODUCTION

Medical linear accelerators equipped with cone-beam CT (CBCT) imaging system, using either a kV or MV x-ray source, have recently become available in clinics. The volumetric image provided by CBCT opens new avenues for patient setup, dose verification, and online treatment planning.[1–12] These applications rely highly upon the fidelity and quality of the CBCT images. When imaging in the region of thorax and upper abdomen, however, respiration induced artifacts, such as blurring, doubling, streaking, and distortion are observed, which heavily degrade the image quality and affect the target localization ability and the accuracy of the dose calculation.[13,14]

A recently proposed method to account for respiratory motion during CBCT imaging is called "respiration correlated CBCT" or four-dimensional (4D) CBCT.[15–18] In this method, the CBCT projections are divided into several groups according to their respiratory phases. Each phase group is then reconstructed independently to yield a volumetric image corresponding to that specific phase. Since the selected projections in each group have almost the same phase, the method greatly reduces the motion-induced inconsistency among the data, leading to improved image reconstruction. However, the number of projections available for each image reconstruction is substantially decreased compared to a conventional 3D CBCT due to the data dividing. This may lead to a serious undersampling problem and result in strong view-aliasing artifacts in the phase-resolved images. The artifacts are generated during the backprojection step in the CBCT image reconstruction process and are seen mainly in the 2D axial planes.

To eliminate the view-aliasing artifacts in 4DCBCT, we have recently investigated acquisition techniques of "multiple gantry rotation" and "slow gantry rotation" with low x-ray tube current.[16,17] These methods increase the number of projections of each phase and significantly improve the 4DCBCT image quality. However a practical issue is the prolonged acquisition time, which may limit their clinical applications.

The purpose of this work is to investigate a novel approach to reduce the acquisition time while maintaining the 4DCBCT image quality, or from another point of view, to enhance the current 4DCBCT image quality while using short acquisition time. The approach developed in this article is essentially to reduce the view-aliasing artifacts resulted from insufficient sampling. To increase the sampling rate in each individual phase, the projections of all other phases can be incorporated into the reconstruction process. To do so, a motion model linking the data of different phases is required, which can be derived from deformable registrations of the 4DCBCT phases. Two other registration strategies of introducing an additional diagnostic CT image and mapping between image space and projection space are also investigated. The proposed approach is evaluated with numerical simulations. Since the view-aliasing artifacts are prominent only in the axial view and for simplicity, we start with fan-beam (2D) geometry to study the performance of the approach, a clinical case of a lung cancer patient is then presented.

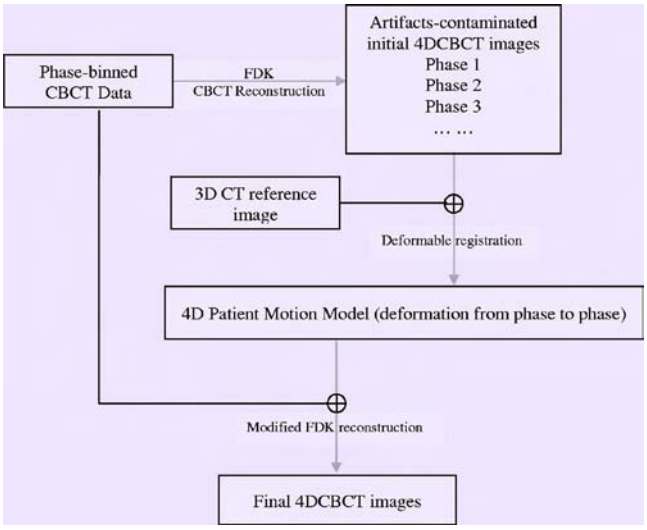

FIG. 1. Flow chart of the proposed reconstruction process for enhanced 4DCBCT imaging.

II. METHODS AND MATERIALS

II.A. Modified Feldkamp reconstruction for reduced view-aliasing artifacts

As described earlier, to form the 4DCBCT images, the acquired projection data are retrospectively sorted into several phase bins before reconstructions. When the acquisition time is limited, the reduced number of projections per reconstruction will result in undersampling and degrade the image with view-aliasing artifacts. In order to improve the sampling rate in each phase, we need to borrow projection information from other phases. Obviously, direct inclusion of projections of other phases will cause the inconsistency in the data due to patient motion. However, as we have shown previously, if the motion can be accurately modeled, a motion-corrected CBCT reconstruction can be obtained.[19] This reconstruction method is a modified Feldkamp algorithm, which performs the backprojections of the filtered data along deformed paths according to the corresponding motion model. Equivalently and computationally more efficiently, one can reconstruct each individual phase first, then superimpose all the phases after deforming each of them into the same phase based on the given motion model. This method can be described in the following flow chart (Fig. 1).

II.B. Motion model estimation

To derive the motion model (i.e., the points of correspondence between any two phases) to be used in the enhanced 4DCBCT reconstruction, we have investigated the following three registration strategies with and without the aid of an additional 3D CT image.

II.B.1. Register artifacts-contaminated 4DCBCT images

The most straightforward way to find the motion model is to register the regular 4DCBCT phases using a deformable model. A unique problem here is that the images to be registered contain serious steak artifacts, which may adversely affect the accuracy of the derived motion model, and the error can propagate into the final 4DCBCT images. Nevertheless, the process may prove to be favorable because of greatly reduced view-aliasing artifacts. The performance of this method is shown later with a simulation study where the registration was done based on a free-form Spline (BSpline) model. The simplicity and yet accuracy of the BSpline method make it a preferred tool for many clinical applications.[20–25] More details about this registration algorithm can be found in Ref. 22.

II.B.2. Register planning CT to 4DCBCT phased image

Note that in radiation therapy, it is often the case that a patient has already had a 3D or 4D CT scan for the treatment planning before any radiation delivery. In such case, an artifact-free volumetric image can be assumed available prior to the 4DCBCT scan on the treatment day. Considering respiration motion, this CT image should be one phase of 4D CT images or a breath-hold CT scan. The idea is to register each phase of the 4DCBCT images to this artifact-free 3D image to derive corresponding deformation with respect to the specific phase of the CT image. The deformation of the 4DCBCT phases with respect to each other can be subsequently obtained by calculating the relative movements. Since only one of the two images being registered has artifacts, it is expected that the accuracy will be improved over the first procedure. Again, the performance of this method is evaluated with the simulation study later in this article.

II.B.3. Registration from image space to projection space

Although the reconstructed 4DCBCT phase images contain view-aliasing artifacts, one should realize that the artifacts are not originally present in the raw data but are generated later during the reconstruction process. Therefore, we may avoid the drawback of using a low-quality reconstructed image in deriving the motion model by registering the 3D planning CT directly to the CBCT raw data (after phase sorting). Note that the two images being registered are in different spaces; in the following, we present a simple algorithm for such a registration task using a BSpline model.

Similar to the conventional image registration using deformable models, the motion of the object is described by $g(\boldsymbol{x};t)=f(\boldsymbol{x}+\boldsymbol{u}(\boldsymbol{x};t))$, where $f(\boldsymbol{x})$ represents the 3D image obtained from the planning CT scan, $g(\boldsymbol{x};t)$ is the same object at a particular phase t during the 4DCBCT scan, and $\boldsymbol{u}(\boldsymbol{x};t)$ defines the corresponding deformation for point $\boldsymbol{x}$ at that phase. With the BSpline model, the deformation is defined on a sparse, regular grid of control points λ_n placed over the CT image. When a point is not on the grid, the associated deformation is calculated by the BSpline interpolation as follows:

$$\boldsymbol{u}(\boldsymbol{x};t)=\sum_n \theta_{n,t}\beta^{(3)}\left(\frac{\boldsymbol{x}-\lambda_n}{\Delta_x}\right), \quad (1)$$

where $\beta^{(3)}(\boldsymbol{x})=\beta^{(3)}(x)\beta^{(3)}(y)\beta^{(3)}(z)$ is a separable cubic BSpline convolution kernel, $\theta_{n,t}$ are the values for the control points at phase t, and Δ_x controls the grid spacing in each dimension.

To register the CBCT projections with the planning CT image, we adopt the metric of sum of squared difference,

$$\Phi(\boldsymbol{\theta})=\sum_i\left(Y_i-\sum_j A_{ij}g_j\right)^2=\sum_i\left(Y_i-\sum_j A_{ij}f_j(\boldsymbol{x}+\boldsymbol{u})\right)^2, \quad (2)$$

where Y_i is the total attenuation along the ith projection ray, j is the index of the image voxel, and A is the cone-beam projection matrix. For simplicity, the phase index t is neglected here. Given the projection data Y and planning CT image f, the deformation field $\boldsymbol{u}$ at a particular phase can be found by minimizing the above objective function. General-purpose algorithms can be applied to solve the optimization problem, and in this work the LBFSG algorithm is used,[26] which requires the calculation of the first derivative of the cost function Φ. It can be shown that Eq. (2) has a closed-form derivative that can be calculated explicitly. For a similar derivation, readers are referred to the original work by Zeng *et al.*,[27,28] of which the method B3 can be understood as a variation.

II.C. Simulation studies

The above model-based recontruction method is validated with numerical simulations under 2D fan-beam geometry and 3D cone-beam geometry. The parameters for the simulations are similar to the real setup of a Varian Trilogy machine (Varian Medical Systems, Palo Alto, CA), where the focal length of the fan beam or cone beam is 150 cm, and the radius of the detector rotation is 50 cm. The fan-beam simulation has 1024 samples spaced by 0.388 mm, and 2048 projection views were simulated with projection angles evenly spanned over 360°, while the cone-beam simulation consists of 1024×768 pixels in each of the total 1200 projections with a pixel size of 0.388 mm. The object used in the fan-beam simulations came from one slice of the CT images of a patient, which contained 512×512 pixels with the pixel size of 1.0 mm. For the cone-beam simulation, the 80 slices are used with slicethickness of 2.5 mm.

To include the effect of the respiratory-induced motion, we imposed an artificial perodically changing deformation field on the image during the simulations. Specifically, a maximum deformation is determined by registering the inhale and exhale phases of a patient 4DCT scan. The deformation of an intermediate phase is then obtained by linearly scaling down the maximum deformation field with a scaling factor $s=\cos^2(\pi t/T)$, where t is the acquisition time, and T is the respiration period. For the fan-beam case, the motion is restricted in the axial plane, while for the cone-beam geometry, the motion is fully 3D. The period of the simulated respiratory motion is 4 s. In reality, irregular patient respiration is possible, which may affect the accuracy of phase binning in 4DCBCT. However, this was not considered in our simulations because the focus of this paper is the reduction of the view-aliasing artifacts.

II.D. Patient study

A lung cancer patient had a multiple-gantry-rotation (MGR) 4DCBCT scan in our clinic, and his 4D images were used to evaluate our proposed approach. Due to the limit access of the available data, only the method described in Sec. 2.1.1 was tested. The 4DCBCT was acquired with a Trilogy system (Varian Medical Systems, Palo Alto, CA). For the MGR 4D scan, the x-ray tube current was set to 32 mA, and four gantry rotations were performed at a speed of 6°/s. Each rotation (slightly over 360°) consisted of over 680 projections, and the effective area of each acquired projection image was 397.312 mm $\times$ 297.984 mm, containing 1024×768 pixels. The average breathing cycle of the patient was 4.2 s. The 4DCBCT images were obtained by retrospective sorting of the MGR data into 6 phases and subsequently reconstructing the rebinned data. More details about this 4DCBCT technique can be found in Ref. 16. To evaluate the proposed 4D image enhancing method, the 4D phases were registered to the 0% phase with a BSpline deformable model and then superimposed. The resultant phase-0% image was then compared with the original 4DCBCT for several axial slices to demonstrate the differences.

III. RESULTS

III.A. Fan-beam simulation study

The fan-beam simulated projection data are shown in Figs. 2(a) and 2(b), where the left is from the static CT image and the right is from the same object with the artificial in-plane deformation. It is seen that the object motion during the scan generated a large amount of inconsistency in the projection data [Fig. 2(b)]. To show its effect on the resultant image, in Figs. 2(c) and 2(d), the corresponding reconstructed images are compared, where artifacts such as blurring, doubling, distortion, and streak artifacts are observed in the motion contaminated image [Fig. 2(d)].

The simulated projections of the continuously deformed image were retrospectively sorted into eight phases. Five of the reconstructed phases from the peak inspiration to the peak expiration are illustrated in Fig. 3(a), and a zoomed-in image of phase 1 is shown in Fig. 3(b). Compared with the reconstructed images in Figs. 2(c) and 2(d), it can be found that the motion blurring is greatly reduced, and the boundary of the primary tumor became much clearer after the phase sorting. However, some low contrast structures (for example the aorta, muscle, etc.) are lost due to the view-aliasing streak artifacts.

Three enhanced images using the proposed approach are shown in Fig. 4 corresponding to the three motion model derivation techniques. The top row in Fig. 4 shows the derived deformation between phase 1 and phase 4, where from the left to the right are using "4D phase-to-phase registra-

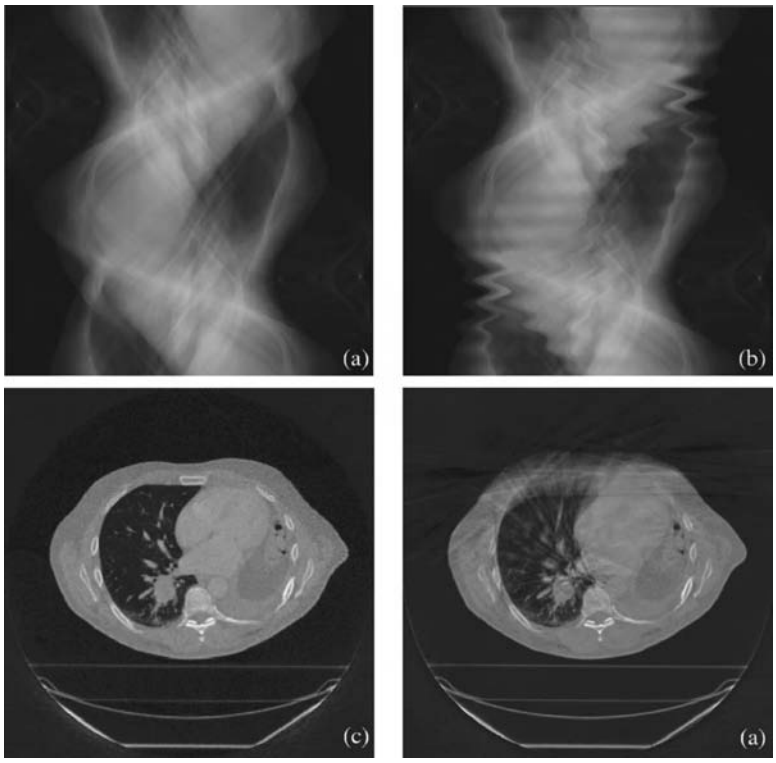

FIG. 2. Simulated projections and their corresponding reconstructed images. The left column is from the static object, and the right column is from the same object with artificial deformation.

tion" (method B1), "CT image to 4D phases" (method B2), and "CT image to CBCT projection" (method B3), respectively. The corresponding reconstructed images (at phase 1) are shown in the bottom row. We find no significant artifacts in the reconstructed image, even with certain errors in the derived motion model [see Fig. 4(a) the circular pattern in the deformation field due to registering CBCT images contaminated with view-aliasing artifacts]. The image enhancing approach using any of the three motion models improved the image quality over the regular phase-resolved image (Fig. 3), and the method as described in B3 by matching CT image with CBCT raw data generated the best final images (less streak artifacts near the boundary of the field of view), because a relatively more accurate motion model is applied.

In Figs. 5(a) and 5(b), we quantitatively compared the CBCT images by plotting vertical profiles passing through

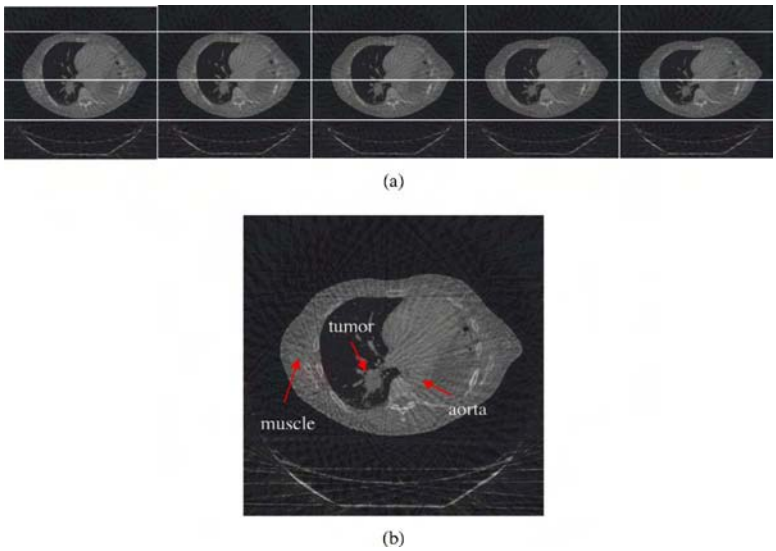

FIG. 3. (a) Five examples of the reconstructed phases after the phase sorting of the simulated projection data of the moving object; (b) a zoomed-in image of the first reconstructed phase where it is found that the motion blurring is reduced by phase binning, but some low-contrast structures are lost due to view-aliasing artifacts.

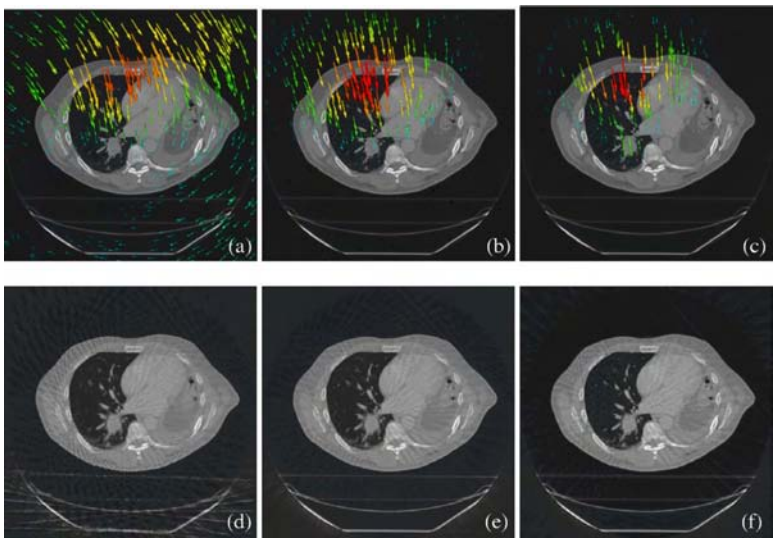

FIG. 4. Top row, from the left to the right, illustrates the derived deformation field obtained by using methods B1, B2, and B3, respectively, and the bottom row shows the corresponding reconstructed images for phase 1 using the proposed image enhancement technique.

the tumor. It is seen from Fig. 5(a) that the enhanced 4DCBCT (ED_4DCBCT) images resulted from three motion models have similar accuracy in terms of the CT numbers. The difference from the phantom (ground truth) is mainly due to the filtered backprojection reconstruction process. In Fig. 5(b), the enhanced 4DCBCT (using motion model B1) is compared with 3DCBCT and regular 4DCBCT. It can be seen that the ED_4DCBCT results in less noise (compared with regular 4DCBCT) while maintaining the correct tumor profile.

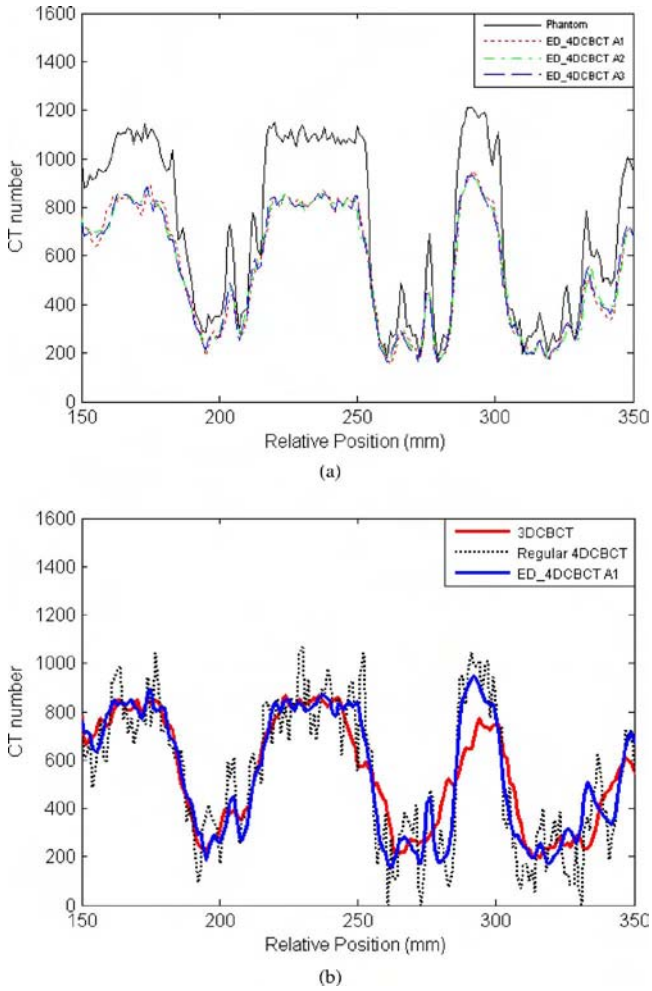

FIG. 5. Comparison of vertical profiles passing through the tumor.

Furthermore, the contrast-to-noise ratio (CNR) as an image metric is compared for the CBCT images, defined as $\mathrm{CNR}=|\langle S\rangle-\langle S_0\rangle|/\sigma$, where $\langle S\rangle$ and $\langle S_0\rangle$ denote the average signal within a region of interest for the tumor and soft tissue, respectively, and σ denotes the standard deviation within the tumor. The calculated CNR for regular 4DCBCT is 1.186; for enhanced 4DCBCT, the CNRs are 5.487, 5.584, and 5.589 for motion models B1, B2, and B3, respectively.

III.B. Cone-beam simulation study

Figure 6 shows the 4D cone-beam simulation results at respiratory phase 1. From the top to the bottom rows are the phantom images, the motion blurred 3DCBCT images, the regular 4DCBCT images, and the enhanced 4DCBCT images, respectively. From left column to the right column are the axial, coronal, and sagittal views. The motion model applied to the enhanced 4DCBCT image reconstruction was derived using method B2 by registering each phase of the regular 4DCBCT to the peak-inhale phantom images. Again, dramatic improvement [Fig. 6(d) over Fig. 6(c)] is observed by using the proposed approach for the cone-beam study. The CNRs for the regular 4DCBCT and the enhanced 4DCBCT are 0.92 and 4.43, respectively.

III.C. Patient study

The enhanced 4DCBCT images were obtained for the patient using the proposed approach and the motion model de-

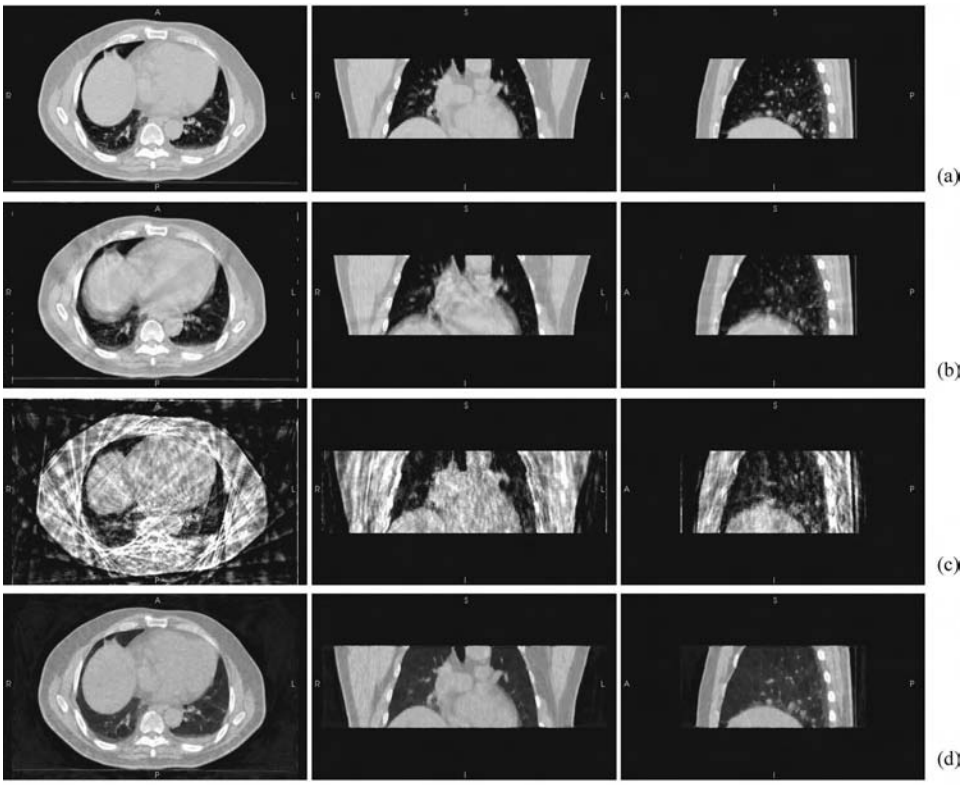

FIG. 6. Simulation study using cone-beam geometry. From left to right are the images of axial, coronal, and sagittal views, respectively. Row (a) shows the 4D phantom; row (b) is the 3DCBCT showing the motion blurring artifacts; row (c) is the regular 4DCBCT images showing the view-aliasing artifacts; and row (d) is the enhanced 4DCBCT images.

rived with method B1. In Fig. 7 the resultant image at phase 1 is shown along with the image of the same phase before the enhancement. Because MGR technique was used for the 4D CBCT scan for the patient, the view-aliasing artifacts in the original 4DCBCT images are not prominent. The improvement by using the proposed approach is not dramatic as the previous simulation studies. The CNRs are 3.82 and 3.97 for the regular 4DCBCT and enhanced 4DCBCT, respectively. It is found that the proposed technique results in a smoother image in the uniform region leading to a higher CNR. However, it is also noticed that the process may reduce the spatial resolution. The trade-off between the CNR and the spatial resolution using the proposed model-based reconstruction technique requires further systematic study, which is beyond the scope of this work.

IV. DISCUSSION AND CONCLUSION

One goal of 4DCBCT is to remove the respiratory motion induced artifacts in the reconstructed images to increase the accuracy of target localization and dose calculation. Different from conventional 4DCT,[29–31] 4DCBCT acquisition with an onboard imager usually has a much slower speed of about 1 min per rotation, and due to the limited total scan time in practice, undersampling is often an issue resulting in severely degraded 4D images, which sometimes are even worse than the motion contaminated 3D images. The approach proposed in this article reconstructs the image of any particular phase by introducing additional information from other phases, effectively increasing the sampling rate and improving the image quality. In general, the approach relies on the accuracy of the motion model that relates different projections. We have demonstrated with 2D simulations that the best way to derive the motion model is to register the artifact-free CT images with the CBCT projections, if a planning CT scan has been performed prior to the CBCT scan. Though the registration accuracy in 3D geometry may be different from 2D geometry, these basic principles and relative performances observed in this article are expected true. As an example, the real patient case shown in this article demonstrated the feasibility of the proposed method under the worst condition (low view-aliasing artifacts in the 4D images leave little space for further improvement, and low accuracy in motion derivation by using method B1 limits the performance of the proposed approach).

As it is known, the radiation dose has been one of the major concerns in CBCT imaging because of the repeated use for a given patient. With the proposed approach, it is possible to lower the x-ray tube current, hence the radiation exposure for the 4DCBCT scan while maintaining a meaningful 4D image, because introducing additional information of other phases during reconstruction effectively increases the photon statistics. This is similar to the case of 4D fan-beam CT studied earlier by our group.[32] The efficacy of the approach in improving the trade-off between the controlled radiation exposure and the resultant CBCT image quality is being investigated.

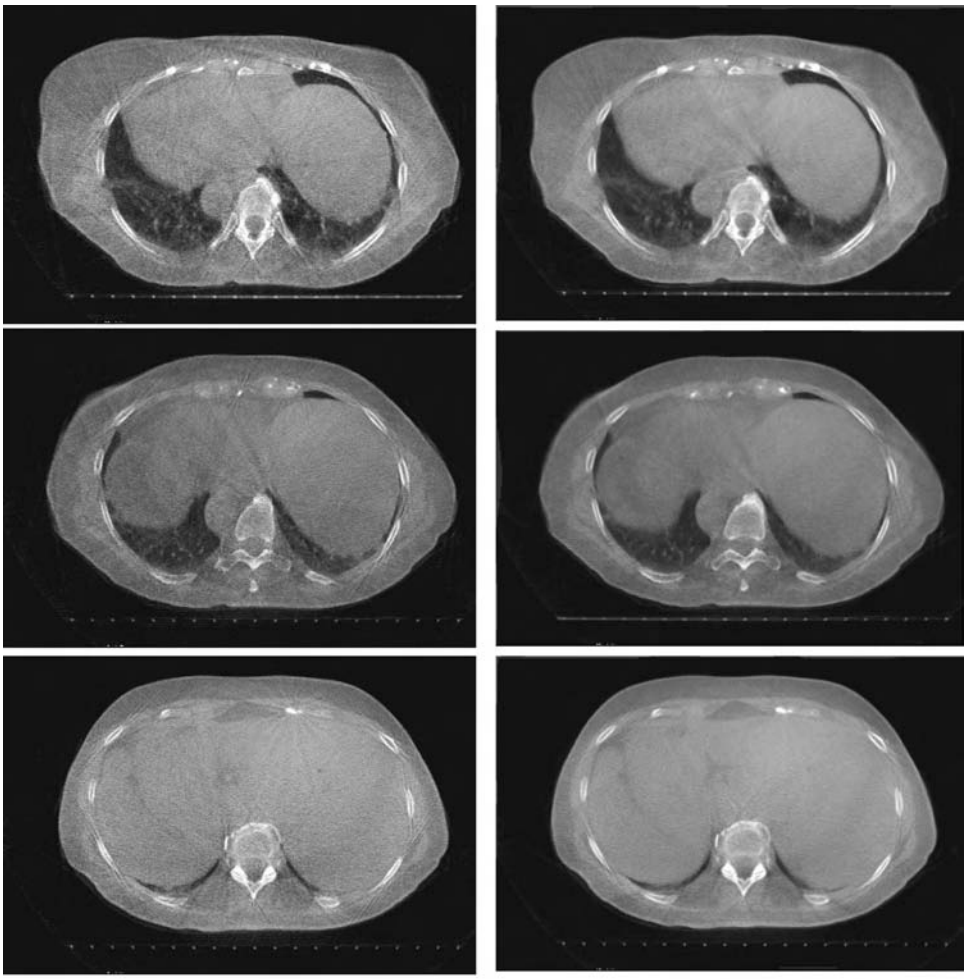

FIG. 7. 4DCBCT images of a patient. The left column shows three arbitrary slices of the peak inspiration phase, and the right column is the corresponding images after the proposed enhancement with motion model derived by using method B1.

It should be noted that the proposed 4DCBCT enhancing technique needs a computation of the deformation field before the image reconstruction, which takes extra time compared with regular CBCT imaging. Currently, a 3D image-to-image registration with an image size of $512 \times 512 \times 64$ will take approximately 30 min. The image-to-projection registration method generally takes longer because of the calculation of the forward projections. The computational time makes it difficult for online applications in the treatment room. However, the development of techniques in speeding up the algorithms as well as the computer hardware is highly promising, which we believe will make the 4DCBCT imaging fast and reliable in the near future. In addition, the 4DCBCT image quality may be further improved by the advanced reconstruction algorithm and helical scan mode.[33–35]

In conclusion, we have developed a novel approach to enhance the 4DCBCT image quality. The enhancement is achieved by increasing the angular sampling rate of each phase of the 4DCBCT data using information from other phases, thus the view-aliasing artifacts commonly seen in the limited-time scan 4DCBCT images are eliminated or significantly reduced. The approach opens new opportunities for 4DCBCT to be a more useful tool that may substantially improve the current cancer management in radiation oncology.

ACKNOWLEDGMENT

This work was supported in part by grants from the Department of Defense (DAMD-170310657) and the Susan Komen Breast Cancer Foundation (BCTR0504071).

[a]Author to whom correspondence should be addressed. Electronic mail: lei@reyes.stanford.edu

[1]L. Xing, B. Thorndyke, E. Schreibmann, Y. Yang, T. F. Li, G. Y. Kim, G. Luxton, and A. Koong, "Overview of image-guided radiation therapy," Med. Dosim. **31**, 91–112 (2006).

[2]R. I. Berbeco, S. B. Jiang, G. C. Sharp, G. T. Chen, H. Mostafavi, and H. Shirato, "Integrated radiotherapy imaging system (IRIS): Design considerations of tumour tracking with linac gantry-mounted diagnostic x-ray systems with flat-panel detectors," Phys. Med. Biol. **49**, 243–255 (2004).

[3]M. J. Ghilezan, D. A. Jaffray, J. H. Siewerdsen, M. Van Herk, A. Shetty, M. B. Sharpe, S. Zafar Jafri, F. A. Vicini, R. C. Matter, D. S. Brabbins, and A. A. Martinez, "Prostate gland motion assessed with cine-magnetic resonance imaging (cine-MRI)," Int. J. Radiat. Oncol., Biol., Phys. **62**, 406–417 (2005).

[4]D. Letourneau, A. A. Martinez, D. Lockman, D. Yan, C. Vargas, G.

Ivaldi, and J. Wong, "Assessment of residual error for online cone-beam CT-guided treatment of prostate cancer patients," Int. J. Radiat. Oncol., Biol., Phys. **62**, 1239–1246 (2005).
[5]T. R. Mackie, J. Kapatoes, K. Ruchala, W. Lu, C. Wu, G. Olivera, L. Forrest, W. Tome, J. Welsh, R. Jeraj, P. Harari, P. Reckwerdt, B. Paliwal, M. Ritter, H. Keller, J. Fowler, and M. Mehta, "Image guidance for precise conformal radiotherapy," Int. J. Radiat. Oncol., Biol., Phys. **56**, 89–105 (2003).
[6]R. Mohan, X. Zhang, H. Wang, Y. Kang, X. Wang, H. Liu, K. K. Ang, D. Kuban, and L. Dong, "Use of deformed intensity distributions for on-line modification of image-guided IMRT to account for interfractional anatomic changes," Int. J. Radiat. Oncol., Biol., Phys. **61**, 1258–1266 (2005).
[7]H. Shirato, S. Shimizu, T. Kunieda, K. Kitamura, M. van Herk, K. Kagei, T. Nishioka, S. Hashimoto, K. Fujita, H. Aoyama, K. Tsuchiya, K. Kudo, and K. Miyasaka, "Physical aspects of a real-time tumor-tracking system for gated radiotherapy," Int. J. Radiat. Oncol., Biol., Phys. **48**, 1187–1195 (2000).
[8]S. L. Meeks, J. F. Harmon, Jr., K. M. Langen, T. R. Willoughby, T. H. Wagner, and P. A. Kupelian, "Performance characterization of megavoltage computed tomography imaging on a helical tomotherapy unit," Med. Phys. **32**, 2673–2681 (2005).
[9]J. Pouliot, A. Bani-Hashemi, J. Chen, M. Svatos, F. Ghelmansarai, M. Mitschke, M. Aubin, P. Xia, O. Morin, K. Bucci, M. Roach III, P. Hernandez, Z. Zheng, D. Hristov, and L. Verhey, "Low-dose megavoltage cone-beam CT for radiation therapy," Int. J. Radiat. Oncol., Biol., Phys. **61**, 552–560 (2005).
[10]K. M. Langen, S. L. Meeks, D. O. Poole, T. H. Wagner, T. R. Willoughby, P. A. Kupelian, K. J. Ruchala, J. Haimerl, and G. H. Olivera, "The use of megavoltage CT (MVCT) images for dose recomputations," Phys. Med. Biol. **50**, 4259–4276 (2005).
[11]C. F. Elder, W. K. Rebecca, D. Letourneau, D. A. Jaffray, J. Bissonnette, A. Bezjak, P. Greg, W. Elizabeth, M. Carol, M. Michael, S. Michael, and G. Mary, "Towards a one-step scan and treat process for palliative radiotherapy-a potential application for cone beam computerized tomography (CBCT)," Int. J. Radiat. Oncol., Biol., Phys., Suppl. **63**, S440 (2005).
[12]M. Oldham, D. Letourneau, L. Watt, G. Hugo, D. Yan, D. Lockman, L. H. Kim, P. Y. Chen, A. Martinez, and J. W. Wong, "Cone-beam-CT guided radiation therapy: A model for on-line application," Radiother. Oncol. **75**, 271–278 (2005).
[13]Y. Yang, E. Schreibmann, T. Li, C. King, and L. Xing, "Dosimetric evaluation of kV cone-beam CT (CBCT) based dose calculation," Phys. Med. Biol. (to be published) (2006).
[14]T. Lo, Y. Yang, E. Schreibmann, T. Li, and L. Xing, "Mapping electron density distribution from planning CT to cone-beam CT (CBCT): A novel strategy for accurate dose calculation based on CBCT," Int. J. Radiat. Oncol., Biol., Phys., Suppl. **63**, S507 (2005).
[15]J. J. Sonke, L. Zijp, P. Remeijer, and M. van Herk, "Respiratory correlated cone-beam CT," Med. Phys. **32**, 1176–1186 (2005).
[16]T. Li, L. Xing, P. Munro, C. McGuinness, M. Chao, Y. Yang, B. Loo, and A. Koong, "Four-dimensional cone-beam computed tomography using a non-board imager," Med. Phys. **33**, 3825–3833 (2006).
[17]T. Li and L. Xing, "Optimize 4D cone-beam CT acquisition protocol for external beam radiotherapy," Int. J. Radiat. Oncol., Biol., Phys. (to be published) (2006).
[18]L. Dietrich, S. Jetter, T. Tucking, S. Nill, and U. Oelfke, "Linac-integrated 4D cone-beam CT: First experimental results," Phys. Med. Biol. **51**, 2939–2952 (2006).
[19]T. Li, E. Schreibmann, Y. Yang, and L. Xing, "Motion correction for improved target localization with on-board cone-beam computed tomography," Phys. Med. Biol. **51**, 253–267 (2006).
[20]D. Mattes, D. R. Haynor, H. Vesselle, T. K. Lewellen, and W. Eubank, "PET-CT image registration in the chest using free-form deformations," IEEE Trans. Med. Imaging **22**, 120–128 (2003).
[21]T. Rohlfing, C. R. Maurer, Jr., D. A. Bluemke, and M. A. Jacobs, "Volume-preserving nonrigid registration of MR breast images using free-form deformation with an incompressibility constraint," IEEE Trans. Med. Imaging **22**, 730–741 (2003).
[22]D. Rueckert, L. I. Sonoda, C. Hayes, D. L. Hill, M. O. Leach, and D. J. Hawkes, "Nonrigid registration using free-form deformations: Application to breast MR images," IEEE Trans. Med. Imaging **18**, 712–721 (1999).
[23]E. Schreibmann, G. T. Chen, and L. Xing, "Image interpolation in 4D CT using a BSpline deformable registration model," Int. J. Radiat. Oncol., Biol., Phys. **64**, 1537–1550 (2006).
[24]J. W. Wolthaus, M. van Herk, S. H. Muller, J. S. Belderbos, J. V. Lebesque, J. A. de Bois, M. M. Rossi, and E. M. Damen, "Fusion of respiration-correlated PET and CT scans: Correlated lung tumour motion in anatomical and functional scans," Phys. Med. Biol. **50**, 1569–1583 (2005).
[25]J. R. McClelland, J. M. Blackall, S. Tarte, A. C. Chandler, S. Hughes, S. Ahmad, D. B. Landau, and D. J. Hawkes, "A continuous 4D motion model from multiple respiratory cycles for use in lung radiotherapy," Med. Phys. **33**, 3348–3358 (2006).
[26]D. C. Liu and J. Nocedal, "On the limited memory BFGS method for large scale optimization," Math. Program. **45**, 503–528 (1989).
[27]R. Zeng, J. A. Fessler, and J. M. Balter, "Respiratory motion estimation from slowly rotating x-ray projections: Theory and simulation," Med. Phys. **32**, 984–991 (2005).
[28]R. Zeng, J. A. Fessler, and J. M. Balter, "Estimating 3-D respiratory motion from orbiting views by tomographic image registration," IEEE Trans. Med. Imaging **26**, 153–163 (2007).
[29]T. Pan, "Comparison of helical and cine acquisitions for 4D-CT imaging with multislice CT," Med. Phys. **32**, 627–634 (2005).
[30]T. Pan, T. Y. Lee, E. Rietzel, and G. T. Chen, "4D-CT imaging of a volume influenced by respiratory motion on multislice CT," Med. Phys. **31**, 333–340 (2004).
[31]S. S. Vedam, P. J. Keall, V. R. Kini, H. Mostafavi, H. P. Shukla, and R. Mohan, "Acquiring a four-dimensional computed tomography dataset using an external respiratory signal," Phys. Med. Biol. **48**, 45–62 (2003).
[32]T. Li, E. Schreibmann, B. Thorndyke, G. Tillman, A. Boyer, A. Koong, K. Goodman, and L. Xing, "Radiation dose reduction in four-dimensional computed tomography," Med. Phys. **32**, 3650–3660 (2005).
[33]X. Pan, Y. Zou, and D. Xia, "Image reconstruction in peripheral and central regions-of-interest and data redundancy," Med. Phys. **32**, 673–684 (2005).
[34]X. Pan, Y. Zou, D. Xia, and E. Y. Sidky, "Reconstruction of 3D regions-of-interest from data in reduced helical cone-beam scans," Technol. Cancer Res. Treat. **4**, 143–150 (2005).
[35]Y. Zou, E. Y. Sidky, and X. Pan, "Partial volume and aliasing artefacts in helical cone-beam CT," Phys. Med. Biol. **49**, 2365–2375 (2004).

Int. J. Radiation Oncology Biol. Phys., Vol. 67, No. 4, pp. 1211–1219, 2007

0360-3016/07/$–see front matter

ELSEVIER

doi:10.1016/j.ijrobp.2006.10.024

PHYSICS CONTRIBUTION

OPTIMIZING 4D CONE-BEAM CT ACQUISITION PROTOCOL FOR EXTERNAL BEAM RADIOTHERAPY

TIANFANG LI, PH.D., AND LEI XING, PH.D.

Department of Radiation Oncology, Stanford University School of Medicine, Stanford, CA

Purpose: **Four-dimensional cone-beam computed tomography (4D-CBCT) imaging is sensitive to parameters such as gantry rotation speed, number of gantry rotations, X-ray pulse rate, and tube current, as well as a patient's breathing pattern. The aim of this study is to optimize the image acquisition on a *patient-specific* basis while minimizing the scan time and the radiation dose.**

Methods and Materials: **More than 60 sets of 4D-CBCT images, each with a temporal resolution of 10 phases, were acquired using multiple-gantry rotation and slow-gantry rotation techniques. The image quality was quantified with a relative root mean-square error (RE) and correlated with various acquisition settings; specifically, varying gantry rotation speed, varying both the rotation speed and the number of rotations, and varying both the rotation speed and tube current to keep the radiation exposure constant. These experiments were repeated for three different respiratory periods.**

Results: **With similar radiation dose, 4D-CBCT images acquired with low current and low rotation speed have better quality over images obtained with high current and high rotation speed. In general, a one-rotation low-speed scan is superior to a two-rotation double-speed scan, even though they provide the same number of projections. Furthermore, it is found that the image quality behaves monotonically with the relative speed as defined by the gantry rotation speed and the patient respiratory period.**

Conclusions: **The RE curves established in this work can be used to predict the 4D-CBCT image quality before a scan. This allows the acquisition protocol to be optimized individually to balance the desired quality with the associated scanning time and patient radiation dose.** **© 2007 Elsevier Inc.**

Image-guided radiotherapy, Four-dimensional cone-beam CT, Optimization.

INTRODUCTION

Onboard cone-beam computed tomography (CBCT) imaging provides a convenient means for accurate patient setup and dose verification (1–8). However, when used for thorax or upper abdomen imaging, motion artifacts appear in the reconstructed images because of intrascanning organ motion within the field of view (FOV). According to the International Electric Commission recommendation, onboard CBCT systems have a limited gantry rotation speed of 60 s per round. A complete scan therefore consists of projection data from 10 to 20 respiratory cycles of the patient, resulting in large amount of inconsistency in the CBCT projection data. Reconstruction algorithms based on theories of static object lead to images that are significantly deteriorated by motion artifacts. Because of the prolonged scanning time, these motion-induced adverse effects in CBCT are much more severe than those seen in conventional CT scans (9). The artifacts not only blur the image, but also inhibit direct use of CBCT for dose calculation (10–12).

Four-dimensional (4D) CBCT, or respiration-correlated CBCT, groups the acquired projection data into several bins as according to their respiratory phases. Each phase bin is then reconstructed independently to obtain a volumetric image corresponding to that specific phase (13–15). 4D-CBCT not only greatly reduces the motion artifacts presented in each of these phase-resolved images, but also provides the dynamic information of the patient anatomy, which is absent in the three-dimensional (3D) case, and could be very useful in future 4D radiotherapy (1).

Because the total amount of projections acquired during a 4D-CBCT scan is divided into several phase groups, the number of projections available for each image reconstruc-

Reprint requests to: Lei Xing, Ph.D., Stanford University School of Medicine, Department of Radiation Oncology, 875 Blake Wilbur Drive, Stanford, CA 94305-5847. Tel: (650) 498-7896; Fax: (650) 498-4015; E-mail: lei@reyes.stanford.edu

This work was supported in part by grants from the Department of Defense (W81XWH-06-1-0235), the American Cancer Society (RSG-01-022-01-CCE) and Komen Breast Cancer Foundation (BCTR0504071).

Acknowledgment—We wish to thank A. Koong, K. Goodman, B. Loo, G. Luxton, T. Pawlicki, P. Maxim, E. Schreibmann, R. Wu, and R. Wiersma from Stanford University, and P. Munro, M. Svatos, S. Johnson, C. Zankowski, and R. Wicha from Varian Medical Systems for useful discussions.

Conflict of interest: none.

Received June 10, 2006, and in revised form Oct 3, 2006. Accepted for publication Oct 9, 2006.

tion becomes much less than in the regular 3D-CBCT case. As known from theory, the number of projections needed to avoid undersampling artifacts is inversely proportional to the reconstructed voxel size (16). An insufficient number of projections will lead to severe view-aliasing artifacts. To increase the number of projections for each phase, two strategies that can be employed are: slowing down the gantry rotation speed (SGR) and multiple gantry rotations (MGR). In addition to the gantry rotation speed and the number of gantry rotations, the quality of 4D-CBCT images is also sensitive to parameters such as the X-ray pulse rate, the tube current, and the patient's breathing pattern. These parameters constitute a multidimensional space, making the optimal 4D-CBCT protocol intractable. To balance the tradeoff between image quality, scan time, and patient radiation dose, a patient-specific 4D-CBCT acquisition protocol is highly desirable. This issue is systematically studied in this work, with the goal of fully understanding the influences of these various scanning parameters to optimize 4D-CBCT data acquisition protocol.

METHODS AND MATERIALS

4D-CBCT data acquisition system

An Acuity simulator (Varian Medical Systems, Palo Alto, CA) was used in this work for all CBCT imaging. In the case of regular 3D-CBCT simulation, a gantry rotation speed of 8°/s is used. The X-ray tube operates at 125 kVp and 80 mA with a pulse width at each projection angle of 9 ms when no bow-tie filter is used. The pulse width is increased to 25 ms if a bow-tie filter is used to maintain similar photon statistics. The data are acquired at ~15 frames/s and a full rotation (slightly more than 360°) consists of about 685 projections corresponding to an angle interval of about 0.5°. The radiation dose of a one-rotation CBCT scan at isocenter is approximately 4.0 cGy. The dimension of each acquired projection image is 397.3 mm × 298.0 mm, containing 1,024 × 768 pixels. With a source-to-axis distance of 100 cm and source-to-detector distance of 150 cm, the field of view is around 25 cm in diameter in the transverse plane for a full-fan mode. This can be close to 50 cm if a half-fan mode is employed (by shifting the flat-panel detector laterally). Here it should be noted that the half-fan mode generally results in inferior image quality when compared with that obtained with full-fan mode if all other acquisition parameters are maintained the same, and is a consequence of the loss of the data redundancy as is in the full-fan mode. However, for regions such as the thorax, a full-fan mode may result in truncated images, which are not appropriate for dose calculation. Thus the half-fan mode is preferred when a large field of view is required, and this mode is therefore used in this work.

To generate the 4D image sets, the acquired CBCT projections must be sorted into a number of bins according to their specific respiratory phases. The phase information of each projection can be obtained with the aid of a motion tracking system, for example, the Real-time Position Management system (Varian Medical Systems) as done in 4D-CT acquisition with conventional diagnostic CT scanners (17–25), or alternatively, it can be achieved by analyzing the acquired raw data in the projection space (26). In the latter, one or more CT-opaque fiducials are placed on the patient skin and the locations of the fiducials in the projections are detected by a computer searching algorithm. The coordinate of the fiducial is recorded as a function of the gantry angle, revealing the motion status of the object for each projection. In this work, the projection-space approach is used. Figure 1 shows an example of such a plot for the periodically moving phantom. The projections are phase-tagged according to the resultant sinusoidal curve, and sorted into 10 phase groups. The data in each phase bin are then reconstructed independently using a Feldkamp algorithm with a pixel size of 0.5 mm × 0.5 mm in the cross-section plane and a slice thickness of 1.0 mm.

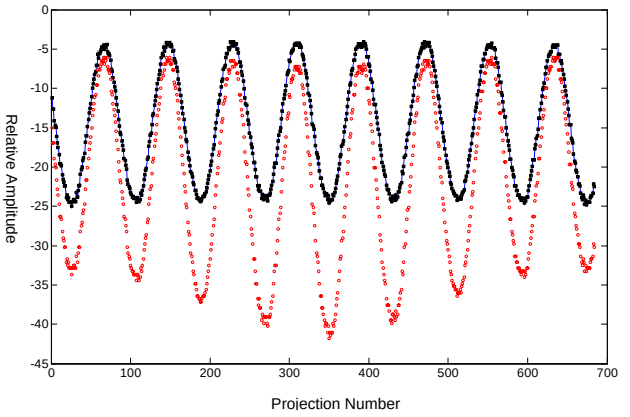

Fig. 1. An example of the projection-space phase tracking used in this work. The black solid squares and the red open circles represent the positions of the fiducial marker in the real world coordinate system and projection space, respectively. The sinusoidal curve obtained from cone-beam computed tomography projections can be used to determine the phase of each projection.

Motion phantom

To investigate the influence of various scanning parameters on the quality of 4D-CBCT, a motion phantom was constructed. The motion phantom consisted of a commercial CT calibration phantom CatPhan 600 (The Phantom Laboratory, Inc., Salem, NY) that is placed on top of a platform capable of sinusoidal motion along three directions: the phantom moved with the maximal displacements 5.5 cm in superoinferior direction, 1.5 cm in anteroposterior direction, and 0.2 cm in lateral direction. The period of the motion was continuously adjustable in the range of 0.5 s–1 min. In this work, three different periods were used to study the effects of breathing cycle on the image quality, which were 3.37 s, 4.59 s, and 6.53 s. 4D-CBCT images of the motion phantom were acquired using SGR or MGR methods as described in the following section. All 4D data acquisitions were using X-ray tube current of 10 mA unless otherwise stated. For comparison, three additional scans, with the phantom "frozen" at the "peak-inspiration," "mid-expiration" and "peak-expiration" phases, were obtained as well using the standard 3D-CBCT protocol (gantry rotation speed at 8°/s, X-ray tube current and voltage at 80 mA and 125 kVp, respectively). The three scans served as our "standards" for these phases.

4D-CBCT image analysis

Because the images in this work involve significant artifacts, a common metric such as contrast-to-noise ratio (CNR), defined as $CNR = | < \bar{S}_1 - \bar{S}_2 > |/\sigma$, may not be suitable, in the sense that a high CNR output may not represent a better image. For example, dark streak artifacts may accidentally decrease the mean value of

$\bar{S}_2$, leading to a high CNR value. Thus the CNR metric may highly depend on the selected regions of interest. To have a more robust and accurate assessment of the images obtained using different CBCT settings, a "relative root mean square error" (denoted by *RE*) is chosen as the figure of merit of the image quality, which is defined as

$$RE = \left(\sum_i (S_{4D}(i) - S_0(i))^2 \Big/ \sum_i S_0^2(i) \right)^{1/2}, \quad (1)$$

where S_{4D} denotes the 4D single-phase image, and S_0 is the standard 80-mA 3D-CBCT images of the phantom frozen at the same phase. The summation runs over all voxels of the images. In Eq. 1, S_0 image is used as the "gold standard," and the mean square error between the 4D images and the gold standard is normalized to the mean square of the true intensity.

Slow-gantry rotation strategy

A sufficient number of projections must be collected for each phase to remove the view-aliasing artifacts in 4D-CBCT. One way to achieve this is to slow down the gantry rotation. In this way, the number of breathing cycles covered by a full rotation is increased, leading to more projections in each phase group. Figure 2 is a sketch illustrating the relationship between the gantry rotation schemes and the breathing. The dark areas represent the available projections that belong to the same phase group.

To examine the influence of gantry rotation speed on the resultant image quality, scans were made of the motion phantom for eight gantry rotation speeds ranging from 8°/s to 1°/s. All other system variables were kept constant with the X-ray tube current and voltage in these eight scans being held at 10 mA and 125 kVp, respectively. This increased the total number of projections from about 680 for 8°/s speed to about 5,440 for 1°/s speed. Consequently, the number of projections in each phase bin increased by ~8 times. The resultant 4D-CBCT images were then analyzed using the RE metric as defined in Eq. 1.

Another important quantity for SGR 4D acquisition is the relation between image quality and the associated radiation exposure. For a constant X-ray pulse width, the radiation dose is directly proportional to the number of projections (beam-on time) and essentially linear to the X-ray tube current. Hence a scan with a rotational speed of 1°/s at 10 mA current will result in a similar amount of radiation as a scan with a 2°/s rotation speed at doubled the tube current. To investigate this image quality–tube current relationship, 4D-CBCT images of the motion phantom were acquired for 1°/s-10 mA, 2°/s-20 mA, 4°/s-40 mA, 5°/s-50 mA, and 8°/s-80 mA, for each of the three motion periods mentioned previously. These scanning schemes deliver a similar radiation dose to the phantom. A quantitative comparison of the 4D images was carried out.

Multiple-gantry rotation strategy

An alternative to SGR is MGR 4D acquisition, in which the gantry now rotates multiple times back and forth. As with SGR, the projections of the same phase are again collected and used for 4D-CBCT image reconstruction. The MGR acquisition scheme in relation to the breathing pattern is sketched in Fig. 2c. As shown, both SGR and MGR strategies lead to an increase in the number of projections over conventional CBCT (Figs. 2b, 2c); however, the angular distribution of the projections of a given phase group is very different. In SGR, the projections belonging to a particular breathing phase are regularly distributed in the angular space, whereas in MGR, two or more rotations lead to the projection becoming irregular. As a result, now there is a chance that, during the multiple gantry rotations, projections at the same phase and gantry angle may occur more than once, leading to redundancy of the data and resulting in less effective 4D-CBCT reconstruction. The angular overlap or partial overlap of the projection data can, in principle, be avoided/reduced by properly selecting the initial phase of the two (or multiple) scans. Generally, as illustrated in Fig. 2d, the chance for two successive scans to overlap is minimal when the gantry moves in opposite directions. One can imagine that if two scans are in the same direction, at every angle, the two projections from the two scans may be at same phase in the extreme case. This scenario will never happen if the two scans are in opposite directions. Two-rotation MGR scans with the gantry "back and forth" were performed for each of the previously mentioned three motion periods and the results were compared with that obtained using SGR. To maintain a constant radiation exposure, the gantry rotation speed in the MGR approach was increased by a factor of two as compared with that of a single rotation scan.

Relative gantry speed

Four-dimensional-CBCT image quality depends not only on the gantry rotation speed, but also on the patient respiratory pattern. This suggests that a *patient-specific* setting might be needed to achieve a similar quality of 4D-CBCT images. Here we propose a new measure of *relative speed* to combine the two variables of gantry rotation and patient respiration, which is defined as follows

$$\textit{Relative Speed} = \textit{Respiratory Period}(s) \times \textit{Gantry Rotation Speed}(\deg/s). \quad (2)$$

Relative speed has a unit of degree, which is the spanned angle of the CBCT scan during the time of one respiratory cycle.

The data acquired in these studies, for different motion periods and different scanning speed at constant X-ray tube current (10 mA) and voltage (125 kVp), were reanalyzed to illustrate the utility of the new concept in optimizing the 4D-CBCT image acquisition protocol on a patient-specific basis.

RESULTS

4D-CBCT image quality as a function of gantry rotation speed

Four-dimensional-CBCT images acquired with eight different gantry rotation speeds and constant X-ray tube current (10 mA) for the phantom moving at a period of 3.37 s are summarized in Fig. 3. From the top-left to the bottom-middle, the images correspond to gantry rotation speeds from 8°/s to 1°/s. Without loss of generality, only the phase 0% images of the 4D-CBCT acquisitions are compared here. Note that all other imaging parameters such as the tube current and voltage were the same for all the eight scans. The golden standard image (obtained with a standard 3D-CBCT protocol and without motion) is also shown at the bottom right in Fig. 3. As expected, it is found that the image quality improves with decreasing gantry rotation speeds. Similar trends were also observed for the phantom moving with the other two periods (4.93 s and 6.53 s).

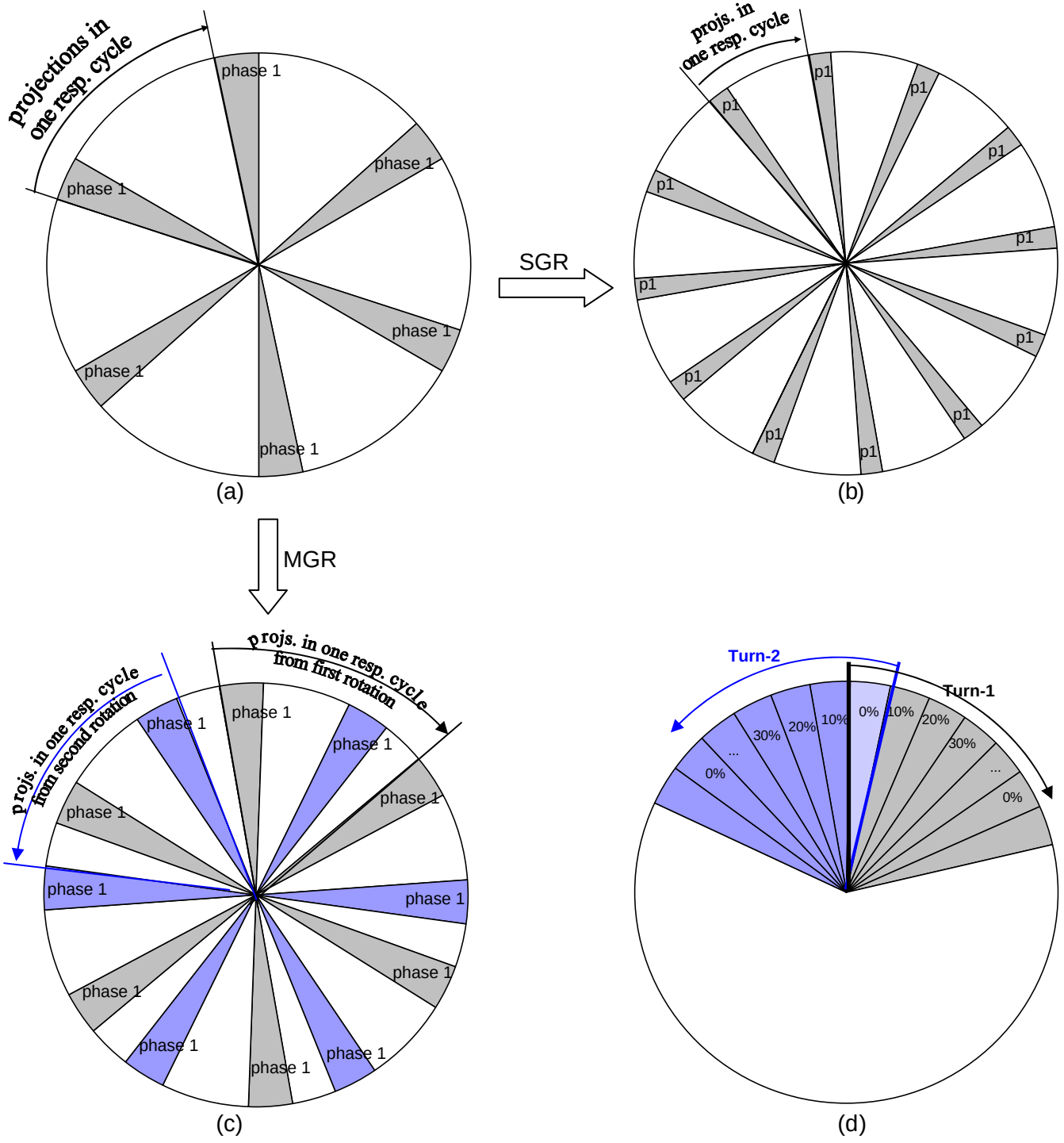

Fig. 2. Illustration of four-dimensional cone-beam computed tomography acquisitions with gantry rotation speed (SGR) and multiple gantry rotations (MGR) methods. The shadow in the diagrams represents the projections available for reconstruction of one particular phase. (a) Single rotation with rotation speed of a conventional three-dimensional scan, in which the number of projections in a phase bin is relatively small; (b) with SGR, a scan expands more respiratory cycles, hence more projections of the same phase can be collected; (c) with MGR, the number of projections in a phase group increases as shown by the gray and blue shadow; (d) the phase distribution in two successive rotations of the MGR method. Note that if two projections overlap at a particular angle, for example, for 0% phase, the projections at neighbor angles will be in different phases because the two rotations are in opposite directions.

The quantitative relation between image quality and gantry rotation speed was analyzed using the image metric of REs and the results were plotted in Fig. 4. For all three respiratory periods, the relative errors are found to increase with increasing gantry rotation speeds, indicating a drop in the image quality. Also from Fig. 4, it is seen that at a given

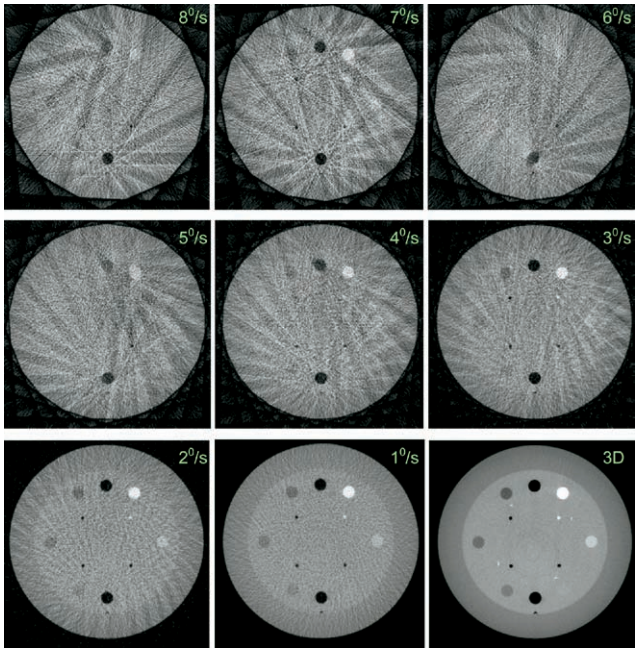

Fig. 3. From the top-left to the bottom-right are the four-dimensional cone-beam computed tomography (4D-CBCT) images of phase 0% obtained by varying the gantry rotation speed from 8°/s to 1°/s, and the three-dimensional CBCT images of the phantom "frozen" at the same phase. All 4D-CBCT were acquired with X-ray tube current of 10 mA.

gantry rotation speed, the image quality improves (smaller REs) with increasing phantom velocities. This is not surprising because a full scan at fast phantom speed will contain more respiratory cycles, leading to a reduction of the gap (Fig. 2) between the projections of same phase in two successive cycles, hence less view-aliasing artifacts. To help visualize this effect, Fig. 5 shows the 0% phase images obtained for the three different motion modes with the same gantry rotation speed of 2°/s.

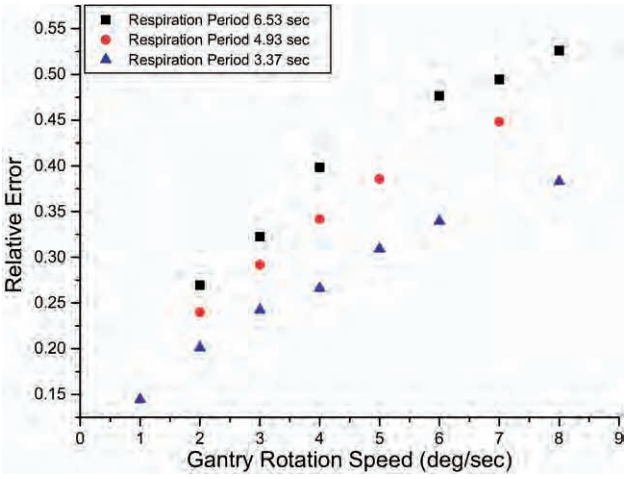

Fig. 4. Relation between relative root mean-square error and gantry rotation speed for three motion modes with periods of 3.37 s, 4.93 s, and 6.53 s, respectively.

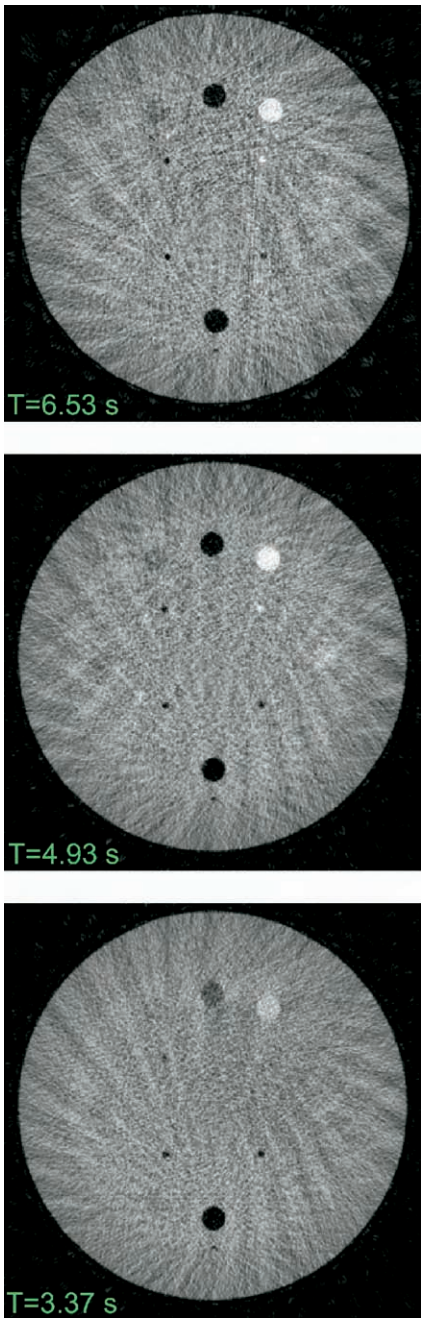

Fig. 5. Four-dimensional cone-beam computed tomography images of phase 0% obtained at the same gantry rotation speed of 2°/s, but different phantom motion periods.

SGR acquisition under the condition of a constant radiation exposure

As mentioned previously, the photon flux, noise level and patient radiation exposure are all related to the tube current. This is investigated by comparison of the 0% phase 4D images for scans of 8°/s at 80 mA, 5°/s at 50 mA, 4°/s at 40 mA, 2°/s at 20 mA, and 1°/s at 10 mA. Because the radiation exposure is approximately proportional to the tube current, scans with these eight settings deliver a similar level of radiation dose to the phantom. Again, the image metric of RE was employed to quantify the difference

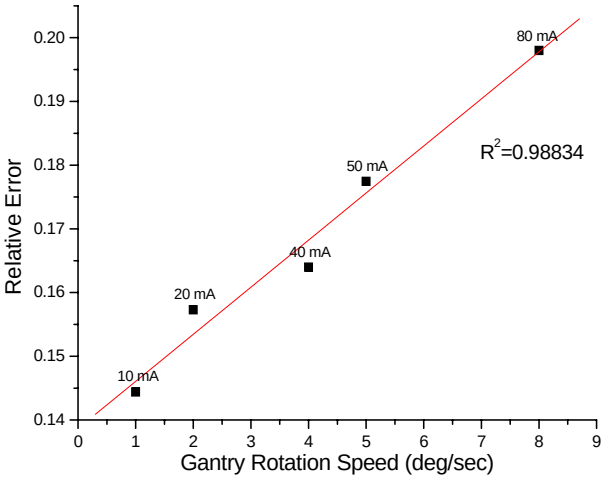

Fig. 6. The effects of increasing tube current and gantry rotation speed. With the same radiation dose, lower speed results in higher quality four-dimensional images as a result of increased number of projections per phase.

among the images. As shown in Fig. 6, the image acquired with the combination of 1°/s and 10 mA setting had the best quality (smallest RE). For visual comparison, the 1°/s—10 mA and 8°/s—80 mA images are shown in Fig. 7. Moving to slower gantry rotation speed will lead to each phase accumulating more projection data that can be used for reconstruction as compared with faster scans. As a consequence, the integral photon number (filtered back projection) at a spatial point is not reduced in the SGR low-current acquisition as compared with high-current, high-speed scans. Furthermore, at low scan speed, the data become more evenly spared along the 360° circle for each phase, leading to less view-aliasing artifact and consequently to higher image quality.

As shown in Fig. 6, it is found that RE increases almost linearly as a function of the scan speed. Because the total number of projections in a scan, and therefore the number of projections in each phase, varies linearly with the gantry rotation speed, it seems that the RE measure is an appropriate image metric, which has a linear relationship to the number of projections available for generating the phase image.

4D-CBCT imaging with single- and double-gantry rotations

Both SGR and MGR resulted in an increased number of projections. However, as illustrated in Figs. 2b and 2c, the angular distribution of the projections is different for the two acquisition schemes. In general, the efficiency of the MGR method depends on the level of projection redundancy or overlap of the data from the two or more gantry rotations. The 4D-CBCT images acquired with SGR and MGR were compared using the RE metric, and the results are summarized in Fig. 8. Here it is found that for all three motion modes (3.37 s, 4.93 s, and 6.53 s, respectively) and for different combinations of the gantry rotations speed and number of rotations, SGR almost always led to a lower RE or better image quality than the MGR method.

4D-CBCT image quality as a function of the relative speed

The relationship between the image quality and the relative speed is presented in Fig. 9. The data shown in Fig. 9 were fitted with a second order polynomial. The parameters of the model and the goodness of the fit are also shown in the figure. The monotonic dependence of the RE on the relative speed suggests that the relative speed is a meaningful concept in characterizing the 4D-CBCT data acquisition. The quantity "condenses" two important parameters (patient-specific respiration period and the gantry rotation speed) into one and is useful for us to optimize the 4D-CBCT acquisition protocol. In reality, because the respiratory period of a patient can be measured with the aid of a real-time position management signal or similar device (*e.g.*, strain gauge signal) before the 4D-CBCT scanning, a suitable gantry speed can be derived to achieve a prespecified image quality before 4D-CBCT scan. Alternatively, one can use the curve as shown in Fig. 9 to preestimate the 4D image quality for an acquisition setting and to estimate the corresponding patient radiation dose.

DISCUSSION

Cone-beam CT volumetric imaging integrated with a medical linear accelerator opens new avenues for improving current radiation oncology practice. In reality, CBCT has two important applications: patient setup and dose reconstruction/verification. By imaging the patient routinely during a course of radiation therapy, the accuracy of the patient setup can potentially be improved. Furthermore, the CBCT provides a pretreatment patient model on which the dose calculation can be performed using intended fluence maps from the planning system or other means. Both applications rely on the fidelity and quality of the volumetric images. When imaging in the region of thorax and upper abdomen, however, respiration-induced artifacts, such as blurring, doubling, streaking, and distortion are observed, which heavily degrade the image quality, and affect the target

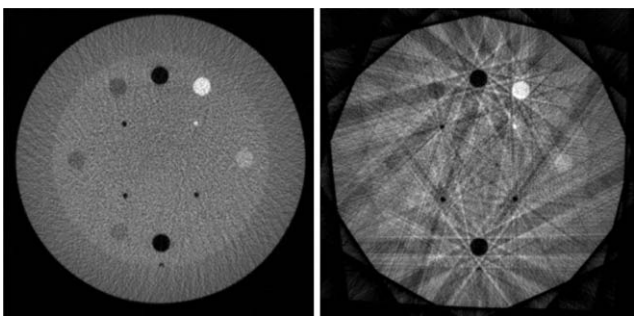

Fig. 7. Comparison of four-dimensional cone-beam computed tomography images acquired with speed 1°/s tube current 10 mA (left) and speed 8°/s tube current 80 mA (right).

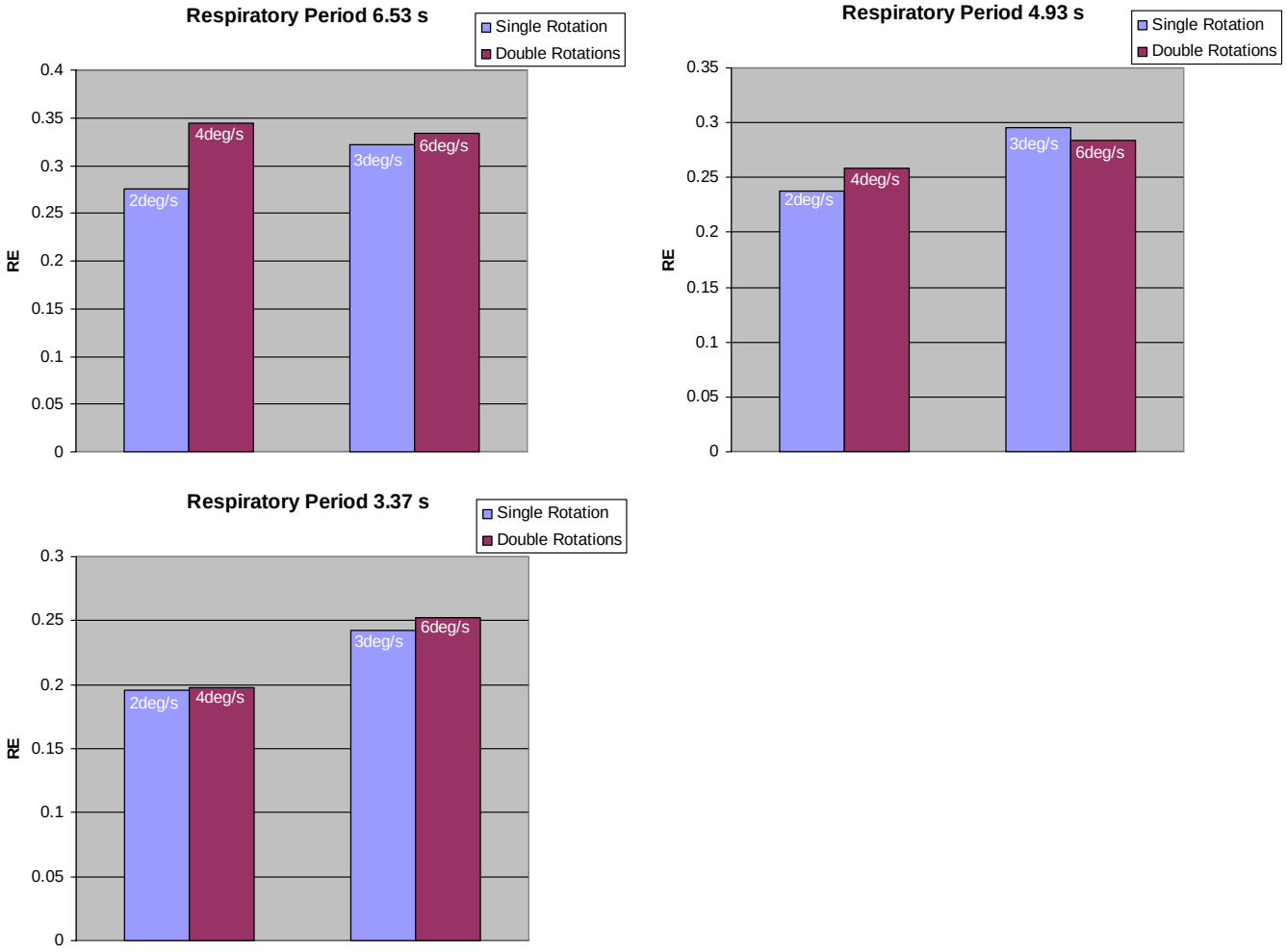

Fig. 8. The effects of increasing the number of rotations and gantry speed. With the same radiation dose, for most of the cases, low rotation speed results in a better image quality than multiple rotations.

localization ability and the accuracy of dose verification. These artifacts in CBCT are much more severe than those found in conventional CT exams because of the relatively slow gantry rotation. In conventional CT, each rotation of the scan can be completed within 0.5 s, during this period the organ/tumor motion is relatively small. Patient body restraints and breath-hold techniques can be used to minimize the motion if necessary. On the contrary, in CBCT scan, the gantry rotation speed is much slower, typically around 1 min for a full 360° scan in acquiring the projection data, which covers more than 10 breathing cycles for most patients. 4D-CBCT or phase-correlated CBCT is an effective way to reduce/eliminate the motion artifacts and makes it useful for guiding the patient setup and dose validation in the presence of organ motion.

Radiation dose is an important issue in CT imaging and, in particular the onboard CBCT imaging because of the repeated use of modality for a given patient. We found that, as we increase the number of projections per phase by slowing down the gantry rotation speed or multiple gantry rotations, the tube current can be lowered accordingly. In this way, the 4D image quality is generally not compromised and one can obtain decent 4D-CT images without increasing the radiation exposure. In a sense, this scheme is to "spread" the photons of a projection in 3D-CBCT to a range of angles in 4D-CBCT imaging, which represents a better tradeoff between the signal-to-noise ratio and the reduction in motion artifacts. In addition to the reduced patient dose, low current is essential to avoid overheating the X-ray tube, especially for an onboard imager without oil cooling system. Although the 4D image quality directly relates to the number of projections available for each phase, there is a limit for slowing down gantry speed. Beyond this limit, the time needed to complete the scan may be too long to cause patient discomfort and extra intrascan motion (other than the respiration-induced motion) may lead to undesirable artifacts. There is a practical need to keep the scanning time as short as possible while maintaining an acceptable image quality. The result shown in Fig. 9 provides guidance for the 4D-CBCT acquisition on a patient-specific basis, which predicts the quality of the 4D images for a certain gantry rotation speed and patient respiratory period. Though patient irregular breathing patterns may alter the number and angular distribution of the pro-

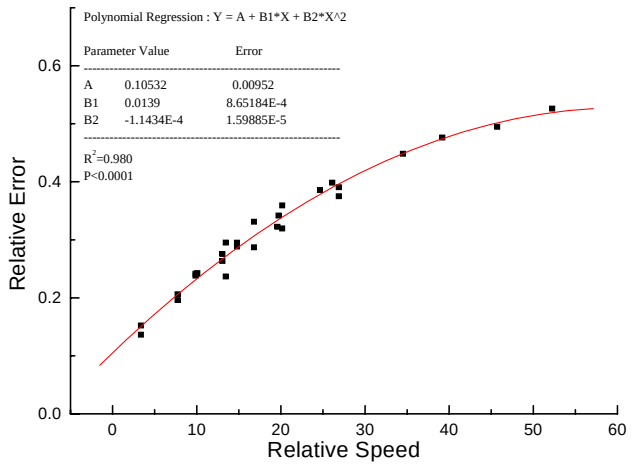

Fig. 9. Relationship between image quality and relative speed of the four-dimensional cone-beam computed tomography scan. The data were acquired for three motion modes with gantry rotation speed varying from 1°/s to 8°/s and constant X-ray tube current (10 mA) and voltage (125 kVp).

jections in each phase and thus change the image qualities, Fig. 9 will nonetheless represent an approximate relation between the image quality and the average patient respiratory period. Obviously, this approximation is valid only when the irregularity of the breathing pattern is not far from ideal periodic motion. It is also worth noting that the influence of breathing irregularity on the 4D images is different from that in conventional fan beam CT, in which the binning artifacts may arise due to mismatch of the slices corresponding to different couch positions.

Although 4D-CBCT technique (SGR or MGR) with phase binning before reconstruction reduces the motion artifacts and improves the image quality, it deals with each phase independently and ignores the correlation of the projections among different phase groups. It is of great interest to reconstruct a 4D object (with spatial and temporal parameters) rather than a series of independent 3D objects (with only spatial parameters), by using simultaneously all the projection data collected in different respiratory phase groups. With the aid of deformable registration and novel reconstruction techniques (9, 22, 27–33), it is possible to incorporate all projection data of different phases into one image reconstruction process. In this way, information from the measurement (CBCT scan) is fully used in the data processing, and more accurate imaging and better dose efficiency may be achieved.

CONCLUSIONS

We have demonstrated that 4D-CBCT images with significantly reduced artifacts can be obtained with a commercially available on-board imager system. A measure of relative error was used to quantify the image quality. At the same radiation dose, the low-current, low-speed acquisition is superior to acquisition with a high current and high speed (<8°/s), and, in most cases, for the same total scanning time, one-rotation low-speed scan is more preferable as compared with an acquisition based on multiple rotations and higher speed. Furthermore, we suggested that 4D-CBCT gantry rotation speed should be determined on a patient-specific basis and have established a quantitative relation between the 4D-CBCT image quality and the relative speed. The approach optimizes the 4D acquisition and makes an efficient use of the available 4D-CBCT technology. The study lays foundation for clinical application of 4D-CBCT and should have significant implication to image-guided radiation therapy.

REFERENCES

1. Xing L, Thorndyke B, Schreibmann E, *et al.* Overview of image-guided radiation therapy. *Med Dosim* 2006;31:91–112.
2. van Herk M, Jaffray D, Betgen A. First clinical experience with cone-beam CT guided radiation therapy: Evaluation of dose and geometric accuracy [Abstract]. *Int J Radiat Oncol Biol Phys* 2004;60(Suppl.):S196.
3. Sidhu K, Ford EC, Spirou S, *et al.* Optimization of conformal thoracic radiotherapy using cone-beam CT imaging for treatment verification. *Int J Radiat Oncol Biol Phys* 2003;55:757–767.
4. Oldham M, Letourneau D, Watt L, *et al.* Cone-beam-CT guided radiation therapy: A model for on-line application. *Radiother Oncol* 2005;75:271–278.
5. Langen KM, Meeks SL, Poole DO, *et al.* The use of megavoltage CT (MVCT) images for dose recomputations. *Phys Med Biol* 2005;50:4259–4276.
6. Mohan R, Zhang X, Wang H, *et al.* Use of deformed intensity distributions for on-line modification of image-guided IMRT to account for interfractional anatomic changes. *Int J Radiat Oncol Biol Phys* 2005;61:1258–1266.
7. Wu Q, Liang J, Yan D. Application of dose compensation in image-guided radiotherapy of prostate cancer. *Phys Med Biol* 2006;51:1405–1419.
8. Jaffray DA, Siewerdsen JH, Wong JW, *et al.* Flat-panel cone-beam computed tomography for image-guided radiation therapy. *Int J Radiat Oncol Biol Phys* 2002;53:1337–1349.
9. Yang Y, Schreibmann E, Li T, Xing L. Motion correction for improved target localization with on-board cone-beam computed tomography. *Phys Med Biol* 2006;51:253–267.
10. Li T, Schreibmann E, Yang Y, Xing L. Dosimetric evaluation of kV cone-beam CT (CBCT) based dose calculation. *Phys Med Biol.* In press.
11. Lo T, Yang Y, Schreibmann E, *et al.* Mapping electron density distribution from planning CT to cone-beam CT (CBCT): A novel strategy for accurate dose calculation based on CBCT. *Int J Radiat Oncol Biol Phys* 2005;63(Suppl. 2):S507.
12. Letourneau D, Martinez AA, Lockman D, *et al.* Assessment of residual error for online cone-beam CT-guided treatment of prostate cancer patients. *Int J Radiat Oncol Biol Phys* 2005;62:1239–1246.
13. Sonke JJ, Zijp L, Remeijer P, *et al.* Respiratory correlated cone beam CT. *Med Phys* 2005;32:1176–1186.
14. Moseley DJ, Hawkins M, Eccles C, *et al.* Respiratory gated cone-beam CT volumetric imaging for external beam radiotherapy. *Int J Radiat Oncol Biol Phys* 2005;63(Suppl. 1):s27–s28.
15. Sonke JJ, Van Herk M, Belderbos J, *et al.* An off-line 4D cone

beam CT based correction protocol for lung tumor motion. *Int J Radiat Oncol Biol Phys* 2005;63(Suppl. 1):s389–s390.
16. Crowther RA, DeRosier DJ, Kug A. The reconstruction of a three-dimensional structure from projections and its application to electron microscopy. *Proc R Soc London Ser A* 1970; 317:319–340.
17. Low DA, Nystrom M, Kalinin E, *et al.* A method for the reconstruction of four-dimensional synchronized CT scans acquired during free breathing. *Med Phys* 2003;30:1254–1263.
18. Rietzel E, Chen GTY. Improving retrospective sorting of 4D computed tomography data. *Med Phys* 2006;33:377–379.
19. Rietzel E, Pan T, Chen GTY. Four-dimensional computed tomography: Image formation and clinical protocol. *Med Phys* 2005;32:874–889.
20. Pan T, Lee TY, Rietzel E, *et al.* 4D-CT imaging of a volume influenced by respiratory motion on multi-slice CT. *Med Phys* 2004;31:333–340.
21. Vedam SS, Keall PJ, Kini VR, *et al.* Acquiring a four-dimensional computed tomography dataset using an external respiratory signal. *Phys Med Biol* 2003;48:45–62.
22. Li T, Schreibmann E, Thorndyke B, *et al.* Radiation dose reduction in four-dimensional computed tomography. *Med Phys* 2005;32:3650–3660.
23. Pan T. Comparison of helical and cine acquisitions for 4D-CT imaging with multislice CT. *Med Phys* 2005;32:627–634.
24. Wink N, Panknin C, Solberg TD. Phase versus amplitude sorting of 4D-CT data. *J Appl Clin Med Phys* 2006;7:77–85.
25. Wink NM, McNitt-Gray MF, Solberg TD. Optimization of multi-slice helical respiration-correlated CT: The effects of table speed and rotation time. *Phys Med Biol* 2005;50:5717–5729.
26. Li T, Xing L, Munro P, *et al.* 4D cone-beam CT (CBCT) using an on-board imager. *Med Phys* 2006;33:3825–3833.
27. Li T, Thorndyke B, Schreibmann E, Xing L. Model-based image reconstruction for four-dimensional PET. *Med Phys* 2006;33:1288–1298.
28. Schreibmann E, Chen GT, Xing L. Image interpolation in 4D CT using a BSpline deformable registration model. *Int J Radiat Oncol Biol Phys* 2006;64:1537–1550.
29. Zeng R, Fessler JA, Balter JM. Respiratory motion estimation from slowly rotating x-ray projections: Theory and simulation. *Med Phys* 2005;32:984–991.
30. Coselmon MM, Balter JM, McShan DL, *et al.* Mutual information based CT registration of the lung at exhale and inhale breathing states using thin-plate splines. *Med Phys* 2004;31: 2942–2948.
31. Brock KM, Balter JM, Dawson LA, *et al.* Automated generation of a four-dimensional model of the liver using warping and mutual information. *Med Phys* 2003;30:1128–1133.
32. Zou Y, Sidky EY, Pan X. Partial volume and aliasing artefacts in helical cone-beam CT. *Phys Med Biol* 2004;49:2365–2375.
33. Zou Y, Pan X. Exact image reconstruction on PI-lines from minimum data in helical cone-beam CT. *Phys Med Biol* 2004; 49:941–959.

Automated contour mapping using sparse volume sampling for 4D radiation therapy

Ming Chao, Eduard Schreibmann, Tianfang Li, Nicole Wink, and Lei Xing[a)]
Department of Radiation Oncology, Stanford University School of Medicine, Stanford, California 94305-5847

(Received 26 November 2006; revised 16 July 2007; accepted for publication 16 August 2007; published 26 September 2007)

The purpose of this work is to develop a novel strategy to automatically map organ contours from one phase of respiration to all other phases on a four-dimensional computed tomography (4D CT). A region of interest (ROI) was manually delineated by a physician on one phase specific image set of a 4D CT. A number of cubic control volumes of the size of ~1 cm were automatically placed along the contours. The control volumes were then collectively mapped to the next phase using a rigid transformation. To accommodate organ deformation, a model-based adaptation of the control volume positions was followed after the rigid mapping procedure. This further adjustment of control volume positions was performed by minimizing an energy function which balances the tendency for the control volumes to move to their correspondences with the desire to maintain similar image features and shape integrity of the contour. The mapped ROI surface was then constructed based on the central positions of the control volumes using a triangulated surface construction technique. The proposed technique was assessed using a digital phantom and 4D CT images of three lung patients. Our digital phantom study data indicated that a spatial accuracy better than 2.5 mm is achievable using the proposed technique. The patient study showed a similar level of accuracy. In addition, the computational speed of our algorithm was significantly improved as compared with a conventional deformable registration-based contour mapping technique. The robustness and accuracy of this approach make it a valuable tool for the efficient use of the available spatial-tempo information for 4D simulation and treatment. © *2007 American Association of Physicists in Medicine*. [DOI: 10.1118/1.2780105]

Key words: CT, image registration, contour mapping, IGRT

I. INTRODUCTION

A longstanding question in radiation therapy is how to accurately and efficiently segment a region of interest (ROI) such as a tumor target volume or a critical structure.[1–6] In spite of intense research efforts in the past few decades, ROI segmentation remains a time consuming task in treatment planning. In most cases, the segmentation is performed manually in a slice-by-slice fashion, creating a strong need for automated segmentation tools in the clinics. The introduction of four-dimensional computed tomography (4D CT) in radiation oncology practice further amplifies this need as the number of images to be segmented is increased dramatically.[7–15] Generally, a 4D CT scan consists of 5–10 sets of three-dimensional (3D) CT images, each representing the patient anatomy at a specific phase of respiration. For 4D radiation therapy applications, it is labor intensive to follow the 3D approach of manual segmentation due to the immense workload associated with this process.

A natural way to deal with the 4D segmentation problem is to start with a known set of contours for a selected phase and map these contours onto all other phases. ROIs for the selected phase are first manually contoured, similar to that done in treatment planning based on 3D CT image data sets. The mapping procedure can be accomplished with the aid of a computer algorithm that registers an arbitrary point on the selected phase to the corresponding points on all other phases. While conceptually simple, the implementation of this idea is not straightforward. An intelligent algorithm capable of providing accurate point-to-point correspondence between the phased images, or at least between points within the ROIs, is the key to the success of this approach. Various studies have investigated algorithms to automatically map contours using deformable image registration and surface mapping techniques. One method is based on a deformable registration model.[16–18] This method has limited accuracy, especially in the regions proximate to the interfaces of different organs, and is brute-force in nature, which entails a large amount of computations. In reality, contour mapping is a regional problem and a global association of the phase-based images is neither necessary nor efficient. Surface mapping achieves the stated goal of contour transformation by iteratively deforming the ROI contour-extended surface until the optimal match with the reference is reached.[2,19–22] Numerous surface mapping techniques, such as spatial partitioning, principal component analysis, conformal mapping, rigid affine transformation, deformable contours, and warping based on the thin-plate spline (TPS), have been developed over the years and the end point of all of these techniques is a mapping between topological components of the input surfaces that allow for transfer of annotations. This type of computation is inherently more efficient in comparison with the deformable model-based approaches, but it suf-

fers from the fact that the resultant mapping heavily depends on the model used and the fact that the model parameters in the calculations are not physically transparent.

In this work, we combine the useful features of the two different types of techniques for contour mapping. Our working hypothesis is that information contained in the boundary region is often sufficient to guide the contour mapping process without relying on the use of an *ad hoc* surface deforming model. In the proposed technique, the neighborhood information of the contour surface is captured by a series of small cubic (or other shaped) control volumes placed around the surface.[23] The collection of the centers of the control volumes is a representation of the contour surface. The ROI contour mapping proceeds iteratively under the guidance of the information contained in the control volumes. The proposed method is illustrated by a digital phantom experiment and three clinical lung case studies. The results suggest that the technique is capable of automatically mapping contours among the 4D CT phases with clinically acceptable accuracy.

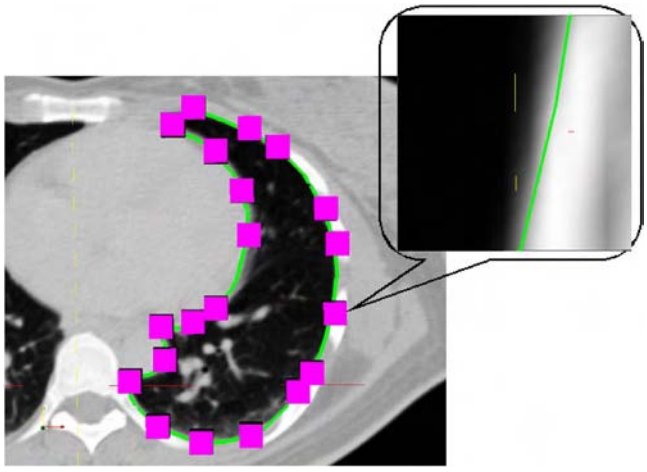

FIG. 1. A schematic drawing of the placement of control volumes (shown as squares) on the manually segmented contour (depicted curve). Each control volume is typically ~1 cm in cubic shape as shown in the zoomed image. No interpolated volumes are displayed.

II. MATERIALS AND METHOD

II.A. Software platform

The Insight Toolkit[24] (ITK) and the Visualization Toolkit[25] (VTK), which are open source cross-platform C++ software toolkits and are freely available for research purposes, were used in this study. A variety of methods have been programmed into the ITK platform for image registration and segmentation. ITK was used for automatic mapping while VTK was mainly used for 3D visualization and contour construction.

II.B. Image acquisition

The 4D CT image data sets for three lung cancer patients were acquired with a multislice helical CT scanner (Discovery ST, GE Medical System, Milwaukee, WI). The collected data were sorted into ten phase bins.[10] The 4D CT image sets for all patient studies were reconstructed with a 2.5 mm slice thickness. The size and pixel resolution of each CT slice was 512×512 and 0.98×0.98 mm^2, respectively. The 4D CT images were transferred through DICOM to a personal computer with a Pentium IV (2.66 GHz) processor for image processing. One of the phases, which is referred to as the template phase, was selected for manual segmentation of the ROIs. We refer to the other phases in the 4D CT image set as the target phases with corresponding target contours. The enrolled patients in this study were under an Institutional Review Board approved protocol.

II.C. Placement of control volumes along the ROI contour surface

The task of mapping a contour is to find its corresponding location on the target phase for an arbitrary point on the contour drawn on the template image. In general, the image feature surrounding a contour point can be used as a signature of the point to aid the search for its corresponding position on the target phase. In this study, the image feature at each point was captured by introducing a cubic control volume (~1 cm in size) centered at the point. The manual ROI delineation was first performed on the template phase using the Varian Eclipse TPS (Varian Medical Systems, Palo Alto, CA). Afterwards, the contours were exported from the TPS to a local computer for contour propagation. The exported contours are polygons on individual slices, and the vertices of the polygons were used as the locations of control volumes. This is depicted in Fig. 1, where the curve represents the contour and the squares represent the control volumes. The center of each control volume was set at a contour point, typically 0.5–1 cm from the next point. More control volumes are placed through interpolation if the spacing between two consecutive control volumes is greater than 1 cm. The collection of these points represents the ROI contour surface.

The contour mapping was carried out in three steps: (i) mapping the introduced control volumes collectively using a rigid image registration algorithm; (ii) iteratively fine-tuning the 3D positions of the control volumes to determine the deformed ROI contour surface; and (iii) reconstructing the new contours by cutting the deformed surface slice-by-slice along the transversal, sagittal, or coronal direction. This procedure is shown in Fig. 2 and described in detail below.

II.D. Collective mapping of control volumes

After a series of control volumes were placed along the segmented contours on the template phase, we mapped them onto the target phase collectively (i.e., all the control volumes were treated as an entity) using a rigid image registration algorithm.[24] A feature of the rigid collective mapping is that the relative distances and orientations of the control volumes remain the same during the course of mapping, resulting in an approximate ROI contour surface in the target phase and providing a good start for further adjustment of the contour shape to accommodate the organ deformations. We note that using a rigid mapping is not a necessary step

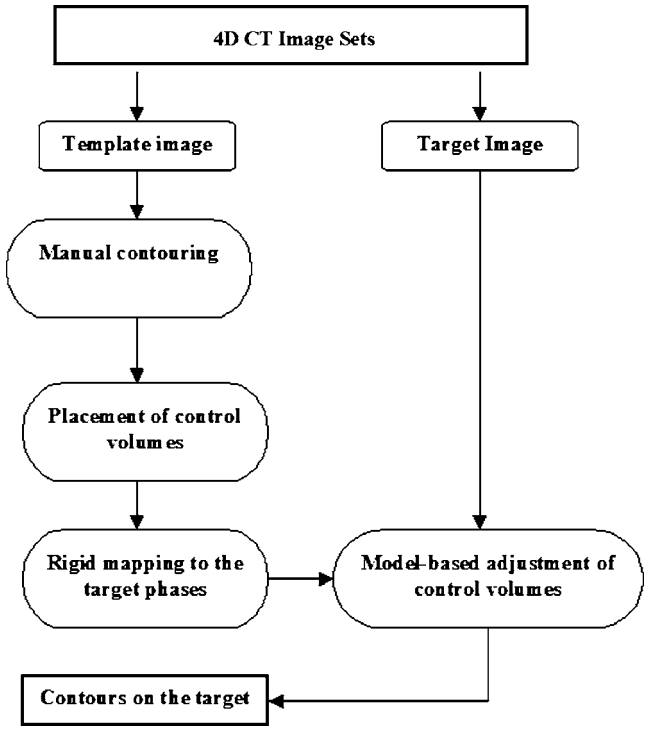

FIG. 2. Flow chart of the automatic contour mapping process for 4D CT images.

and other methods capable of providing a reasonable initial estimate of the ROI surface may also be used.

The collective mapping of the control volumes was performed under the guidance of a normal cross correlation (NCC) metric[24] defined by

$$f = -\frac{\sum_{\alpha}\sum_{\beta}\sum_{i=1} I_{\alpha}(\mathbf{x}_i) I_{\beta}(\mathbf{x}'_i)}{\sqrt{\sum_{\alpha}\sum_{i=1} I^2_{\alpha}(\mathbf{x}_i)\sum_{\beta}\sum_{j=1} I^2_{\beta}(\mathbf{x}'_j)}}, \quad (1)$$

where $I_{\alpha}(\mathbf{x}_i)$ is the intensity at a point $\mathbf{x}_i$ in a control volume indexed by α in the target phase and $I_{\beta}(\mathbf{x}'_j)$ represents the intensity at a point $\mathbf{x}'_j$ in a control volume indexed by β in the template phase. In Eq. (1), $\mathbf{x}$ and $\mathbf{x}'$ are related by a rigid transformation $\mathbf{T}$, where $\mathbf{T}\mathbf{x}' = \mathbf{x}$. We calculated the transformation matrix $\mathbf{T}$, which maps the ensemble of control volumes from the template phase to the target phase. The limited memory Broyden–Fletcher–Goldfarb–Shannon algorithm (L-BFGS) algorithm[26–30] was used to optimize the metric in Eq. (1) with respect to the transform parameters. The details of this algorithm have been described elsewhere[18,31] and will not be repeated here. During the course of the control volume mapping, an iterative calculation based on the L-BFGS algorithm was carried out until a preset maximum number of iterations were met or until the NCC function stopped improving.

II.E. Fine tuning of the mapped control volumes

In the absence of deformation, the ROI contour of the target phase is obtained by connecting the centers of the rigidly mapped control volumes. In a more general case where deformation does exist, the contour from the rigid mapping serves as an initial estimate of the ROI contour in the target phase. Further positional adjustment of the control volumes is needed to accommodate the deformation of the ROI. The final positions of the control volumes, which define the ROI surface, are determined by balancing the self-energy and the interaction energy, which drive the control volumes to their corresponding locations while maintaining similar shape integrity of the contour.

Mathematically, the above adaptation process is modeled by two "energy terms." The first term is referred to as "self-energy" and the second term describes the "interaction" among the control volumes. Self-energy tends to drive a control volume toward a position where the neighborhood environment resembles itself most. For each control volume in the template image, this process was driven by the NCC between the volume and its corresponding locations in the target image. The interaction term among the control volumes intends to maintain the integrity of the control volume cluster as a whole and prevents any unrealistic control volume configuration from happening. The interaction energy term is described by

$$E_{\text{interaction}} = M_{\text{template}} - M_{\text{target}}, \quad (2)$$

where M_{template} is defined as the correlation between a control volume in the template phase and the neighboring control volumes in the target phase, M_{target} represents the correlation between the control volume in the target phase and the neighboring volumes in the template phase. These two terms take into account the neighborhood environment of the control volume being adjusted and apply a constraint on the possible form of the control volume configuration. In a sense, the interaction energy in Eq. (2) exerts a restoring force when the position of a control volume is varied with respect to its neighbors. The interaction force is important in preventing the control volumes from moving to unrealistic positions simply driven by the self-energy and in retaining the shape integrity of the ROI surface. For simplicity, only the adjacent control volumes were considered when computing the interaction energies. The final position of each control volume was determined by minimizing the sum of the self-energy and interaction energy terms.

A simple searching algorithm was implemented to find the minimum of Eq. (2) and thus the final configuration of the control volumes. The algorithm was realized using an exhaustive search in the defined local region around the control volume and was based on three dimensional basis. For each rigidly mapped control volume on the target phase, we defined a small region of ~3 cm around the central point in the volume. The search region of 3 cm was chosen primarily to accommodate maximum deformation of tissue. 3 cm is a very conservative value because the tissue deformation in two adjacent phases barely exceeds this value (the maximum deformation occurring between the inhale and exhale phases may reach ~3 cm). Equation (2) was then minimized to determine the optimal control volume location within this region. This process was repeated for each separate control

volume. Due to the fact that the interaction energy term demands the information from the neighboring volumes, adjusting the location of each control volume changes the position of the previously fine-tuned volume. Therefore, several cycles of this process were needed to obtain the truly optimal positions of all the control volumes. We found (see digital phantom study in results section) that 2–3 complete adjustment cycles were adequate to find the optimal control volume configuration.

II.F. Reconstruction of target contours

Upon completion of the control volume mapping and adaptation, the centers of each control volume were identified. A ROI surface was constructed with these central points using a triangulated surface construction technique which uses marching cubes[32] method and triangular surface decimation of VTK.[25,33] The intersection of the surface with each CT slice was superimposed on top of the image in order to visualize the contour in a conventional fashion. These contours can be exported as ASCII or DICOM-RT format for treatment planning.

II.G. Evaluation of the algorithm and case study

Evaluation of a contour mapping algorithm is a difficult task because of the general lack of a gold standard for comparison. The proposed control volume based 4D contouring technique was first evaluated with a digital phantom experiment. In this study, a thoracic CT image was deformed intentionally using a known deformation matrix which was introduced by drifting the positions of each control volume along the contour with known sizes. Specifically, for a control volume i, we assign the following displacements:

$$D(x,y) = i * 0.01 \text{ and } D(z) = i * 0.001 \text{ if } i = 0, 1, \ldots, N/2 \quad (3)$$

or

$$D(x,y) = (N - i) * 0.01 \text{ and } D(z) = (N - i) * 0.001 \text{ if } i = N/2 + 1, N/2 + 2, \ldots N, \quad (4)$$

where N is the total number of control volumes on the ROI contour. The artificially deformed image serves as a "new breathing phase" relative to the original image. The "ground truth" lung surface in the target phase was attainable by transforming the original contours with the same deformation matrix. The manually delineated lung contours in the original image were also mapped using the proposed novel control volume based approach. A comparison of the mapped lung surface with the ground truth allowed us to quantitatively assess the success of the proposed approach.

The control volume based contour mapping technique was also applied to three 4D CT patient scans. A physician manually delineated the lungs and GTV for each scan on a selected phase (for example, the exhale phase). These contours were then mapped onto all other phases using the proposed technique. Visual inspection was used to evaluate the three patient studies. Although it is less quantitative, visual inspection is a cnvenient way for rapid assessment of a segmentation calculation, especially in a case where the ground truth contours do not exist.

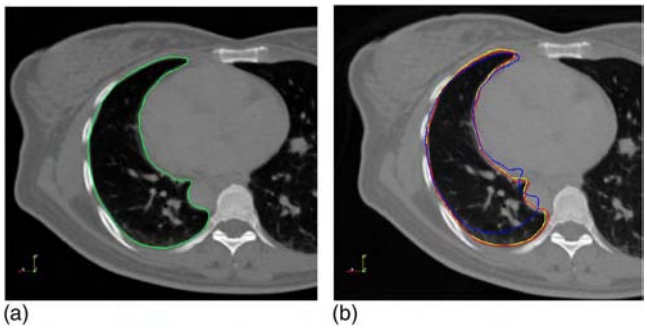

FIG. 3. Validation process of proposed algorithm using a digital phantom. (a) Original image and contour; (b) Artificially deformed image and contour (ground truth contour) together with contour after fine tuning. These two contours are almost indistinguishable. The contour after rigid mapping is also shown.

III. RESULTS

III.A. Digital phantom study

The thoracic CT images before and after the intentionally introduced deformation are shown in Fig. 3. The manually delineated lung contour is shown in Fig. 3(a), while the ground truth contour obtained by transforming the manual contour with the known transformation matrix is plotted in Fig. 3(b). The contour from the proposed approach is shown in the same figure. To be comprehensive, the rigidly mapped contour, which served as the start of the model-based refinement, is also plotted in Fig. 3(b). Clearly, it is significantly deviated from the lung boundary. Visual inspection of the ground truth contour and contour after refinement in Fig. 3(b) indicated that the gold standard and the mapped contours are similar, despite the fact that the intentionally introduced deformation field is quite large (the displacement of the some of the voxels is as large as 2.0 cm). The mean and maximum separations between the two sets of contours were found to be 1.5 and 2.5 mm, respectively.

To better understand the mapping process, we examined the behavior of each energy term (metrics) during the course of the contour mapping. In Fig. 4(a) we plotted the values of self-energy, interactive energy, and total energy of one of the control volumes in the process of positional adjustment in the surrounding area of the control volume in the deformed image. For this particular control volume, the minimum of Eq. (2) was reached after searching the first 30 points. For control volumes located in regions where the deformation is large, more searching points may be required to reach the minimum. It is also interesting to show how the average metric value of all the control volumes evolved. In Fig. 4(b) the metric value is depicted as a function of the calculation process. The first point, corresponding to step 0, is the metric before mapping. Step 1 refers to the system after rigid mapping. The metric at this point is decreased but does not reach the minimum. The third point shows the metric after each of

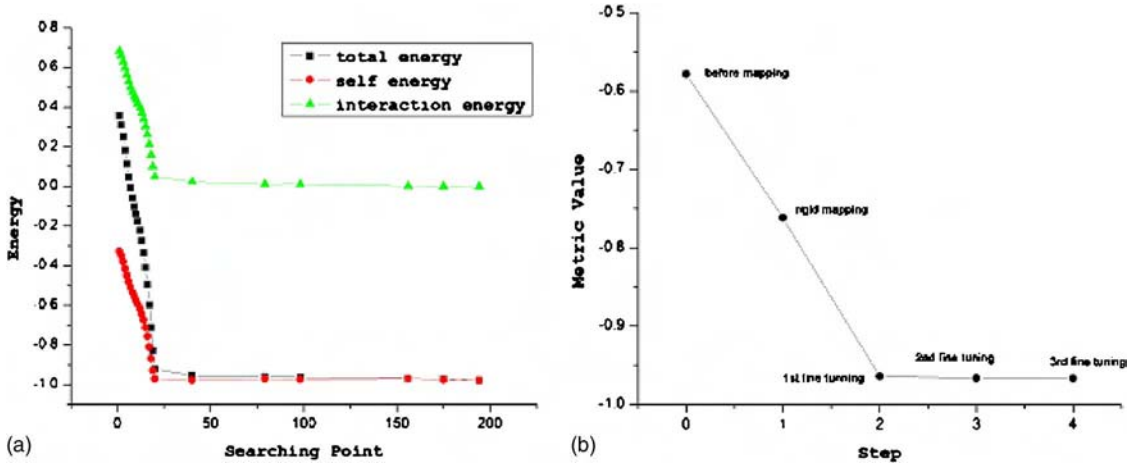

FIG. 4. (a) Energies (self, interaction, and total energy) as a function of the searching points in the surrounding area of a randomly selected control volume in the target image (see text for details). (b) The metric value versus step during the course of the contour mapping. The metric values are the average NCC of all the involved control volumes.

the control volumes is fine tuned sequentially. To obtain the optimal contours two more cycles of fine tuning were performed; however, the improvement with further iterations was not significant.

III.B. Patient studies

The proposed technique was assessed using 4D CT images of three lung cancer patients. Figure 5 shows the manually delineated contours on the 4D CT scans of two lung cancer patients for lung and GTV, respectively. The CT images and contours are displayed in axial, coronal, and sagittal views. Contours were drawn on the exhale phases (phase 1) for patient 1 (top row in Fig. 5). The GTV contour for patient 3 was delineated on the inhale phase (phase 5) as shown in Fig. 5 bottom row. For patients 1 and 2 the mapping of the lung contours was studied. For the third patient, GTV contour mapping was investigated.

The lung contours before and after the control volume-based mapping for the first patient are presented in Fig. 6. To better visually evaluate the results, the CT images and contours for this patient are displayed in axial, coronal, and sagittal views as in left, middle, and right columns, respectively. Target phases 4, 7, and 10 are selected to demonstrate the results as in the top, middle, and bottom rows in Fig. 6. The template contours and rigidly mapped contours were shown and significantly deviated from the ROI boundary. The final contours after the model-based adaption are presented as well.

When the lung deformation is small, for example, in phase 10 of patient 1 [see Figs. 6(g)–6(i)], the rigidly mapped contours closely resemble the target contours. Fine tuning merely provides limited adjustment of the contours. For phases with large deformations (e.g., phases of 4 and 7

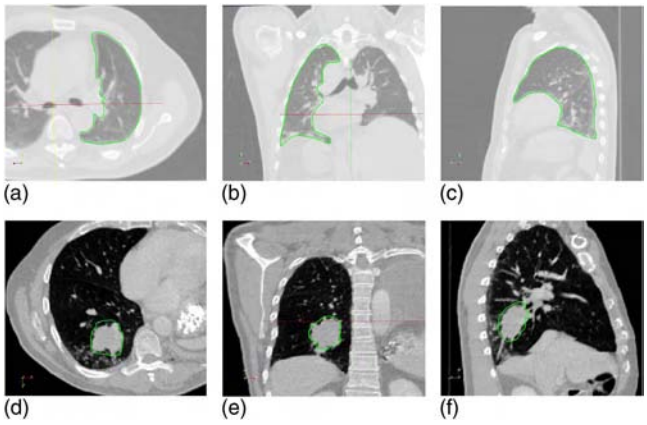

FIG. 5. The template CT images and manually segmented contours for two lung cancer patients (top row: patient 1; bottom row: patient 3) on axial, coronal, and sagittal views. Right lung of patient 1 and GTV of patient 3 were manually delineated, respectively.

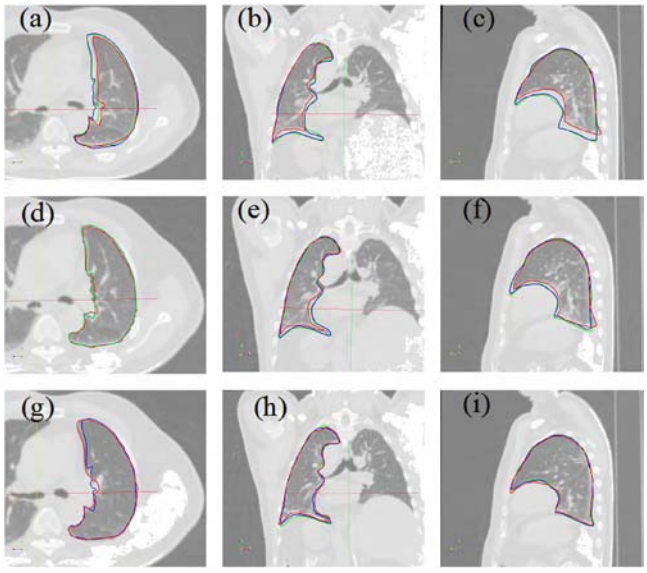

FIG. 6. Axial, coronal, and sagittal views of CT images along with lung contours for the first patient. Top row: phase 4; middle row: phase 7; bottom row: phase 10. Rigidly mapped and target contours are displayed. Template contour is also overlaid on displayed phases.

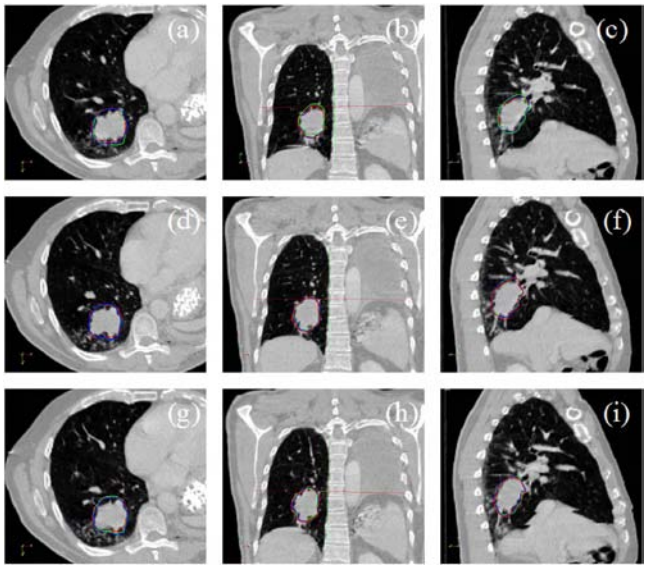

FIG. 7. Axial, coronal, and sagittal views of CT images along with GTV contours for the third patient. Top row: phase 2; middle row: phase 4; bottom row: phase 7. Rigidly mapped and target contours are displayed. Template contour is also overlaid on displayed phases.

of this patient), the model-based adjustment after the rigid contour mapping plays an important role in obtaining optimal contour arrangement. In case of the lung contours, our analyses of the patient data indicate that the accuracy of our contour mapping technique is within one pixel in the superior part of the lung, where respiration induced deformation is small. In other parts, the average error on the target contours is estimated to be less than 2.5 mm.

The mapped GTV contours for phases 2, 4, and 7 in the study of patient 3 are shown in Fig. 7. The representation of the contours is the same as in Fig. 6. For phases 4 and 7 the deformation was relatively small and our contour mapping algorithm performed reliably. For phase 2, which corresponded to the exhale phases, significant deformation in the ROIs was observed. Despite this less ideal case, our algorithm still worked well in these phases.

IV. DISCUSSION

As in 3D radiation therapy, delineation of ROIs in 4D CT images is a necessary step for treatment planning.[34] 4D segmentation is required for constructing a 4D patient model and for computing the accumulated dose of moving or deformed organs. One way to proceed is to draw all contours on one of the phases of respiration and map or propagate these contours onto the remaining phases. Various deformable models have been used for ROI contour mapping as discussed in the introduction. In this work, we take a regional approach based on the mapping and adaptation of the sparsely sampled control volumes. Our approach takes advantage of the imaging features surrounding the ROI and uses them as guidance in searching for the optimal mapped contours while considering the shape integrity of the ROI surface.

The mapping of a point in one image to another is easily achievable if a unique identifier or signature can be tagged to the point. Here the image feature contained in a control volume is employed as a signature of the point to facilitate the process of finding its corresponding location in the target phases. The concept of control volume was first introduced by Schreibmann and Xing[23] and its advantages for both intra- and intermodality image registration have been demonstrated. This study represents a novel application of the concept to 4D image segmentation. After a rigid mapping of the contours from the template phase to the target phase, a model-based adaptation is performed to establish a reliable association between the ROIs in two phase specific image sets. This adaptation takes into account the deformation of an object and ensures the overall integrity of the resultant ROI surface. The calculation is local in nature, which improves both computational efficiency and convergence behavior.

A quantitative comparison of different deformable registration algorithms is a difficult task because of the multifaceted and even subjective nature of the problem. A unbiased and meaningful comparison may entail the efforts from multiple institutions.[35] Thus we defer the detailed comparative study to the future. However, we wish to emphasize that the chief advantage of the proposed technique is its computational efficiency. Because of the regional nature of the calculation, our general finding is that the new algorithm is at least an order of magnitude faster than the whole image based approach.[17,18] Enormous saving in the memory usage in the proposed approach is also self-explanatory and highly desirable feature in practice.

A common problem in image segmentation and contour mapping studies is the lack of quantitative validation. In the study of Lu *et al.*,[36] for example, the accuracy of a deformable model-based contour mapping technique was evaluated purely based on visual inspection. The same approach was employed in many other previous investigations.[4,6,16,18] In our study, in addition to the visual evaluation, a set of digital phantom experiments was introduced to evaluate the success of the proposed technique. By applying a prespecified deformation matrix to the original image, the ground truth of the contour propagation is readily known. Therefore, the experiments provide a quantitative test of the proposed algorithm. In general, we found that a spatial accuracy better than 2.5 mm is achievable using our technique.

V. CONCLUSION

The development of 4D radiation therapy involves the use of a large number of images acquired at different times and/or with different modalities. Clinical implementation of the new IGRT paradigm is, to a large extent, bottlenecked by the inability to accurately and efficiently register images and segment the ROIs. In this work, a mathematical framework for control volume-based contour mapping has been proposed for 4D radiation therapy. We demonstrated that the information contained in the boundary region is sufficient to guide the contour mapping process without registering the whole image or relying on the use of an *ad hoc* surface

deforming model. The results showed that the control volume-based contour mapping algorithm is capable of robustly and accurately mapping contours from one phase of a 4D CT to the remaining phases. Our technique decreases the workload involved in 4D CT ROI segmentation and provides a valuable tool for the efficient use of available spatial-tempo information for 4D simulation and treatment.

ACKNOWLEDGMENTS

This work was supported in part by grants from the Department of Defense (W81XWH-06-1-0235 and W81XWH-05-1-0041), Komen Breast Cancer Foundation (BCTR0504071), and National Cancer Institute (5R01 CA98523 and 1R01 CA98523).

[a]Author to whom correspondence should be addressed. Present address: Stanford University School of Medicine, Department of Radiation Oncology, 875 Blake Wilbur Drive, Stanford, CA 94305-5847; Telephone: (650)498-7896; Fax: (650)498-4015; Electronic mail: lei@reyes.stanford.edu

[1]M. R. Kass, A. Witkin, and D. Terzopoulos, "Snakes: Active contour models," Int. J. Comput. Vis. **1**, 321–331 (1988).
[2]T. Cootes, A. Hill, C. Taylor, and J. Haslam, "The use of active shape models for locating structures in medical images," J. Image. Vis. Comput. **12**, 355–366 (1994).
[3]C. Xu and J. L. Prince, "Snakes, shapes, and gradient vector flow," IEEE Trans. Image Process. **7**, 359–369 (1998).
[4]F. Liu, B. Zhao, P. K. Kijewski, L. Wang, and L. H. Schwartz, "Liver segmentation for CT images using GVF snake," Med. Phys. **32**, 3699–3706 (2005).
[5]J. Weese *et al.*, "Shape constrained deformable models for 3D medical image segmentation," Information Processing in Medical Imaging: 17th International Conference, IPMI 2001, Davis, CA, June 18–22, 2001, Vol. 2082, pp. 380–387 (2001).
[6]V. Pekar, T. R. McNutt, and M. R. Kaus, "Automated model-based organ delineation for radiotherapy planning in prostatic region," Int. J. Radiat. Oncol. Biol. Phys. **60**, 973–980 (2004).
[7]C. J. Ritchie, J. Hsieh, M. F. Gard, J. D. Godwin, Y. Kim, and C. R. Crawford, "Predictive respiratory gating: A new method to reduce motion artifacts on CT scans," Radiology **190**, 847–852 (1994).
[8]S. S. Vedam, P. J. Keall, V. R. Kini, H. Mostafavi, H. P. Shukla, and R. Mohan, "Acquiring a four-dimensional computed tomography dataset using an external respiratory signal," Phys. Med. Biol. **48**, 45–62 (2003).
[9]L. Xing, B. Thorndyke, E. Schreibmann, Y. Yang, T. F. Li, G. Y. Kim, G. Luxton, and A. Koong, "Overview of image-guided radiation therapy," Med. Dosim. **31**, 91–112 (2006).
[10]T. Pan, T. Y. Lee, E. Rietzel, and G. T. Chen, "4D-CT imaging of a volume influenced by respiratory motion on multi-slice CT," Med. Phys. **31**, 333–340 (2004).
[11]L. Dietrich, S. Jetter, T. Tucking, S. Nill, and U. Oelfke, "Linac-integrated 4D cone beam CT: First experimental results," Phys. Med. Biol. **51**, 2939–2952 (2006).
[12]T. Li, E. Schreibmann, B. Thorndyke, G. Tillman, A. Boyer, A. Koong, K. Goodman, and L. Xing, "Radiation dose reduction in four-dimensional computed tomography," Med. Phys. **32**, 3650–3660 (2005).
[13]W. Lu and T. R. Mackie, "Tomographic motion detection and correction directly in sonogram space," Phys. Med. Biol. **47**, 1267–1284 (2002).
[14]T. Li, L. Xing, P. Munro, C. McGuinness, M. Chao, Y. Yang, B. Loo, and A. Koong, "Four-dimensional cone-beam computed tomography using an on-board imager," Med. Phys. **33**, 3825–3833 (2006).
[15]J. J. Sonke, L. Zijp, P. Remeijer, and M. van Herk, "Respiratory correlated cone beam CT," Med. Phys. **32**, 1176–1186 (2005).
[16]T. M. Guerrero, G. Zhang, T. C. Huang, K. P. Lin, P. Giraud, Y. De Rycke, B. Dubray, S. Helfre, D. Voican, L. Guo, J. C. Rosenwald, K. Keraudy, M. Housset, E. Touboul, and J. M. Cosset, "Intrathoracic tumour motion estimation from CT imaging using the 3D optical flow method," Phys. Med. Biol. **49**, 4147–4161 (2004).
[17]D. Ragan, G. Starkschall, T. McNutt, M. Kaus, T. Guerrero, and C. W. Stevens, "Semiautomated four-dimensional computed tomography segmentation using deformable models," Med. Phys. **32**, 2254–2261 (2005).
[18]E. Schreibmann, G. T. Chen, and L. Xing, "Image interpolation in 4D CT using a B Spline deformable registration model," Int. J. Radiat. Oncol. Biol. Phys. **64**, 1537–1550 (2006).
[19]T. McInerney and D. Terzopoulos, "Deformable models in medical image analysis," Med. Image Anal. **1**, 91–108 (1996).
[20]A. Chakraborty, L. H. Staib, and J. S. Duncan, "*An integrated approach for surface finding in medical images*" IEEE Workshop Mathematical Methods in Biomedical Image Analysis, 1996, pp. 253–262.
[21]J. Montagnat, H. Delingette, and N. Ayache, "A review of deformable surfaces: Topology, geometry and deformation," Image Vis. Comput. **19**, 1023–1040 (2001).
[22]J. Montagnat and H. Delingette, "4D deformable models with temporal constraints: Application to 4D cardiac image segmentation," Med. Image Anal. **9**, 87–100 (2005).
[23]E. Schreibmann and L. Xing, "Image registration with auto-mapped control volumes," Med. Phys. **33**, 1165–1179 (2006).
[24]L. Ibanez, W. Schroeder, L. Ng. ITK Software Guide, Kitware Inc., 2003, http://www.itk.org.
[25]W. Schroeder, K. Martin, B. Lorensen, The Visualization Toolkit: An Objective-Oriented Approach To 3D Graphics, http://public.kitware.com/VTK/.
[26]C. G. Broyden, "The convergence of a class of double-rank minimization algorithms 2, the new algorithm," J. Inst. Math. Appl. **6**, 222–231 (1970).
[27]R. Fletcher, "A new approach to variable-metric algorithms," Comput. J. **13**, 317–322 (1970).
[28]D. Goldfarb, "A family of variable-metric algorithms derived by variational means," Math. Comput. **24**, 23–26 (1970).
[29]D. F. Shanno, "Conditioning of quasi-Newton methods for function minimization," Math. Comput. **24**, 647–656 (1970).
[30]D. C. Liu and J. Nocedal, "On the limited memory BFGS method for large scale optimization," Math. Program. **45**, 503–528 (1989).
[31]E. Schreibmann and L. Xing, "Narrow band deformable registration of prostate magnetic resonance imaging, magnetic resonance spectroscopic imaging, and computed tomography studies," Int. J. Radiat. Oncol. Biol. Phys. **62**, 595–605 (2005).
[32]W. E. Lorensen and H. E. Cline, "Marching cubes: A high resolution 3D surface construction algorithm," ACM Comput. Graph. **21**, 163–169 (1987).
[33]W. Schroeder, J. Zarge, and W. E. Lorensen, "Decimation of triangle meshes," Comput. Graph. **26**, 65–70 (1992).
[34]E. Rietzel, G. T. Chen, N. C. Choi, and C. G. Willet, "Four-dimensional image-based treatment planning: Target volume segmentation and dose calculation in the presence of respiratory motion," Int. J. Radiat. Oncol. Biol. Phys. **61**, 1535–1550 (2005).
[35]J. West *et al.*, "Comparison and evaluation of retrospective intermodality image registration techniques," Proc. SPIE **2710**, 332–347 (1996).
[36]W. Lu, G. H. Olivera, Q. Chen, M. Chen, and K. J. Ruchala, "Automatic re-contouring in 4D radiotherapy," Phys. Med. Biol. **51**, 1077–1099 (2006).

Int. J. Radiation Oncology Biol. Phys., Vol. 70, No. 2, pp. 599–608, 2008

0360-3016/08/$–see front matter

ELSEVIER

doi:10.1016/j.ijrobp.2007.09.057

PHYSICS CONTRIBUTION

AUTOMATED CONTOUR MAPPING WITH A REGIONAL DEFORMABLE MODEL

MING CHAO, PH.D., TIANFANG LI, PH.D., EDUARD SCHREIBMANN, PH.D., ALBERT KOONG, M.D., AND LEI XING, PH.D.

Department of Radiation Oncology, Stanford University School of Medicine, Stanford, CA

Purpose: To develop a regional narrow-band algorithm to auto-propagate the contour surface of a region of interest (ROI) from one phase to other phases of four-dimensional computed tomography (4D-CT).

Methods and Materials: The ROI contours were manually delineated on a selected phase of 4D-CT. A narrow band encompassing the ROI boundary was created on the image and used as a compact representation of the ROI surface. A BSpline deformable registration was performed to map the band to other phases. A Mattes mutual information was used as the metric function, and the limited memory Broyden-Fletcher-Goldfarb-Shanno algorithm was used to optimize the function. After registration the deformation field was extracted and used to transform the manual contours to other phases. Bidirectional contour mapping was introduced to evaluate the proposed technique. The new algorithm was tested on synthetic images and applied to 4D-CT images of 4 thoracic patients and a head-and-neck Cone-beam CT case.

Results: Application of the algorithm to synthetic images and Cone-beam CT images indicates that an accuracy of 1.0 mm is achievable and that 4D-CT images show a spatial accuracy better than 1.5 mm for ROI mappings between adjacent phases, and 3 mm in opposite-phase mapping. Compared with whole image–based calculations, the computation was an order of magnitude more efficient, in addition to the much-reduced computer memory consumption.

Conclusions: A narrow-band model is an efficient way for contour mapping and should find widespread application in future 4D treatment planning.

Deformable model, Image registration, Contour mapping, IGRT.

INTRODUCTION

Segmentation of a region of interest (ROI), such as a tumor target volume or a sensitive structure, is an important but time-consuming task in radiotherapy (1–6). With the emergence of four-dimensional (4D) imaging and adaptive radiotherapy, the need for efficient and robust segmentation tools is even increasing (7–11). Because of dramatically increased numbers of images, it becomes impractical to manually segment the ROIs slice by slice as in current three-dimensional radiotherapy practice. A natural solution to the 4D computed tomography (4D-CT) segmentation problem is to delineate the ROIs on a selected phase and then propagate the contours onto other phases using a mathematical model. Along this line, deformable model–based contour mapping has been implemented by a few groups (12–14). Although feasible, the calculation is global in nature and thus computationally intensive. In addition, the accuracy of the mapped contours may be compromised because the registration may be influenced unnecessarily by the image content distant from the ROIs, which would otherwise be irrelevant to the contour mapping process. This is especially problematic when nonlocal deformable models, such as thin plate spline and elastic model, are used. In general, contour mapping is a regional problem, and a global association of the phase-based images is neither necessary nor efficient.

Surface mapping techniques (15–17) represent a competitive alternative to the deformable model–based approach. The idea of surface mapping is to obtain contour transformation by iteratively deforming the ROI contour-extended surface until the optimal match with the reference is found. The calculation involves only the surface region and is thus computationally efficient. Numerous surface mapping techniques have been developed in the past, which include, to name a few, spatial partitioning, principal component analysis, conformal mapping, rigid affine transformation, deformable contours, and warping based on the thin-plate spline. All of

Reprint requests to: Lei Xing, Ph.D., Department of Radiation Oncology, Stanford University School of Medicine, 875 Blake Wilbur Drive, Stanford, CA 94305-5847. Tel: (650) 498-7896; Fax: (650) 498-4015; E-mail: lei@reyes.stanford.edu

Supported in part by grants from the Department of Defense (W81XWH-06-1-0235 and W81XWH-05-1-0041), Komen Breast Cancer Foundation (BCTR0504071), and National Cancer Institute (5R01 CA98523 and 1 R01 CA98523).

Conflict of interest: none.

Acknowledgment—The authors thank Dr. B. Loo from Stanford University for useful discussions.

Received March 12, 2007, and in revised form Sept 18, 2007. Accepted for publication Sept 27, 2007.

these techniques are a mapping between topologic components of the input surfaces that allow for transfer of annotations. Although the calculations are inherently efficient, the results depend heavily on the model used, which may not be generally applicable for all clinical situations because the ROI surface is multidimensional and hardly modeled by only a few parameters.

In this work, we present a novel regional algorithm for ROI propagation among different 4D-CT phases. The deformation of an ROI contour-extended surface in our algorithm is not driven by an *ad hoc* surface-based model but instead by the image features in the neighborhood of the surface. The underlying hypothesis here is that information contained in the ROI boundary region is sufficient to guide the contour mapping process. In the proposed algorithm the neighborhood image features of an ROI are captured by a narrow band, which is composed of all points within two surfaces with the signed distances of ±d from the ROI boundary. The algorithm is a hybrid of the regional surface–based model and the global deformable registration–based approach. The combination takes advantage of the desirable features of each of these two techniques and provides a robust and computationally efficient contour propagation tool for 4D radiotherapy.

METHODS AND MATERIALS

Software platform

The proposed contour mapping algorithm was implemented using the Insight Toolkit (18) and the Visualization Toolkit (19), which are open source cross-platform C++ software toolkits sponsored by the National Library of Medicine.

Overview of the mapping process

Figure 1 depicts the overall contour mapping process. For a given 4D-CT image set, a selected phase, named the template phase, was selected, and the ROIs were manually delineated by a physician. The manually outlined contour was referred to as the template contour. A narrow band encompassing the template contour was created (see next section for details). A deformable mapping was then carried out to propagate the band from the template phase to other phases, referred to as target phases. Upon successful mapping of the band, the deformation field was used to transform the template contour to the target images.

Narrow-band representation of ROI contour

The contour manually segmented on an axial slice of the template image has a polygon shape, and the vertices of the polygon form the basis for constructing the narrow band. As schematically shown in Fig. 2, a band with signed distances ±d was placed along the template contour. The regional image features contained in the band function serve as a ''signature'' of the contour and drive the contour mapping process. The distance between the neighboring vertices on the contour is typically 2–10 mm, depending on the shape of the contour. In generating the narrow band, we first created cubes with a side length of 2d around all the vertices, as depicted by points A and B in Fig. 2. To obtain a smooth band, between A and B three more cubes, centered at points C, D, and E, were inserted. Point C was chosen to be the middle point between A and B, point D the middle between A and C, and point E the middle between C and

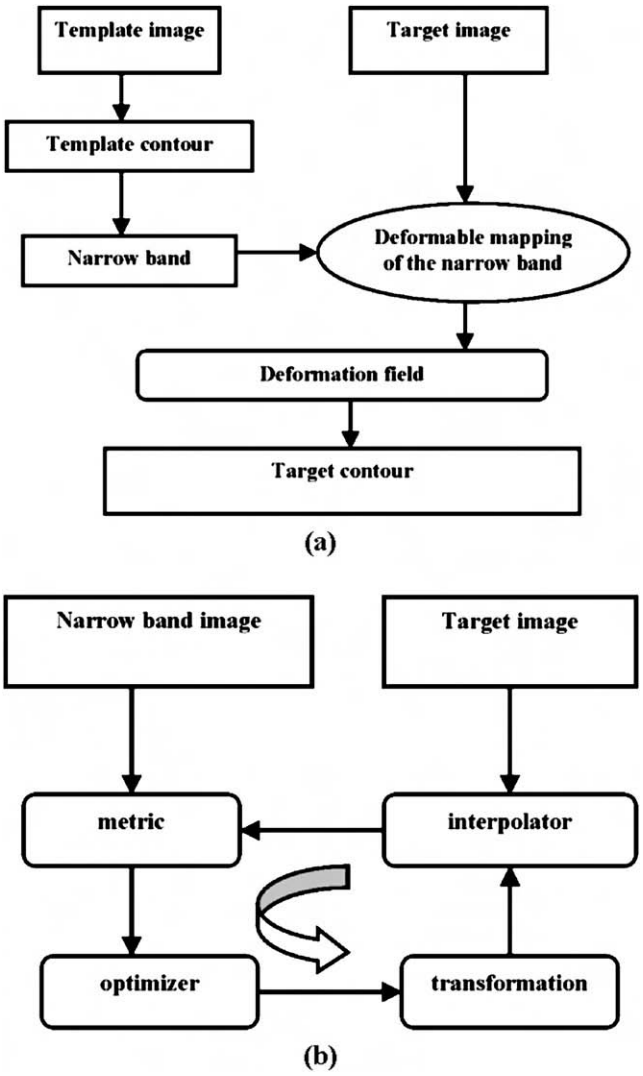

Fig. 1. Flow chart of narrow band–based contour mapping procedure. (a) Overall calculation process. (b) Deformable mapping process of the narrow band.

B. More interpolated vertex points can be introduced similarly when needed. Figure 3 illustrates a narrow band surrounding the lung boundary on the template phase CT image. The light green area stands for the narrow band, and the green curve is the manual contour. The width of the narrow band was set to be 2d = 15 mm in our calculations. To examine the robustness of the proposed mapping algorithm, a variety of other bandwidths, ranging from 4 mm through 30 mm, were also tested for one of the clinical cases.

Contour propagation

As illustrated in Fig. 1, the process of contour mapping is essentially to warp the narrow band constructed above in such a way that its best match in the target image is found. Mathematically, the mapping process of the narrow band constitutes an optimization problem, in which a group of transformation parameters that transform the points within the band in the template phase to their homologous points in the target image. The warping of the narrow band is quantified by a metric function, which ranks a trial matching based on the ''accordance'' level of the image content of the band and its correspondence in the target image. The calculation process is detailed below.

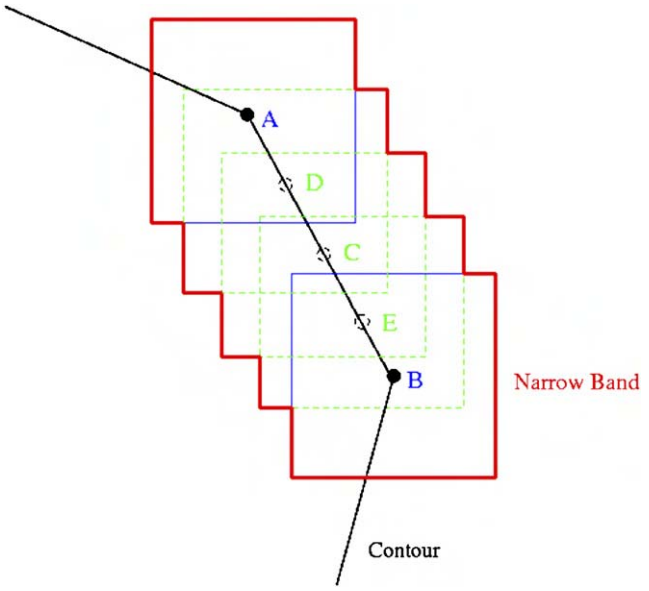

Fig. 2. A schematic drawing of narrow-band construction.

The input to the contour mapping software includes the narrow band and the whole target image, which are described by the image intensity distributions $\mathbf{I}_a(\mathbf{x})$ and $\mathbf{I}_b(\mathbf{x})$, respectively. It is worth emphasizing that, even though the whole target image was used, only fractional voxels in the target image (the voxels encompassed by the band) are involved in each iteration (a subregion surrounding the ROI on the target image could be created and used in the calculation, but the algorithm converged so fast that after two to three iterations the searching was quickly confined in the neighborhood of the optimal solution). The narrow band acts as a representation of the ROI contour. The task is to find the transformation matrix, $\boldsymbol{T}(\mathbf{x})$, that maps an arbitrary point in the band to the corresponding point on the target image (or *vice versa*) so that the best possible correspondence, as measured by the metric function, is achieved. The calculation proceeds iteratively. A BSpline deformable model is used to model the deformation of the band, but other models should also be applicable. The spacing between the BSpline nodes was chosen to be approximately 0.5 cm (smaller spacing was tested, but no significant difference was found in the final registration results). The displacement of a node i is specified by a vector $\mathbf{x}_i$, and the displacement vectors (20) of a collection of nodes characterize the tissue deformation. The displacement at a location $\mathbf{x}$ on the image is deduced by a BSpline polynomial fitting.

The Mattes Mutual Information (MMI) (21) was used as the metric function for narrow-band mapping (22–25). The central concept

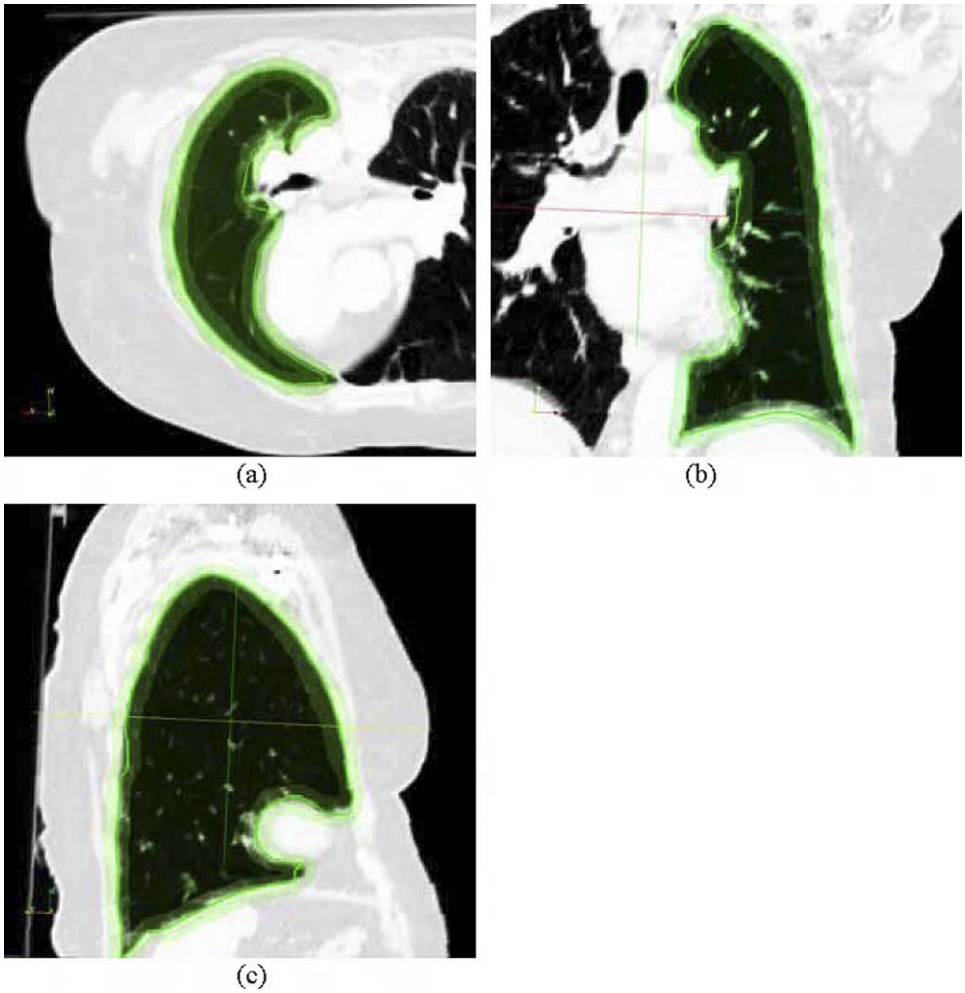

Fig. 3. Computed tomographic images with manual contours and the narrow bands for patient 1. The narrow bands are shown in light green and the contours are green curves. (a) Transverse view; (b) coronal view; (c) sagittal view.

of mutual information (MI) is the calculation of entropy. For an image A, the entropy is defined as

$$H\left(A\right) = -\int p_A(a)\log\, p_A(a)da,$$

where $p_A(a)$ (also called the marginal probability density function [PDF]) is the probability distribution of grey values (image intensities), which is estimated by counting the number of times each grey value occurs in the image and dividing those numbers by the total number of occurrences. Given two images, A and B, their joint entropy is

$$H\left(A,B\right) = -\iint p_{AB}(a,b)\log\, p_{AB}(a,b)dadb,$$

where $p_{AB}(a,b)$ is the joint PDF defined by a ratio between the number of grey values in the joint histogram (feature space) of two images and the total entries (26). The mutual information is generally expressed as

$$MI(A,B) = H(A) + H(B) - H(A,B).$$

Mutual information measures the level of information that a random variable (e.g., $\mathbf{I}_a(\mathbf{x})$) can predict about another random variable (e.g., $\mathbf{I}_b(\mathbf{x})$). Different from the conventional MI, whereby two separate intensity samples are drawn from the image, the Mattes implementation, MMI, uses only one set of intensity to evaluate both the marginal and joint PDFs at discrete positions or bins that uniformly spread within the dynamic range of the images. Entropy values were computed by summing over all the bins. The number of bins used to compute the entropy in MMI metric evaluation was chosen to be 30, and the number of spatial samples used was 20,000. Details of MMI implementation can be found in Mattes *et al.* (21).

The limited memory Broyden-Fletcher-Goldfarb-Shanno algorithm (L-BFGS) (27–29) was used to optimize the MMI metric function with respect to the displacement parameters of the nodes, $\{\mathbf{x}_i\}$, to find the transformation matrix $\boldsymbol{T}(\mathbf{x})$ that relates the points on image A and image B. Here we just briefly show the algorithm. Starting from a positive definitive approximation of the inverse Hessian $\mathbf{H}_0$ at $\mathbf{x}_0$, L-BFGS derives the optimization variables by iteratively searching through the solution space. At an iteration k, the calculation proceeds as follows: [*1*] determine the descent direction $\mathbf{p}_k = -\mathbf{H}_k \nabla f(\mathbf{x}_k)$; [*2*] line search with a step size $\alpha_k = \overset{\arg\min}{\alpha \geq 0} f\left(\mathbf{x}_k + \alpha \mathbf{p}_k\right)$, where α is the step size defined in the L-BFGS software package; [*3*] update $\mathbf{x}_{k+1} = \mathbf{x}_k + \alpha_k\, \mathbf{p}_k$; and [*4*] compute $\mathbf{H}_{k+1}$ with the updated $\mathbf{H}_k$.

At each iteration a backtracking line search is used in L-BFGS to determine the step size of movement to reach the minimum of f along the ray $\mathbf{x}_k + \alpha \mathbf{p}_k$. For convergence α has to be chosen such that a sufficient decrease criterion is satisfied, which depends on the local gradient and function value and is specified in L-BFGS by the Wolfe conditions (27). During the course of optimization, the above iterative calculation based on L-BFGS algorithm continues until the following stopping criterion is fulfilled:

$$\frac{\|\nabla f(\mathrm{x}_k)\|_2}{\max(1, \|\mathrm{x}_k\|_2)} < \varepsilon$$

or a pre-set maximum number of iterations is reached. In this study we set $\varepsilon = 10^6$ and the iteration number to 200, but no more than 100 iterations were exceeded in all our calculations for the algorithm to converge.

Evaluation of algorithm performance

Evaluation of a contour mapping algorithm is a difficult task because of the lack of the ground truth for comparison. A straightforward means of evaluation is the visual inspection of the mapped contours. In addition to this, evaluation based on synthetic images (digital phantoms) is also commonly used. The images and existing contours are distorted with preset deformation fields. Because the gold standard is known, a direct comparison with the mapped contour is made so as to assess the propagation algorithm quantitatively. Beside these two methods, we further performed a bidirectional mapping to evaluate the proposed algorithm. In this test, the reverse of the original contour mapping was performed: the mapped contours on the target phase were treated as the template contours and mapped back to the original template phase. The contours so obtained were then compared with the original manual contours, and the difference between the two sets of contours was quantified. The difference between the resultant and template contours was measured in terms of the displacements of the vertex points on the two contours. The last yet pragmatic evaluation of the algorithm performance on patient's study was based on the physician's manual contours.

Case study

Four thoracic cancer patients, named as patient 1, 2, 3, and 4, were first used to test the proposed algorithm. These patients underwent 4D-CT scans. The 4D-CT images were acquired with a GE Discovery-ST CT scanner (GE Medical System, Milwaukee, WI). The collected data were sorted into 10 phase bins. The ROIs on the template phase were manually segmented by a physician. Specifically, for patients 1 and 2, the inhale phase was chosen for manual segmentation, and for patients 3 and 4, the exhale phase. Different ROIs were used to better evaluate the algorithm. Lungs were selected from patients 1, 2, and 3 and gross tumor volume (GTV) from patient 4. Figure 3 illustrates the manual contour and narrow band representation for the lung from patient 1. Contour is shown in the green curve together with the regional narrow bands (light green area) on the transverse, coronal, and sagittal views (Figs. 3a, 3b, and 3c, respectively).

To further assess the robustness of the proposed algorithm, we also carried out the contour propagation calculation from planning CT to Cone-beam CT (CBCT) for a head-and-neck case. The CBCT images were acquired using the Varian Trilogy system (Varian Medical Systems, Palo Alto, CA).

RESULTS

Convergence analysis

To better illustrate the iterative process of the contour propagation, in Fig. 4 the MMI metric as a function of iteration step is plotted for the narrow band mapping from the first phase (inhale phase) to the other nine phases for the first thoracic patient. In all nine calculations it is seen that the metric value decreases monotonically as the iteration proceeds. However, the number of iterations needed for the algorithm to find the optimal solution varies. It is interesting to observe that, for an ''easier'' mapping whereby the deformation between the two phases is small, the number of iterations required is less, whereas for ''tougher'' ones with larger differences in ROI shapes, the required number of iterations increases drastically. Indeed, from Fig. 4 it is seen that the minimum number of iterations required for the metric to saturate occurs when mapping the phase 1 to the adjacent

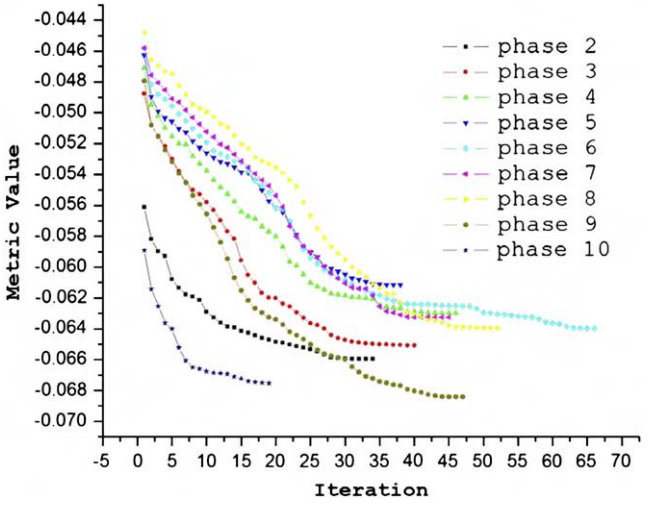

Fig. 4. Narrow-band metric values as a function of iteration step when mapping the narrow band from phase 1 to the other nine phases of the four-dimensional computed tomography.

phases, 2 and 10. For other mapping, the required iteration increases and reaches its largest value for the ''toughest'' mapping between inhale and exhale (phase 5) phases.

In the above analysis, the bandwidth was set to be 15 mm. The performance of the proposed algorithm was also evaluated by varying the width in the range of 4 mm and 30 mm. Specifically, we tried the widths of 4 mm, 8 mm, 10 mm, 15 mm, 20 mm, and 30 mm. Our results revealed that, when the band was too narrow (e.g., 4 mm), the mapping may fail locally at a place not containing sufficient neighborhood image features. The situation is improved dramatically as the bandwidth increases. For all the clinical cases studied here, no single failure was observed for a width of 15 mm. When the width is too large, the whole ROI will be included in the band. In this situation, the mapping becomes equivalent to registering the whole image and the advantage of the narrow band will be overshadowed by the dramatically increased memory and computing costs. Our experience indicates that a width of 10–15 mm provides a fine balance between the computational accuracy and the associated cost.

We found that the overall computing time was increased by roughly an order of magnitude when going from the narrow band approach to the conventional deformable model–based contour mapping, say, approximately 3 min for narrow band–based mapping vs. approximately 25 min for whole image–based mapping. The dramatically increased computer memory requirement in the latter case also posts a serious problem when developing a clinically practical contour propagation method for 4D radiotherapy.

Algorithm performance evaluation

In addition to visual inspect, the proposed algorithm was assessed by a series of synthetic images or digital phantoms. Typically, a thoracic CT image together with the contour was distorted with the intentionally introduced deformation, and then the contour was propagated onto the distorted image. A quantitative comparison was carried out. The mean and maximum separation between the gold standard and the mapped contours were found to be 1.0 mm and 1.5 mm, respectively. Figure 5 shows one example of digital phantom experiments.

The performance of the proposed algorithm was further evaluated by the bidirectional mapping calculation outlined in Methods and Materials. A template contour at phase 1 was first mapped to phases 3 and 6. The mapped contours were then treated as the ''starting contours'' and mapped back to phase 1. The two back-mapped contours were compared with the original template contour. The displacement of each back-mapped vertex point relative to its original locations was computed, and a mean value of 0.8 mm was found for the bidirectional mapping between phases 1 and 3 and 1.8 mm between phases 1 and 6. The larger displacement in the latter situation was due to the fact that, computationally, it is more difficult to map between two opposite phases, such as inhale and exhale phases, owing to larger organ deformations. Overall, the observed displacement is comparable to the pixel size, indicating that the mapping is accurate and robust.

Thoracic patient study results

Figure 6 shows the contour mapping results for the first clinical case. The results are presented in axial, coronal, and sagittal planes for phases 2 (Fig. 6a–c), 6 (Fig. 6d–f), 8 (Fig. 6g–i), and 10 (Fig. 6j–l). For phases 2 and 10, which are immediately adjacent to the inhale phase, the deformation is relatively small and the mapped contours conform to the ROI boundary very well. This represents the ''easy'' mapping situation and is consistent with the analysis presented above. The average error was less than 1.5 mm. For a ''remote'' phase, such as phase 6 shown in Fig. 6d–f, more

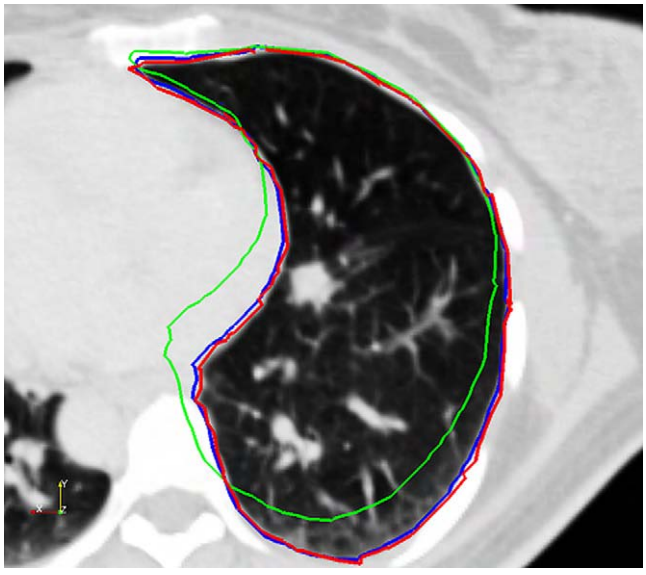

Fig. 5. Synthetic image and overlaid contours. The original contour is depicted in green, gold standard contour in blue, and the mapped contour in red.

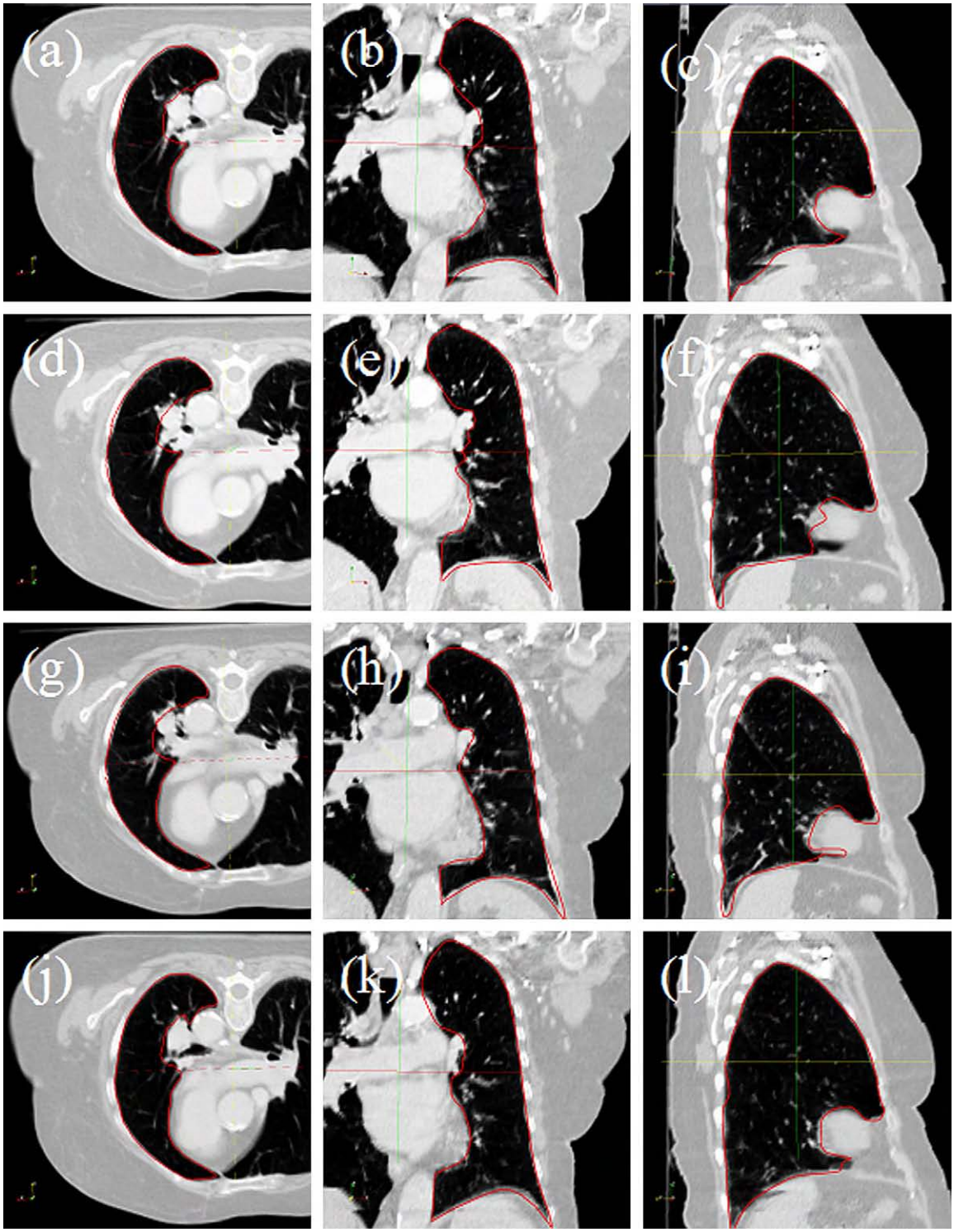

Fig. 6. Computed tomographic images and mapped contours for thoracic patient 1. Displayed are selected phases. From the top row to bottom, phases 2, 6, 8, and 10 are presented, respectively. For each phase, transverse, coronal, and sagittal views are shown from left to right.

iterations were entailed to find the optimal solution, and the resultant contours tend to be worse as compared with those phases adjacent to phase 1. According to the bidirectional mapping, the average mapping error for phase 6 was estimated to be less than 3 mm. The mapped GTV contours (in red) together with manual contours (in blue) by a physician for phases 1, 4, 8, and 10 in the study of patient 4 are shown in Fig. 7 (parts a, b, d, and e, respectively). The template phase (phase 6) with the template manual contour (in green) is shown in Fig. 7c. In addition, the template manual contour from this phase was overlaid on all the displayed phases. For phases 4 and 8 the deformation was relatively

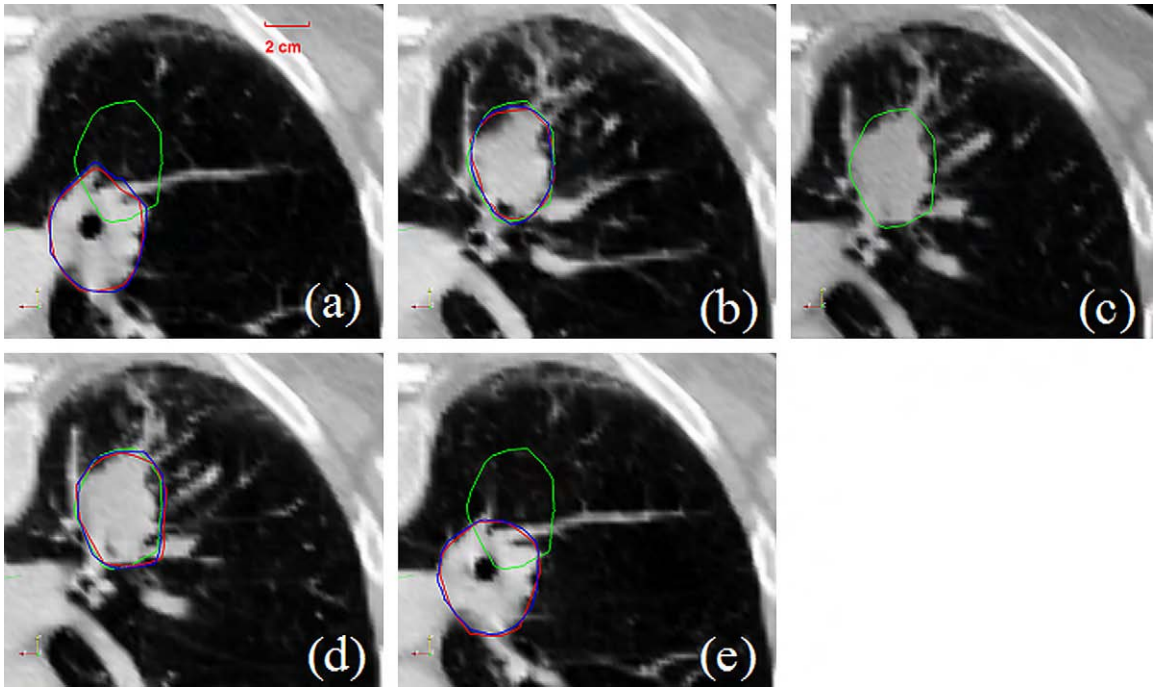

Fig. 7. Axial view of computed tomographic images with gross tumor volume contours for the fourth thoracic patient. (a), (b), (c), (d), and (e) correspond to phases 1, 4, 6 (template phase), 8, and 10, respectively. The green curves are the manually outlined template contour from phase 6, and the red curves represent the contours after warping. The manual contours (in blue) by a physician on individual phases were also displayed.

small (the manual contour was delineated on phase 6), and fewer iterations were needed to find the optimal bands on the target images. For phases 1 and 10, whereby deformation was significant in the ROIs although more computing load was necessary, a good result was still achieved with our narrow-band technique. Comparisons between the mapped contours and the manually segmented contours by physicians for these patients were also performed, and results revealed a similar level of accuracy (maximum and mean values of the discrepancy between the two sets of contours are 2.8 mm and –0.9 mm, respectively).

As a useful application of the proposed technique, in Fig. 8 we present the mean and maximum lung displacements of contour vortices for each breathing phase relative to their locations on the template phase. As seen in Fig. 8, the overall behavior of the mean and maximum displacements is consistent with our intuitive expectation. For cases 1 and 2, the inhale phase (phase 1) was manually segmented, thus the displacement for that phase is zero. For other phases, both mean and maximum displacement values vary with the breathing phase and reach their maxima at the opposite phase. For case 3 the exhale phase was manually segmented, and the behavior was thus opposite to cases 1 and 2. In general, an average displacement of approximately 3 mm was found for inhale and exhale phases. A slight digression is noticed in phase 7 of patient 1, which may be caused by 4D-CT binning artifacts. This type of data is particularly useful in determining the patient-specific tumor margin to account for breathing motion of the tumor target.

Contour propagation in a head-and-neck case

The results of contour mapping for the head-and-neck case are summarized in Fig. 9. Figure 9a shows the planning CT along with manually delineated contours, and Fig. 9b displays the mapped contours of the body, mandible, and GTV on CBCT. For body and mandible a simple rigid mapping is enough to achieve high accuracy. For the GTV, however, the proposed deformable registration model was necessary to adequately propagate the contour. A visual inspection of the propagated contours suggests that the mapping is clinically acceptable.

DISCUSSION

Four-dimensional CT image segmentation represents a necessary step in constructing a 4D patient model and computing the accumulated dose in 4D radiotherapy. A natural way to tackle the problem is to auto-map the manually delineated contours on one of the phases to the remaining phases. In this work, a regional computing algorithm was introduced to deal with the issue. The approach relies on the assumption that a narrow band surrounding the manually segmented contour can capture sufficient information to drive the finding of its counterparts in other phases of the 4D-CT. Obviously, this assumption is valid when the band is sufficiently wide so that a large number of voxels are involved in the registration calculation. As demonstrated by the presented data, the registration and the mapping are reliable when the bandwidth is larger than 4 mm. Computationally, the proposed approach

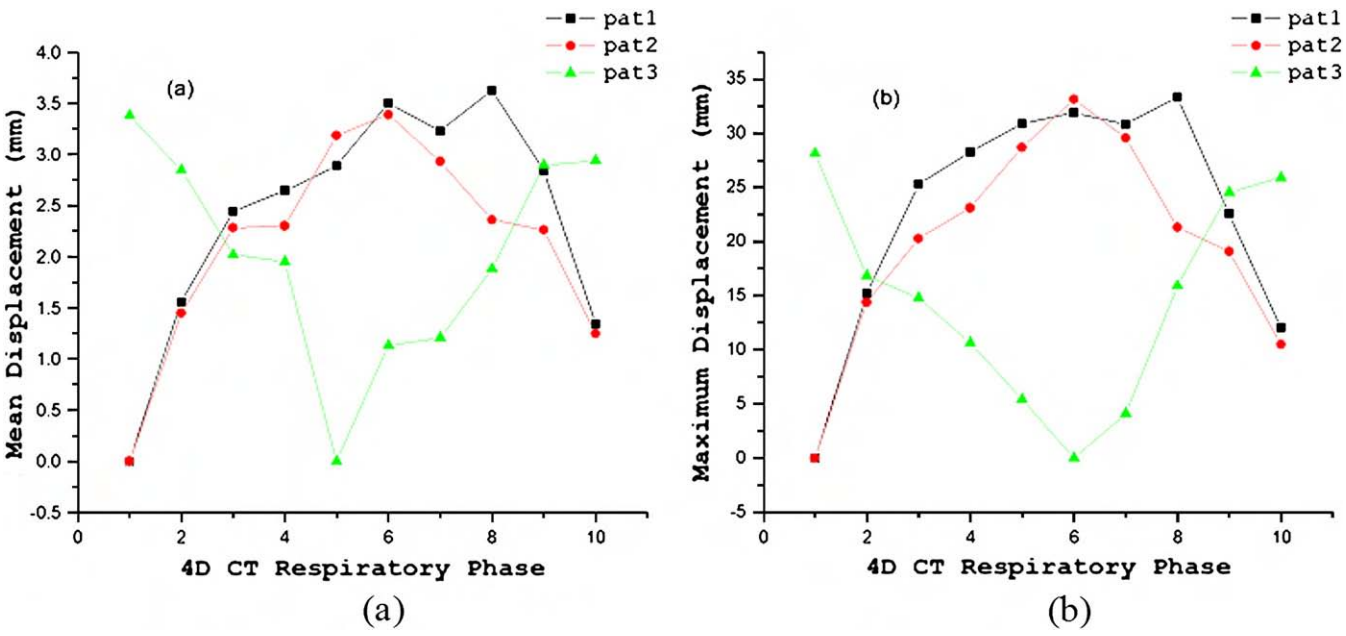

Fig. 8. Displacement of region of interest boundary points as a function of respiration phase for three thoracic patients. (a) Mean displacement vs. phase. (b) Maximum displacement vs. phase. 4D CT = four-dimensional computed tomography.

resides between a deformable model–based mapping and a surface model–based ROI contour mapping.

The success of the image content–based approaches, such as the proposed narrow-band approach or conventional deformable image registration, arises from the fact that they fully utilize the inherent image features of the two input images. The narrow band–based technique is particularly attractive because it takes advantages of the useful features of both image content–based technique and the regional surface–based model. In a sense, it is a hybrid approach of the two distinct types of algorithms. The narrow-band approach utilizes the imaging features surrounding the ROI to guide the search of the optimal mapped contours while considering the shape integrity of the ROI surface. It eliminates the need for a global registration of the input images and thus greatly increases the computational efficiency.

Application of the proposed contour mapping technique to five clinical cases indicates that the technique is accurate and computationally efficient. A common problem in image segmentation and contour mapping studies is the lack of quantitative validation. In the studies of Lu *et al*. (13) and Schriebmann *et al*. (14), for example, the accuracy of a deformable model–based contour mapping technique was evaluated purely on the basis of visual inspection. Although it is a convenient way for rapid assessment of a segmentation calculation, especially in a case in which the ''ground truth'' contours do not exist, the method falls short in quantization. The same approach was used in many other previous

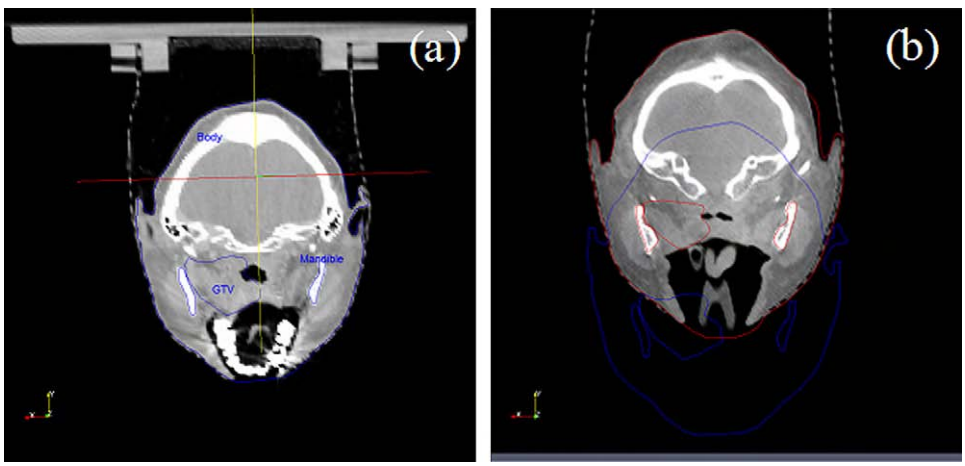

Fig. 9. Contour propagation in a head-and-neck case. (a) Planning computed tomography with manually outlined template contours (in blue) for body, mandible, and gross tumor volume. (b) Cone-beam computed tomography along with contours after warping (in red) for the corresponding structures.

investigations (1, 5, 14, 30). In this study, a bidirectional contour mapping was proposed to examine the reliability and robustness of a contour mapping technique. This method provides a useful test in assessing the success of a contour propagation algorithm. We would like to point out that the bidirectional mapping technique introduced in this work is a necessary (but not sufficient) test. In a rare but possible situation, the bidirectional mapping may not be able to find that an error occurred in the narrow-band mapping process. A visual inspection of the mapped result may help in this situation. On the basis of the bidirectional mapping experiments and visual inspection for the patient studies, we conclude that the proposed approach can perform very well even in the presence of significant deformations.

In our calculation, we observed that the regular grid of BSpline control points could be mapped to a region outside the narrow band. Although it seems that this does not directly affect the accuracy of the method, it may prolong the calculation by computing the displacements in regions where metric information is irrelevant. Setups have been proposed to adapt the splines control mesh to regions where deformation is found to be significant (31), and the extension of the method would allow us to use the BSpline control points defined only in the regions within the narrow band. Implementation of this type of technique should further reduce the computation time required to find the optimal solution.

Although there are numerous deformable algorithms, including, for example, the elastic model (32–34), viscous fluid model (35), optical flow model (5,30,36), finite element model (33, 37), and radial basis function models such as the basis spline model (28, 38, 39) and thin plate spline model (40–43), a truly robust tool suitable for routine clinical applications is yet to be developed. Each of these approaches has its pros and cons. The deformable calculation can be greatly facilitated if some *a priori* system information can be incorporated. Along this line, the homologous correspondence of the bony structure in two input images has been incorporated in thin plate spline method, and remarkable improvement has resulted (44). The narrow band–generated ROI contour correspondence could also be used as prior knowledge to improve a deformable registration. This work is still in progress and will be reported in the future.

CONCLUSIONS

In this work we have developed a regional deformable registration–based method to auto-propagate contours for 4D radiotherapy. The central idea is that a narrow band encompassing an ROI surface carries the neighborhood information of the ROI surface and can be used to establish a reliable association between the ROIs in two phase-specific image sets. Different from other type of regional algorithms, such as surface mapping, the method uses the image features captured in a band to guide the search for the optimal contour mapping. Compared with conventional deformable image registration–based approaches, a great reduction in computational burden and a large capture radius in optimization space result. Our study demonstrated that the information contained in the boundary region can be used to guide the contour mapping in all the testing cases presented in this article. The proposed regional model decreases the workload involved in 4D-CT ROI segmentation and provides a valuable tool for the efficient use of available spatial–temporal information for 4D simulation and treatment planning.

REFERENCES

1. Pekar V, McNutt TR, Kaus MR. Automated model-based organ delineation for radiotherapy planning in prostatic region. *Int J Radiat Oncol Biol Phys* 2005;60:973–980.
2. Kass MR, WitKen A, Terzopoulos D. Snakes: Active contour models. *Int J Comput Vis* 1988;4:321–331.
3. Coote T, Hill A, Taylor C, *et al*. The use of active shape models for locating structures in medical images. *J Image Vis Comput* 1994;12:355–366.
4. Xu C, Prince JL. Snakes, shapes, and gradient vector flow. *IEEE Trans Image Process* 1998;7:359–369.
5. Liu F, Zhao B, Kijewski PK, *et al*. Liver segmentation for CT images using GVF snake. *Med Phys* 2005;32:3699–3706.
6. Weese J, Kaus MR, Lorenz C, *et al*. Shape constrained deformable models for 3D medical image segmentation. In: Insana MF, Leahy RM. Information processing in medical imaging: 17th International Conference, IPMI 2001, Davis, CA, USA, June 18–22, 2001. *Lecture Notes in Computer Science* 2001; 2082:380–387.
7. Li T, Schreibmann E, Thorndyke B, *et al*. Radiation dose reduction in four-dimensional computed tomography. *Med Phys* 2005;32:3650–3660.
8. Vedam SS, Keall PJ, Kini VR, *et al*. Acquiring a four-dimensional computed tomography dataset using an external respiratory signal. *Phys Med Biol* 2003;48:45–62.
9. Dietrich L, Jetter S, Tucking T, *et al*. Linac-integrated 4D cone beam CT: First experimental results. *Phys Med Biol* 2006;51: 2939–2952.
10. Li T, Xing L, Munro P, *et al*. Four-dimensional cone-beam computed tomography using an on-board imager. *Med Phys* 2006;33:3825–3833.
11. Rietzel E, Chen GT, Choi NC, *et al*. Four-dimensional image-based treatment planning: Target volume segmentation and dose calculation in the presence of respiratory motion. *Int J Radiat Oncol Biol Phys* 2005;61:1535–1550.
12. Gao S, Zhang L, Wang H, *et al*. A deformable image registration method to handle distended rectums in prostate cancer radiotherapy. *Med Phys* 2006;33:3304–3312.
13. Lu W, Olivera GH, Chen Q, *et al*. Automatic re-contouring in 4D radiotherapy. *Phys Med Biol* 2006;51:1077–1099.
14. Schreibmann E, Chen GT, Xing L. Image interpolation in 4D CT using a BSpline deformable registration model. *Int J Radiat Oncol Biol Phys* 2006;64:1537–1550.
15. Chakraborty A, Staib LH, Duncan JS. An integrated approach for surface finding in medical images. In: IEEE workshop mathematical methods in biomedical image analysis. Los Alamitos, CA: IEEE Computer Society Press; 1996. p. 253–262.
16. McInerney T, Terzopoulos D. Deformable models in medical image analysis. *Med Image Anal* 1996;1:91–108.

17. Montagnat J, Delingette H, Ayache N. A review of deformable surfaces: Topology, geometry and deformation. *Image Vis Comput* 2001;19:1023–1040.
18. Ibanez L, Schroeder W, Ng L. ITK software guide. Clifton Park, NY: Kitware; 2003.
19. Schroeder W, Martin K, Lorensen B. The visualization toolkit: An object-oriented approach to 3D graphics. 4th edition. Kitware: Clifon Park, NY; 2006.
20. Chao M, Schreibmann E, Li T, *et al*. Knowledge-based autocontouring in 4D radiation therapy. *Med Phys* 2006;33:2171.
21. Mattes D, Haynor DR, Vesselle H, *et al*. Non-rigid multi-modality image registration. In: Sonka M, Hanson KM, editors. *Medical imaging* 2001: *Image processing*. *Proceedings of SPIE* 2001;4322:1609–1620.
22. Woods RP, Cherry SR, Mazziotta JC. Rapid automated algorithm for aligning and reslicing PET image. *J Comput Assist Tomogr* 1992;16:620–633.
23. Woods RP, Mazziotta JC, Cherry SR. MRI-PET registration with automated algorithm. *J Comput Assist Tomogr* 1993;17: 536–546.
24. Collingnon A, Maes F, Delaere D, *et al*. Automated multimodality image registration based on information theory. In: Bizais Y, Barillot C, Paola RD, editors. Information processing in medical imaging. Dordrecht, The Netherlands: Kluwer; 1995. p. 263–274.
25. Wells WM III, Viola P, Kikinis R. Multi-modal volume registration by maximization of mutual information. *Med Image Anal* 1996;1:35–51.
26. Pluim JP, Maintz JB, Viergever MA. Mutual-information-based registration of medical images: A survey. *IEEE Trans Med Imaging* 2003;22:986–1004.
27. Liu DC, Nocedal J. On the limited memory BFGS method for large scale optimization. *Math Program* 1989;45:503–528.
28. Schreibmann E, Yang Y, Boyer A, *et al*. Image interpolation in 4D CT using a BSpline deformable registration model. *Med Phys* 2005;32:1924.
29. Schreibmann E, Xing L. Narrow band deformable registration of prostate magnetic resonance imaging, magnetic resonance spectroscopic imaging, and computed tomography studies. *Int J Radiat Oncol Biol Phys* 2005;62:595–605.
30. Guerrero TM, Zhang G, Huang TC, *et al*. Intrathoracic tumour motion estimation from CT imaging using the 3D optical flow method. *Phys Med Biol* 2004;49:4147–4161.
31. Camara O, Colliot O, Delso G, *et al*. 3D nonlinear PET-CT image registration algorithm with constrained free-form deformations. In: Hamza MH, editor. Proceedings of the 3rd IASTED International Conference on Visualization, Imaging, and Image Processing. Calgary: ACTA Press; 2003. p. 516–521.
32. Bajcsy R, Kovacic S. Multiresolution elastic matching. *Comput Vis Graphics Image Processing* 1989;46:1–21.
33. Gee JC, Haynor DR, Reivich M, *et al*. Finite element approach to warping of brain images. *Proc SPIE Med Imaging* 1994; 2167:18–27.
34. Gee JC, Reivich M, Bajcsy R. Elestically deforming 3D atlas to match anatomical brain images. *J Comput Assist Tomogr* 1993; 17:225–236.
35. Christensen GE, Rabitt RD, Miller MI. Deformable templates using large deformable kinematics. *IEEE Trans Med Imaging* 1996;5:1435–1447.
36. Thirion JP. Image matching as the diffusion process: An analogy wth Maxwell's demons. *Med Image Anal* 1998;2:243–260.
37. Brock KM, Balter JM, Dawson LA, *et al*. Automated generation of a four-dimensional model of the liver using warping and mutual information. *Med Phys* 2003;30:1128–1133.
38. Schreibmann E, Xing L. Image registration with auto-mapped control volumes. *Med Phys* 2006;33:1165–1179.
39. Coselmon MM, Balter JM, McShan DL, *et al*. Mutual information based CT registration of the lung at exhale and inhale breathing states using thin-plate splines. *Med Phys* 2004;31: 2942.
40. Lian J, Xing L, Hunjan S, *et al*. Mapping of the prostate in endorectal coil-based MRI/MRSI and CT: A deformable registration and validation study. *Med Phys* 2004;31:3087–3094.
41. Brock KK, Hollister SJ, Dawson LA, *et al*. Technical note: creating a four-dimensional model of the liver using finite element analysis. *Med Phys* 2002;29:1403–1405.
42. Fei B, Kemper C, Wilson DL. A comparative study of warping and rigid body registration for the prostate and pelvic MR volumes. *Comput Med Imaging Graph* 2003;4:267–281.
43. Bookstein FL. Principlal warping: Thin plate splines and the decomposition of deformations. *IEEE Trans Pattern Anal Machine Intelligence* 1989;11:567–585.
44. Xie Y, Xing L. Incorporating a priori knowledge into deformable registration model [Abstract]. *Med Phys* 2007;34: 2333–2334.

Feature-based rectal contour propagation from planning CT to cone beam CT

Yaoqin Xie, Ming Chao, Percy Lee, and Lei Xing[a)]
Department of Radiation Oncology, Stanford University School of Medicine, Stanford, California 94305-5847

(Received 13 December 2007; revised 13 May 2008; accepted for publication 4 August 2008; published 12 September 2008)

The purpose of this work is to develop a novel feature-based registration strategy to automatically map the rectal contours from planning computed tomography (CT) (pCT) to cone beam CT (CBCT). The rectal contours were manually outlined on the pCT. A narrow band with the outlined contour as its interior surface was then constructed, so that we can exclude the volume inside the rectum in the registration process. The corresponding contour in the CBCT was found by using a feature-based registration algorithm, which consists of two steps: (1) automatically searching for control points in the pCT and CBCT based on the features of the surrounding tissue and matching the homologous control points using the scale invariance feature transformation; and (2) using the control points for a thin plate spline transformation to warp the narrow band and mapping the corresponding contours from pCT to CBCT. The proposed contour propagation technique is applied to digital phantoms and clinical cases and, in all cases, the contour mapping results are found to be clinically acceptable. For clinical cases, the method yielded satisfactory results even when there were significant rectal content changes between the pCT and CBCT scans. As a consequence, the accordance between the rectal volumes after deformable registration and the manually segmented rectum was found to be more than 90%. The proposed technique provides a powerful tool for adaptive radiotherapy of prostate, rectal, and gynecological cancers in the future. © *2008 American Association of Physicists in Medicine*. [DOI: 10.1118/1.2975230]

Key words: image guided radiation therapy (IGRT), image registration, deformable model, segmentation, scale invariance feature transformation (SIFT)

I. INTRODUCTION

Patients treated with radiotherapy for cancers such as prostate, rectal, and gynecological cancers experience large day-to-day changes in their rectal volumes due to motion, distention, and filling. Due to variations in the image content, an exact correspondence between two image sets acquired at different time points may not exist. Thus, any deformable model relying on the use of information contained in the entire image may not be adequate in dealing with these patients. The artifacts-induced disjoint between the images also makes the autopropagation of contours outlined in one set of images to another highly difficult with conventional strategies. With continued enthusiasm for adaptive radiotherapy, the ability to reliably and efficiently map the rectum outlined in the planning computed tomography (CT) (pCT) to the on-treatment cone beam CT (CBCT) images now becomes a bottleneck and needs to be resolved in order for many patients with cancer within the pelvis to benefit from the novel adaptive replanning strategy.[1,2]

The issue of rectal motion and deformation in conformal radiation therapy is described in various publications. Lee *et al.* evaluated the CBCT as a tool to quantify the accuracy and precision of a simulated IMRT treatment delivery model for rectal cancer when rectal motion due to filling and deformation was taken into account.[3] The mean deformation variation of 0.71 and 0.94 cm in the LAT and AP directions was reported. Foskey *et al.* shrank the rectal gas region to a virtual point in order to make the correspondence of the rectal volumes in two sets of images.[4] Gao *et al.* used an automatic image intensity modification procedure to create artificial gas pockets in the pCT images.[5] The major drawbacks of these types of approaches are the artificial introduction of image features within the rectal volume and the potentially inaccurate association of the artificial image features. As a consequence, the accordance between the rectal volumes after deformable registration and the manually segmented rectum was found to be less than 80%.

In this work, we propose to use the image information in the neighborhood outside the rectal wall as the driving force to guide the rectal contour propagation from the pCT to CBCT. Because the content in the region outside the rectal wall should be conserved, regardless of any changes in the rectal filling and distension, this strategy seems to be physically sensible. Coupled with a powerful feature-based deformable registration model, which identifies homologous tissue features shared by the pCT and CBCT images, the novel approach captures the key issues of the system and provides a natural solution to the above stated problem. Application of the proposed algorithm to a number of digital phantoms and clinical cases demonstrates that the technique is accurate and robust and may be useful for future adaptive therapy planning.

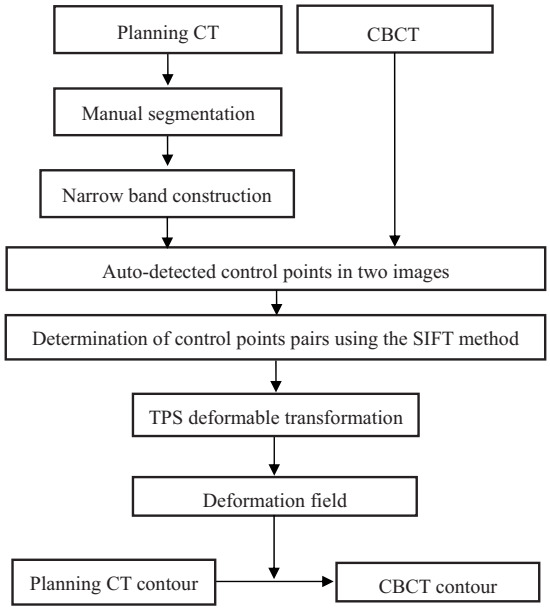

FIG. 1. Overall process of rectal contour propagation.

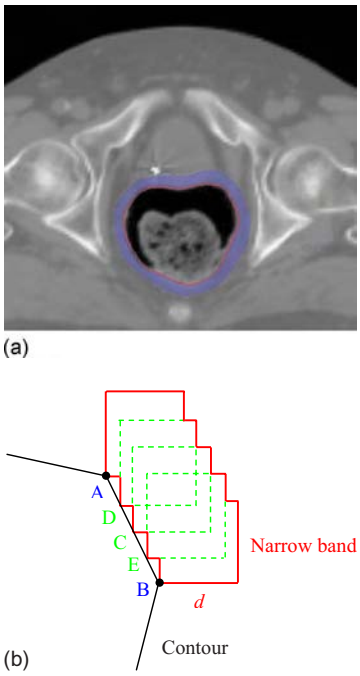

FIG. 2. A sketch of narrow band. (a) A narrow band image surrounding a manually segmented rectal contour and (b) a narrow band construction is illustrated for two vertex points A and B.

II. METHODS AND MATERIALS

II.A. Software platform

The proposed contour mapping algorithm was implemented using the Insight Toolkit[6] and the Visualization Toolkit (VTK),[7] which are open source cross-platform C++ software toolkits sponsored by the National Library of Medicine. They are freely available for research purposes (see Refs. 34 and 35). ITK provides various basic algorithms to perform registration and segmentation for medical images. The programs contained in ITK are highly extendable, making it an ideal platform for development of image registration and processing techniques. VTK is primarily used for image visualization (including contours).

II.B. Narrow band construction

Inconsistency in rectal contents between two input image sets could severely reduce the performance of a deformable registration algorithm. Coregistering an empty rectum without bowel gas to a rectum filled with bowel gas using any deformable model could be problematic, for example. A natural strategy is to exclude the volume inside the rectal wall. In practice, the template rectal contour in the pCT image has been manually contoured as a part of the routine treatment planning process, thus making it a straightforward matter to exclude the volume inside the rectal wall. Figure 1 shows the proposed contour mapping process. After manual segmentation on the pCT, a narrow band as sketched in Fig. 2 is constructed with the manually segmented rectum representing the inner surface of the band. On an axial slice, the contour has a polygon shape and the vertices of the polygon form the basis for constructing the narrow band. The distance between the neighboring vertices on the contour is typically 2–10 mm depending on the shape of the contour. In generating the narrow band, we first create squares with side length of d for each vertex, as depicted by points A and B in Fig. 2(b). In order to obtain a smooth band, between A and B three more squares, cornered at points C, D, and E, are inserted. Point C is chosen to be the middle point between A and B. Point D is the point between A and C, and point E is the point between B and C. More interpolated vertex points can be similarly introduced to obtain a smooth band. The principle of the narrow band diameter selection is to exclude most bony structures outside the narrow band, since the bony structures are rigid and heavily affect the control point selection. Meanwhile, the generated narrow band can capture sufficient information to drive the finding of its counterpart in the subsequent CBCT. In general, the size of the squares is therefore within 1 cm, so that the diameter of the narrow band is within 1.5 cm.

The narrow band in our approach is used as a compact representation of the rectal surface. As will be detailed in the next subsection, a feature-based deformable registration algorithm is employed to find the correspondence of the band in the CBCT images. Upon successful registration, the deformation field is utilized to propagate the pCT contour to the CBCT. Because only the image features outside the rectum are used, a narrow band shown in Fig. 2 permits us to take advantage of the regional information inside the narrow band yet avoiding the nuisance of rectum/bladder filling.

II.C. Feature-based warping of the narrow band

As illustrated in Fig. 1, the process of contour mapping is to warp the narrow band constructed above in such a way that its best match in the CBCT images is found. Mathematically, this constitutes an optimization problem, in which a

group of transformation parameters transform the points within the band in the pCT to their corresponding points in the CBCT. The input to the contour mapping software includes the narrow band and the CBCT images, which are described by the image intensity distributions $\mathbf{I}_a(\mathbf{x})$ and $\mathbf{I}_b(\mathbf{x})$, respectively.

To find the transformation matrix, $\mathbf{T}(\mathbf{x})$, that maps an arbitrary point in the band to the corresponding point in the CBCT images (or *vice versa*), a thin plate spline (TPS) deformable model is employed. But other models should also be applicable to model the deformation of the band. We automates the control point selection by using the scale invariance feature transformation (SIFT) tissue feature searching (see next subsection for details). Roughly, 300 control points are selected based on the prominent tissue features.

The detailed description of the TPS transformation can be found in Ref. 8. For two-dimensional (2D) images, a weighting vector $W=(w_1,w_2,\ldots,w_n)$ and the coefficients a_1,a_u,a_v are computed from a series of matrices which are constructed using n pairs of selected control points in the fixed image (x_i,y_i) and in the moving image (u_i,v_i), respectively. The function transforming a pixel coordinate in the moving image to a new coordinate in the fixed image is defined as

$$f(u',v') = a_1 + a_u u + a_v v + \sum_{i=0}^{n} w_i U(|p_i - (u,v)|), \tag{1}$$

where p_i is the control points coordinate in the fixed image and U is a basis function to measure the distance.

II.D. SIFT

The feature-based deformable registration is an essential part of the proposed contour mapping process. Here, we automate the control point selection by using the SIFT-based tissue feature searching. Because of the efficient use of *a priori* system knowledge, the approach greatly enhances the robustness of the narrow band warping algorithm.

The SIFT method was introduced by Lowe to characterize the local tissue features. The method utilizes both image intensity and local gradient information to characterize the neighborhood property of a point.[9] The algorithm includes scale-space extrema detection, control point localization, orientation assignment, and control point descriptor. In 2D cases, for example, the method uses the orientation histograms of the four quadrants surrounding a point (containing 64 pixels) to characterize the inherent tissue feature of the point (see Fig. 3). To obtain the histogram for a quadrant, as illustrated in Fig. 3, the gradient of each of the 16 pixels in a quadrant is computed. An eight-bin histogram, with first bin representing the number of pixels whose gradients fall between 0° and 45°, and so forth, is then constructed. For illustration, the histogram of each of the four quadrants is displayed schematically in the right panel of Fig. 3 as an eight-vector plot. In total, 32 vectors are calculated in 2D case. In extending the SIFT method from 2D to three dimensional (3D), total of 192 vectors are needed. These vectors

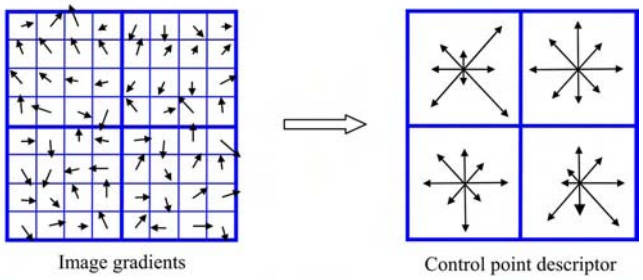

FIG. 3. A sketch of orientation histogram in SIFT method. The gradient of each of the 16 pixels in a quadrant is computed. An eight-bin histogram, with first bin representing the number of pixels whose gradients fall between 0° and 45°, and so forth, is then constructed. The histogram of each of the four quadrants is displayed schematically in the right panel as an eight-vector plot.

represent the local feature and serve as a signature of the point. The SIFT descriptor is considered as one of the most effective descriptors currently available.[10,11]

Theoretically, the SIFT descriptor can be computed for each voxel in an image. However, this is computationally expensive. The commonly used sampling strategy is to compute the descriptor every 2–3 voxels in x, y, and z directions. After the SIFT descriptors are computed in both input images, the points having the most similar SIFT descriptors in the two images are then identified. For a given point, indexed by n, in the pCT image, the least-squares difference of the SIFT descriptor of the point and that of a potential association point n' in the CBCT, $S_{n,n'}$, is first computed according to

$$S_{n,n'} = \sqrt{\sum_{\alpha=1}^{k} |(\nabla I_n)_\alpha - (\nabla I_{n'})_\alpha|^2}, \tag{2}$$

where I represents the image intensity. α indexes the bins of the SIFT histogram of a point and the summation over α runs from 1 to 32 for the 2D case, and 1 to 192 for the 3D case. Typically, about 1000 SIFT descriptors n,n' are computed in the narrow band in the pCT and CBCT, respectively. It is unnecessary to determine $S_{n,n'}$ for all possible combinations n,n', which may dramatically increase the calculation time. We use a specific search radius to control the number of $S_{n,n'}$ calculation. The mapping results are more accurate with larger search radius, however, the calculation time of SIFT mapping becomes longer. After $S_{n,n'}$ is computed, two points n'_1 and n'_2 that have the least histogram difference with point n are identified. If the ratio (for convenience, the ratio is referred to as the κ ratio hereafter) of these two values is less than 80%, the point that has the least S value is chosen tentatively as the correspondence of the point n, otherwise, no association is made for the point. The κ ratio varies between 0 and 1 and is an empirical measure of feature correspondence between two images. The lower the κ ratio, the "stronger" the association of the two feature points on pCT and CBCT. Because of the inherent difference in the textures of the involved organs, the determination of the κ ratio may be organ specific. Typically, it is determined by a tradeoff be-

tween the number of associated point pairs and the reliability of the associations. For a bone, the feature is clear and hundreds point pairs can be associated under a threshold of 50%. On the other hand, for the rectum, the feature is not as obvious as bone. If we still use this low κ ratio, the number of association pairs may be very limited. In this situation, a higher threshold, say 80%, is usually used to increase the number of associated point pairs.

To further increase the accuracy of feature point association, a bidirectional mapping strategy is developed based on the fact that if a point in the pCT is mapped correctly to the CBCT, it will be default to be mapped back to the original point in the pCT when an inverse map is applied to the corresponding point in the CBCT. Therefore, after the original association of feature points as described above, the mapped points in CBCT are inversely coregistered to the pCT. If the correspondence still exists, the associated point pair is labeled a match. Otherwise, they are considered as a mismatch and deleted from the list of correspondence points. Upon the association of the feature points, the associated points are employed as control points. The control point in pCT and CBCT corresponds each other, thus the numbers of control points in the two input images are the same. It was noticed that, when the CBCT region of interest (ROI) is expanded, the increase of feature point generation does not affect the control point association and final contour mapping. The coordinates of an arbitrary point on the contour in CBCT are obtained by interpolating the displacement vectors of the control points using TPS transformation after the control point association is established.

II.E. Evaluation of the models using digital phantom and existing patient data

The performance of the above model is evaluated by a number of 2D digital phantoms and archived clinical cases. In the digital phantom experiments, two deformations are introduced. A virtue of this approach is that the "ground truth" solutions exist and the transformation matrices are known, thus making the evaluation straightforward. The mathematical transformations used to deform the phantom are generated using a formula[12]

$$x'(x,y) = (1 + b\cos m\theta)x, \tag{3}$$

$$y'(x,y) = (1 + b\cos m\theta)y. \tag{4}$$

Here, $\theta = \tan^{-1} y/x$. Two parameters, m and b, are used to characterize a deformation. Generally, they describe the complexity and magnitude of a deformation, respectively. The contour outlined in the original image is then mapped to the deformed image. The accuracy of the contour mapping calculation is assessed by comparing directly with the deformable mapping from the known transformation matrix.

Contour propagation from pCT to CBCT is studied by using three prostate cancer patients and two rectal cancer cases. The pCT is acquired with a GE Discovery-ST CT scanner (GE Medical System, Milwaukee, WI) approximately two weeks prior to the initiation of the radiotherapy. The on-treatment CBCT images are acquired using the Varian Trilogy™ (Varian Medical Systems, Palo Alto, CA). Each slice of pCT or CBCT is discretized into 512×512 voxels. The images are transferred through DICOM to a high-performance personal computer with a Xeon (3.6 GHz) processor for image processing. The manually outlined contours in the pCT images are mapped to CBCT images using the proposed technique. For the cases studied here, the accordance between the rectal volumes after deformable registration and the manually segmented rectum is employed to assess the success of the proposed algorithm.

To quantitatively evaluate the result of contour propagation, the accordance value between the automapped contour and manually outlined contours were calculated. In general, suppose A and B are two contours, the accordance value r is defined as

$$r = \frac{V_A \cap V_B}{V_A \cup V_B}, \tag{5}$$

here, V is the containing volume of A or B.

III. RESULTS

III.A. 2D digital phantom experiment

The proposed algorithm is first tested using a 2D digital phantom [Fig. 4(a)] with two intentionally introduced deformations of the image shown in Figs. 4(b) and 4(c), respectively. The rectal contour is manually outlined and shown in Fig. 4(a). The deformation shown in Figs. 4(b) and 4(c) are obtained by setting the parameters b and m in Eqs. (3) and (4) to ($b=2$, $m=2$) and ($b=2$, $m=3$), respectively. The curves close to the interior surface of the rectum in Figs. 4(b) and 4(c) represent the automapped contour. For comparison, the original contour in Fig. 4(a) is also mapped rigidly to Figs. 4(b) and 4(c). Overall, the mapped contours can capture the main features of the two dramatic deformations, and conform to the boundary of the rectum in both cases.

In obtaining the result shown in Fig. 4(b), a total of 200 control points were identified by the bidirectional SIFT calculation as described in method. Note that the bony structure in the image has been excluded in this calculation by setting an intensity threshold of 300 CT number. In this way, any unphysical bony structure deformation is avoided. For clarity, a selection of the SIFT-identified control point associations are displayed in Fig. 5. The superior contour represents the superior surface of narrow band. The total number of control points identified here are far more than that commonly used in TPS calculation,[13] allowing an improved deformable warping of the narrow band. We should notice that the control points 2, 3, 4, 5, and 9 in Fig. 5 are relatively far away from the rectum wall compared to control points 6 and 10. Since the TPS interpolation is used after SIFT mapping, every control point including points 2, 3, 4, 5, and 9 will affect the deformable warping and therefore the contour shape, although the weights of points 2, 3, 4, 5, and 9 are smaller than points 6 and 10. The displacement field derived by using TPS method is shown in Fig. 6(a). For comparison,

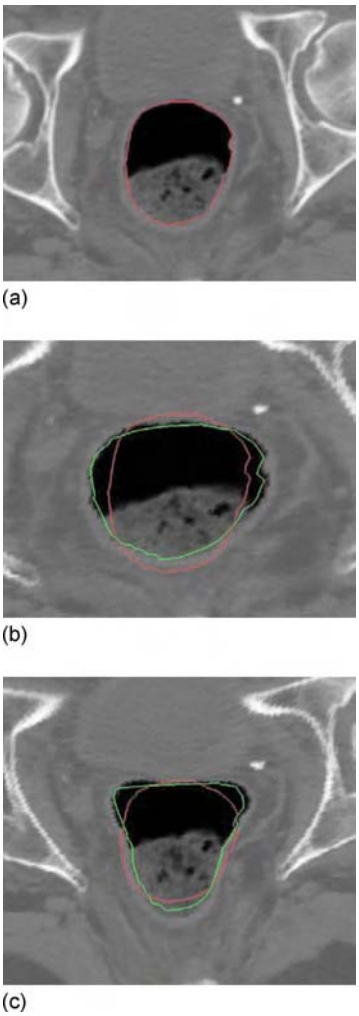

FIG. 4. Rectal contour propagation from the 2D pCT slice to two dramatically deformed images. (a) Original contour, (b) and; (c) its optimal mapping in the two deformed images.

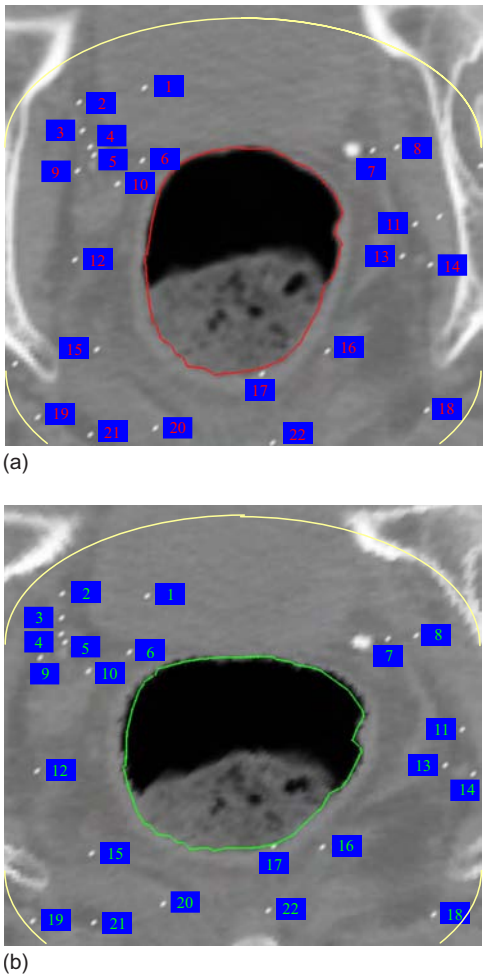

FIG. 5. Control points in the 2D contour mapping.

the known displacement field from Eqs. (3) and (4) is plotted in Fig. 6(b). The subtraction between the TPS-derived displacement field and the known field is shown in Fig. 6(c). It is found that the average deviation of the SIFT-TPS displacement from the known solution is less than 1.2 mm.

III.B. Clinical case study

The contour propagation study from pCT to CBCT for the first prostate case is presented in Fig. 7. The top row shows the pCT image with manually outlined contours. The automapped contours overlaid on the CBCT are displayed in the bottom row. For comparison, the manually outlined contours on the CBCT are also plotted in the bottom row. As mentioned in Sec. I, the propagation of rectum wall is often complicated by the fact that the physical one-to-one correspondence may not exist due to the addition or subtraction of some contents within the rectum. Figure 8 exemplifies this and shows that the rectal filling at the time of CBCT acquisition is quite different from that of pCT. As can be intuitively conceived, this image content change could severely reduce the performance of a conventional deformable registration.[14] The narrow band approach described in this work circumvents the problem by excluding the rectal volume affected by the rectum/bladder filling. Accuracy was evaluated by comparison with manually outlined contours on the CBCTs.[15–17] It is clear that the mapped contours closely conform to the rectal wall change. The accordance between the rectal volume extended by the automapped contour and the manually segmented rectal volume was found to be more than 90%.

In practice, rectal volume motion and deformation can cause large uncertainties pertaining to the adequacy of actual dose delivered to the gross tumor volume as well as to the surrounding normal structures. This issue has been a major obstacle in the implementation of IMRT in rectal cancer. In Fig. 8 six axial pCT and CBCT images of a rectal cancer patient acquired in an interval of two weeks are shown. Large target volume motion and deformation are observed from Fig. 8. The rectal volume in the pCT is found to be three times more than that of the rectal volume in the CBCT and thus represents a challenging situation for any deformable model. The rectal contours are manually outlined in the pCT and mapped to the subsequent CBCT using the proposed method. The first and second rows of Fig. 8 show six

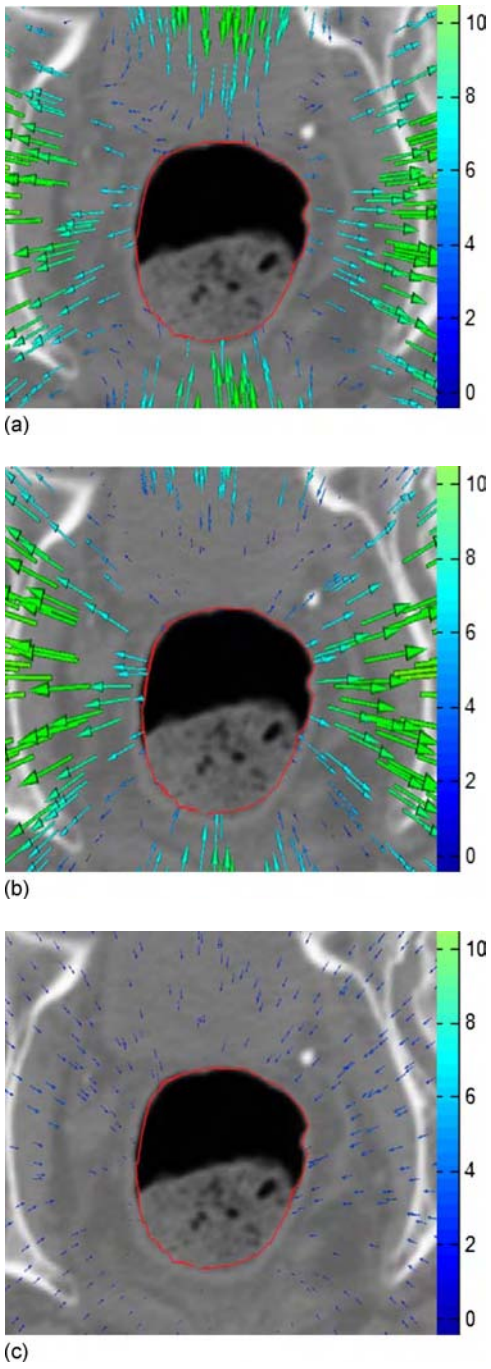

FIG. 6. Displacement fields. (a) TPS-derived displacement field for the 2D digital phantom study; (b) intentionally introduced displacement field; and (c) subtraction of TPS derived and the known displacement fields.

axial slices of the pCT with manually outlined contours. The results of contour propagation from the pCT to the CBCT are shown in the third and fourth rows of Fig. 8. As the same as in Fig. 7 the manually outlined contours on the CBCT are also plotted. The accordance between the rectal volume extended by the automapped contours and the manually segmented rectal volume was found to be more than 95%. The rectal deformations in Fig. 8 are quite large and thus present challenges to any deformable model or contour mapping technique. It is impressive that a simple approach with a narrow band and SIFT descriptor can capture the main feature of the rectal contour and help to find the correspondence contours in the CBCT images.

To further examine the performance of the proposed technique, the method was also applied to three additional patients (Fig. 9). The automapped contours are plotted together with the manually outlined contour on the CBCT. For comparison, the original contours on pCT are also mapped rigidly to the CBCT. The accordance values between the pCT and CBCT contours, as well as between the automapped and manually segmented CBCT contours for these three patients are listed in Table I. In these cases, the accordance values are increased from around 75% to over 90% after contour mapping. The influence of the κ ratio on the contour propagation is illustrated by the data listed in Table II, where the accordance values for a few different κ ratios for the three patients are shown. The accordance reached its peak value when the κ ratio is between 0.8 and 0.9 for all these three cases. When the κ ratio is lower than 0.8, the accordance decreases with the decrease of the κ ratio because less control points are selected. The accordance also decreases with the increase of the κ ratio for the κ ratio higher than 0.9. The accordance value is stable for κ ratios between 0.8 and 0.9. The data also indicate that the κ ratio is generally organ specific and is insensitive for different patients.

IV. DISCUSSION

In this work, an effective feature-based rectal contour mapping algorithm has been described. An indispensable step toward online or offline adaptive replanning with consideration of the patient's dose delivery history and on-treatment anatomy is the expedite organ segmentation of CBCT images. While this task is, in principle, achievable using deformable registration of the pCT and CBCT images, the accuracy of the registration and therefore the contour mapping, is often adversely affected by the presence of image contents in one image that do not have correspondence in the other image. The propagation of rectum wall is an example of this. For prostate, rectal, or gynecological cancer patients for example, the presence and absence of bowel gas can vary daily. Coregistering an empty rectum without bowel gas to a rectum filled with bowel gas (or vice versa) using any deformable model could be problematic and large errors could occur.

We describe a regional contour propagation algorithm taking into account possible organ deformation and anatomic changes. Because the narrow band contains only the image features outside the rectum, this method is not affected by the rectum filling changes. The use of SIFT descriptor enhances our ability to find the correspondence of the narrow band because of the effective utilization of image intensity and gradient information. In contrast to the conventional intensity-based image registration, which only uses intensity information of the voxels, the feature-based registration extracts information regarding image structure, including shape, texture, etc. Therefore, the feature-based image regis-

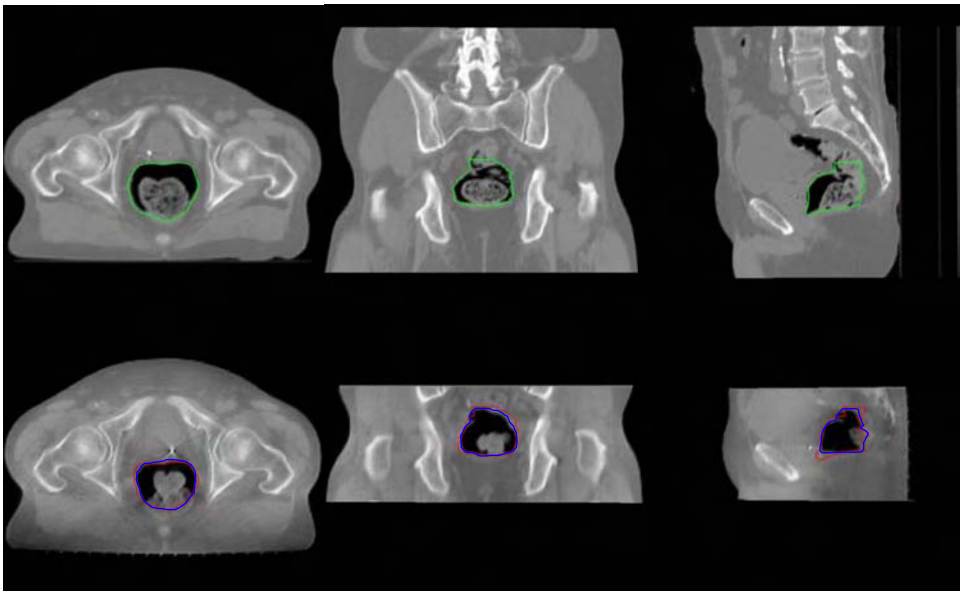

FIG. 7. 3D contour mapping for the rectum of a man with prostate cancer. The top row is the three transactions in the planning CT image, the bottom row is corresponding transactions in the CBCT image. The left column is the axial plane, the middle column is the coronal plane, and the right column is the sagittal plane.

tration is generally more effective in correctly identifying corresponding voxels compared to the intensity-based image registration.

In this study, a bidirectional SIFT descriptor is employed to examine the reliability and robustness of the calculations. The bidirectional mapping further enhances the degree of success of a contour propagation algorithm. It is useful to note that the bidirectional mapping is a necessary (but not sufficient) test. In a rare but possible situation, the bidirectional mapping may not be able to find an error occurred in the contour mapping process.

Because the iterative procedure in the B-spline is not needed in our method, the calculation speed is at least ten times faster than B-spline registration. Typically the total calculation time of SIFT-TPS mapping with about 1000 SIFT descriptors is less than 2 min. Several parameters influence

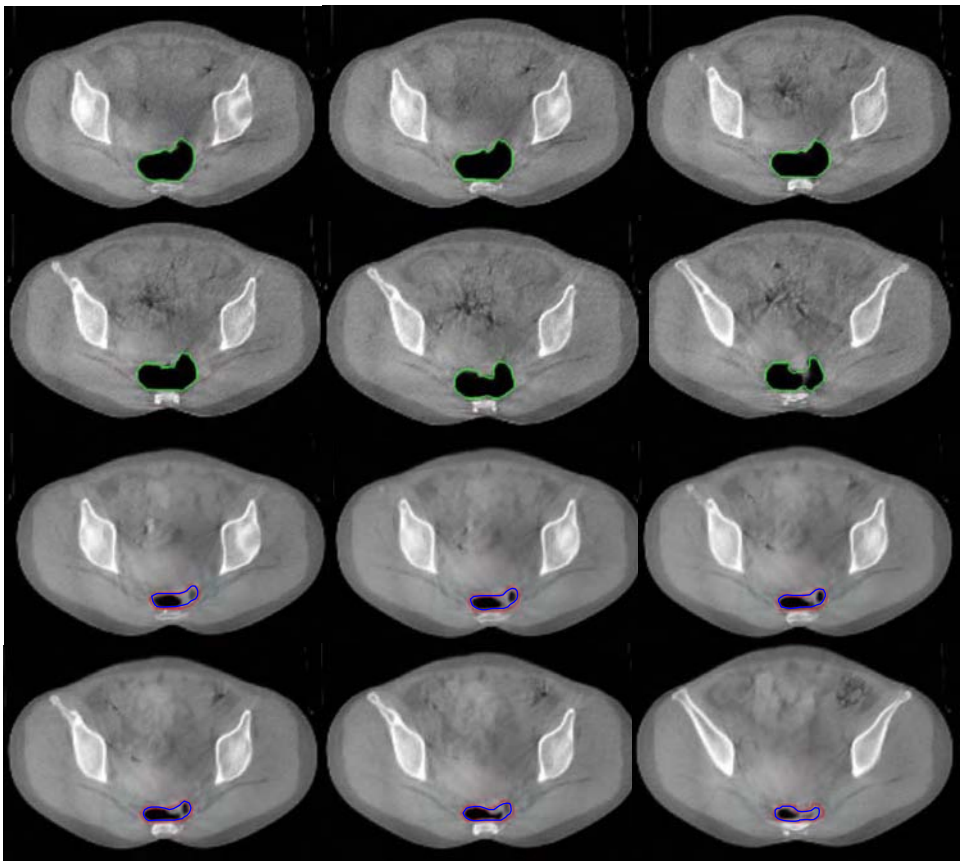

FIG. 8. Rectal contour mapping for a rectal cancer case. The first and second rows show six axial slices in the pCT image. The third and fourth rows are the corresponding slices in the CBCT image.

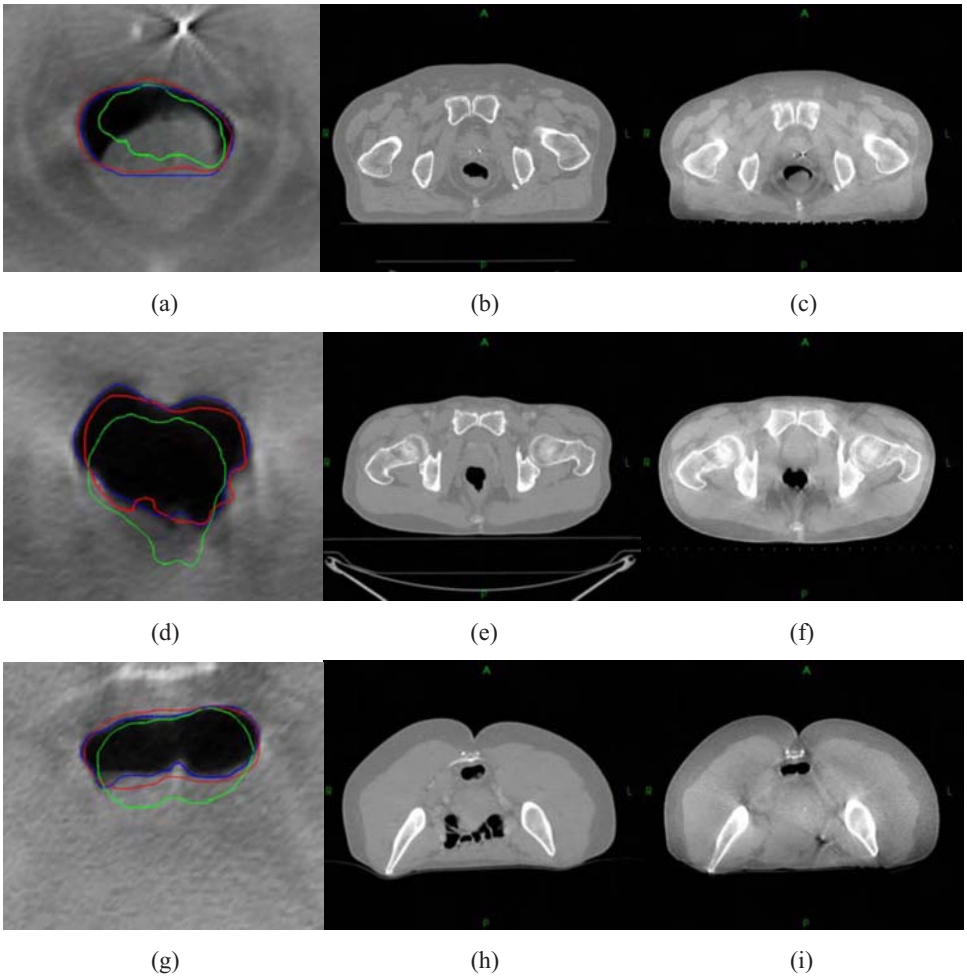

FIG. 9. Automatic contour propagation for three additional patients.

calculation time. For example, larger narrow-band will result in longer calculation times. The number of control points also affects calculation time quite nonlinearly as well. For most cases, 300 control points are enough for accurate contour mapping. Due to the tight clinical timeframes (especially for real-time adaptive schemes), 1 or 2 min calculation time allows the use of the contour mapping tool between acquiring the verification images and delivering the dose fraction for online corrections.[18]

In some cases, no corresponding feature is found by SIFT in a certain area close to the rectal wall. For instance, no control point was found in the upper part of Fig. 5. Since no large local deformation was in these regions, the result was all right. However, it would have lead to larger errors in case of large deformations plus low feature density, which may happen in smooth soft tissues. We will improve it in our future work.

One of the practical concerns is that the relatively low quality of CBCT images may influence the accuracy of image registration and thus the contour mapping. Paquin *et al.* quantitatively studied the influence of different types of noises on deformable registration and found that the accuracy of image registration does not depend on the global noise unless the noise reaches a certain threshold value.[19] Murphy *et al.* also demonstrated that noise levels in cone-beam CTs that might reduce manual contouring accuracy do not reduce image registration and automatic contouring accuracy.[20]

TABLE I. Accordance values between the pCT and CBCT contours, as well as between the auto-mapped and manually segmented CBCT contours for three patients.

	Patient 1	Patient 2	Patient 3
Accordance values between pCT and CBCT contours (%)	73.7	76.5	76.3
Accordance values between auto-mapped and manually segmented CBCT contours (%)	93.3	91.3	91.4

TABLE II. Accordance values between the auto-mapped and manually segmented CBCT contours for different κ-ratios for three patients.

κ ratio	0.7	0.75	0.8	0.85	0.9	0.95
Patient 1 (%)	81.5	88.4	91.6	92.6	93.3	82.9
Patient 2 (%)	76.3	82.1	91.3	88.9	85.8	79.1
Patient 3 (%)	67.5	86.6	88.3	88.4	91.4	62.6

Deformable model plays an important role in automated contour propagation. Numerous approaches have been developed for different applications. Most popular deformable registration methods for medical images include the thin plate splines (TPS),[8] B-splines,[21,22] and finite element method (FEM).[23] TPS is less sensitive to noise because of its global calculation nature.[24] It relies on the use of homologous control points in the two input image sets to be coregistered. Control points are manually selected for many TPS applications.[13,25,26] This may introduce interuser variability and is a major source of error. Malsch *et al.* presented an automatic block matching method,[18] which is similar to the control volume based approach proposed by Schreibmann and Xing.[27] Kim *et al.* presented an automated TPS, where an arbitrary set of control points is supplied initially and then is iteratively repositioned until the resulting warp optimizes some measure of registration.[28–30] The convergence of the iterative calculation is slow because each control point influences the transformation in a global fashion. An alternative is to use B-splines. In contrast to TPS, which allows arbitrary configurations of the control points, B-spline requires a regular mesh of control points with uniform spacing. Unlike spline-based registration methods, FEM models the deforming image as an elastic body subject to external forces which drive the deformation and internal forces (stresses) which impose smoothness constraints.[31,32] FEM may fail to model highly localized deformations, since the deformation energy caused by stress increases proportionally with the strength of the deformation.[33]

V. CONCLUSION

Large interfractional patient setup uncertainty and anatomy changes have been reported in numerous studies and are widely recognized as one of the major limiting factors for maximum exploitation of modern radiation therapy techniques such as IMRT and IGRT. The advent of onboard volumetric imaging devices promises to improve the situation by providing valuable 3D (or even possibly four-dimensional) geometric data of the patient in the treatment position and allows for the adaptive modification of treatment plan during a course of treatment.

In this work, an effective feature-based rectal contour mapping algorithm has been described. The method yielded satisfactory mapping for both digital phantom and clinical cases. It is impressive that the algorithm is able to successfully map the contours from pCT to CBCT even for some very challenging cases in which the deformation and/or image content change are dramatic. The two salient features of the described algorithm are: (1) the use of inherent tissue feature for control point selection as *a priori* knowledge for deformable registration; and (2) limiting the ROI to exclude the volume inside the rectum and focusing on the adjacent neighborhood of the rectal contour. The algorithm should be extendable for contour propagation of organs with similar features, such as the bladder and stomach.

ACKNOWLEDGMENTS

This work was supported in part by grants from the Department of Defense (W81XWH-06-1-0235 and W81XWH05-1-0041) and National Cancer Institute (1R01 CA98523 and CA104205).

[a]Electronic mail: lei@reyes.stanford.edu

[1]L. Xing *et al.*, "Overview of image-guided radiation therapy," Med. Dosim. **31**, 91–112 (2006).
[2]A. de la Zerda, B. Armbruster, and L. Xing, "Formulating adaptive radiation therapy (ART) treatment planning into a closed-loop control framework," Phys. Med. Biol. **52**, 4137–4153 (2007).
[3]P. Lee *et al.*, "Image-guided radiation therapy (RT) for rectal cancer using cone beam CT (CBCT)," Int. J. Radiat. Oncol., Biol., Phys. **66**, S276 (2006).
[4]M. Foskey *et al.*, "Large deformation three-dimensional image registration in image-guided radiation therapy," Phys. Med. Biol. **50**, 5869–5892 (2005).
[5]S. Gao *et al.*, "A deformable image registration method to handle distended rectums in prostate cancer radiotherapy," Med. Phys. **33**, 3304–3312 (2006).
[6]L. Ibanez, W. Schroeder, and L. Ng, "ITK Software Guide," Kitware, Inc., 2003.
[7]W. Schroeder, K. Martin, and B. Lorensen, The Visualization Toolkit: An Object-Oriented Approach To 3D Graphics, 3rd ed., 2003.
[8]F. L. Bookstein, "Principal warps: Thin plate splines and the decomposition of deformations," IEEE Trans. Pattern Anal. Mach. Intell. **11**, 567–585 (1989).
[9]D. G. Lowe, "Object recognition from local scale-invariant features," Proc. of the International Conference on Computer Vision, Corfu, 1999.
[10]K. Mikolajczyk and C. Schmid, "A performance evaluation of local descriptors," IEEE Trans. Pattern Anal. Mach. Intell. **27**, 1615–1630 (2005).
[11]G. Wu, F. Qi, and D. Shen, "A general learning framework for non-rigid image registration," MIAR, 2006, pp. 219–227.
[12]W. Lu *et al.*, "Fast free-form deformable registration via calculus of variations," Phys. Med. Biol. **49**, 3067–3087 (2004).
[13]J. Lian *et al.*, "Mapping of the prostate in endorectal coil-based MRI/MRSI and CT: A deformable registration and validation study," Med. Phys. **31**, 3087–3094 (2004).
[14]L. E. Court and L. Dong, "Automatic registration of the prostate for computed-tomography-guided radiotherapy," Med. Phys. **30**, 2750–2757 (2003).
[15]E. Schreibmann, G. T. Chen, and L. Xing, "Image interpolation in 4D CT using a BSpline deformable registration model," Int. J. Radiat. Oncol., Biol., Phys. **64**, 1537–1550 (2006).
[16]W. Lu *et al.*, "Automatic re-contouring in 4D radiotherapy," Phys. Med. Biol. **51**, 1077–1099 (2006).

[17]T. Zhang *et al.*, "Automatic delineation of on-line head-and-neck computed tomography images: toward on-line adaptive radiotherapy," Int. J. Radiat. Oncol., Biol., Phys. **68**, 522–530 (2007).
[18]U. Malsch *et al.*, "An enhanced block matching algorithm for fast elastic registration in adaptive radiotherapy," Phys. Med. Biol. **51**, 4789–4806 (2006).
[19]D. Paquin, L. Xing, and D. Levy, "Multiscale deformable registration of noisy medical images," Math. Biosci. Eng. **5**, 125–144 (2008).
[20]M. J. Murphy *et al.*, "How does CT image noise affect 3D deformable image registration for image-guided radiotherapy planning?," Med. Phys. **35**, 1145–1153 (2008).
[21]M. Staring, S. Klein, and J. P. W. Pluim, "A rigidity penalty term for nonrigid registration," Med. Phys. **34**, 4098–4108 (2007).
[22]E. Schreibmann *et al.*, "Image interpolation in 4D CT using a B spline deformable registration model," Med. Phys. **32**, 1924 (2005).
[23]R. Alterovitz *et al.*, "Registration of MR prostate images with biomechanical modeling and nonlinear parameter estimation," Med. Phys. **33**, 446–454 (2006).
[24]S. Roberts and L. Stals, "Discrete thin plate spline smoothing in 3D," Annal. Chim. **45**, C646–C659 (2004).
[25]B. Fei, C. Kemper, and D. L. Wilson, "A comparative study of warping and rigid body registration for the prostate and pelvic MR volumes," Comput. Med. Imaging Graph. **4**, 267–281 (2003).
[26]M. M. Coselmon *et al.*, "Mutual information based CT registration of the lung at exhale and inhale breathing states using thin-plate splines," Med. Phys. **31**, 2942–2948 (2004).
[27]E. Schreibmann and L. Xing, "Image registration with auto-mapped control volumes," Med. Phys. **33**, 1165–1179 (2006).
[28]B. Kim *et al.*, "Mutual information for automated unwarping of rat brain autoradiographs," Neuroimage **5**, 31–40 (1997).
[29]C. R. Meyer *et al.*, "Demonstration of accuracy and clinical versatility of mutual information for automatic multimodality image fusion using affine and thin-plate spline warped geometric deformations," Med. Image Anal. **1**, 195–206 (1997).
[30]K. M. Brock *et al.*, "Automated generation of a four-dimensional model of the liver using warping and mutual information," Med. Phys. **30**, 1128–1133 (2003).
[31]L. Xing, J. Siebers, and P. Keall, "Computational challenges for image-guided radiation therapy: Framework and current research," Semin. Radiat. Oncol. **17**, 245–257 (2007).
[32]H. Lester and S. R. Arridge, "A survey of hierarchical non-linear medical image registration," Pattern Recogn. **32**, 129–149 (1999).
[33]J. V. Hajnal, D. L. G. Hill, and D. J. Hawkes, *Medical Image Registration.* (CRC Press, Boca Raton, 1999).
[34]ITK, http://www.itk.org.
[35]VTK, http://public.kitware.com/VTK/.

IOP PUBLISHING PHYSICS IN MEDICINE AND BIOLOGY

Phys. Med. Biol. **53** (2008) 4533–4542 doi:10.1088/0031-9155/53/17/005

Auto-propagation of contours for adaptive prostate radiation therapy

Ming Chao, Yaoqin Xie and Lei Xing

Department of Radiation Oncology, Stanford University School of Medicine, 875 Blake Wilbur Drive, Stanford, CA 94305-5847, USA

E-mail: lei@reyes.stanford.edu

Received 13 March 2008, in final form 9 June 2008
Published 1 August 2008
Online at stacks.iop.org/PMB/53/4533

Abstract

The purpose of this work is to develop an effective technique to automatically propagate contours from planning CT to cone beam CT (CBCT) to facilitate CBCT-guided prostate adaptive radiation therapy. Different from other disease sites, such as the lungs, the contour mapping here is complicated by two factors: (i) the physical one-to-one correspondence may not exist due to the insertion or removal of some image contents within the region of interest (ROI); and (ii) reduced contrast to noise ratio of the CBCT images due to increased scatter. To overcome these issues, we investigate a strategy of excluding the regions with variable contents by a careful design of a narrow shell signifying the contour of an ROI. For rectum, for example, a narrow shell with the delineated contours as its interior surface was constructed to avoid the adverse influence of the day-to-day content change inside the rectum on the contour mapping. The corresponding contours in the CBCT were found by warping the narrow shell through the use of BSpline deformable model. Both digital phantom experiments and clinical case testing were carried out to validate the proposed ROI mapping method. It was found that the approach was able to reliably warp the constructed narrow band with an accuracy better than 1.3 mm. For all five clinical cases enrolled in this study, the method yielded satisfactory results even when there were significant rectal content changes between the planning CT and CBCT scans. The overlapped area of the auto-mapped contours over 90% to the manually drawn contours is readily achievable. The proposed approach permits us to take advantage of the regional calculation algorithm yet avoiding the nuisance of rectum/bladder filling and provide a useful tool for adaptive radiotherapy of prostate in the future.

(Some figures in this article are in colour only in the electronic version)

1. Introduction

There are increased interests in online/off-line adaptive replanning with consideration of updated patient anatomy information derived from cone beam CT (CBCT) (Yan *et al* 2000, Court *et al* 2005, Ghilezan *et al* 2005, Langen *et al* 2005, Letourneau *et al* 2005, Oldham *et al* 2005, Xing *et al* 2006, Yang *et al* 2007). An indispensable step toward the realization of this type of adaptive replanning is the segmentation of CBCT images (Gao *et al* 2006, Smeenk *et al* 2007). While this task is, in principle, achievable using deformable registration of the planning CT and CBCT images, the accuracy of the registration, and therefore contour mapping, is often adversely affected by the presence of image contents in one image that do not have correspondence in the other image, such as the presence/absence of bowel gas or bladder filling in the pelvic patients (Huang *et al* 2002). A regional contour mapping algorithm is highly desirable for its high computational efficiency and accuracy (Schreibmann and Xing 2005, Chao *et al* 2007, 2008). It also has the potential to improve the robustness of deformable registration because the mapped contours can be utilized as *a priori* system information to facilitate the registration of the two input images.

Large interfraction organ motion exists in radiation therapy of pelvic diseases, such as prostate and cervical cancers (Balter *et al* 1995, Yan and Lockman 2001, Michalski 2003). Adaptive therapy provides a viable option to ensure an adequate dose coverage of the tumor target while sparing the sensitive structures (Yan *et al* 1997, Court *et al* 2005, Wu *et al* 2008). Toward the general goal of clinical implementation of adaptive therapy of prostate cancer, in this work we develop an effective regional contour mapping technique to automatically propagate rectum and prostate contours from planning CT to CBCT. Different from other organs, such as the lungs and liver, the contour mapping here is complicated by two factors: (i) the physical one-to-one correspondence may not exist due to the insertion or removal of some image contents within the rectum (Gao *et al* 2006); and (ii) reduced contrast to noise ratio (CNR) of the CBCT images due to increased scatter in CBCT scanning (Li *et al* 2007). A solution customized to rectum mapping is proposed to overcome the above two limitations and allow us to take advantage of the regional calculation algorithm yet avoiding the nuisance of rectum/bladder filling.

2. Methods and materials

2.1. Software platform

The narrow band contour mapping algorithm was implemented using the NLM Insight Toolkit (ITK) (Ibanez *et al* 2003) and the Visualization Toolkit (VTK) (Schroeder *et al*), which are open source cross-platform C++ software toolkits. They are freely available for research purposes (http://www.itk.org for ITK and http://public.kitware.com/VTK/ for VTK). ITK provides various kinds of basic algorithms for performing registration and segmentation for medical images. The fact that programs contained in ITK are highly extendable makes it an ideal platform for the development of image registration methods. VTK is primarily used for image visualization.

2.2. The contour propagation process

The rectum contour propagation from planning CT to CBCT was carried out in the following sequences: (1) rigid alignment of the planning CT and CBCT images using a rigid registration; (2) construction of a narrow band extended to a region 1–2 cm outside the manually delineated

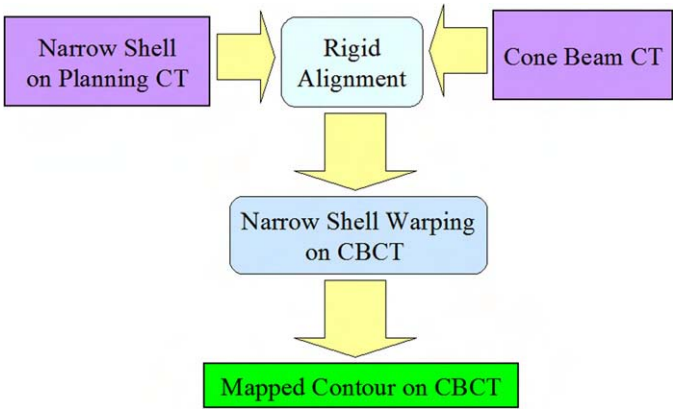

Figure 1. Flowchart of the narrow shell contour mapping process.

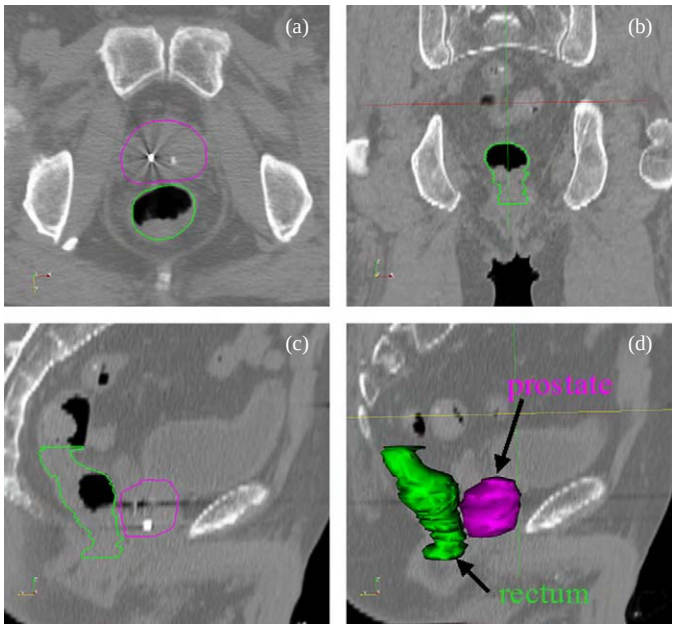

Figure 2. Axial view (a), coronal view (b), sagittal view (c) and volumetric rendering (d) of planning CT of the first patient. Template contours of prostate (magenta) and rectum (green) were superimposed on CT images as indicated.

contours on planning CT; (3) warping of the shell from the planning CT to CBCT. Upon successful warping of the shell, the deformation field in step (3) was utilized to transform the manually segmented contours to the CBCT images. The central idea here is to exclude the volume inside the rectum because its content may change from day to day. Prostate contour can be mapped similarly, but the shell spans the regions both inside and outside the manually segmented prostate. Figure 1 depicts the flowchart of the overall contour mapping process using the narrow shell technique.

The manually delineated region of interest (ROI) contours on planning CT are referred to as the template contours. Figure 2 illustrates the planning CT and the template contours for

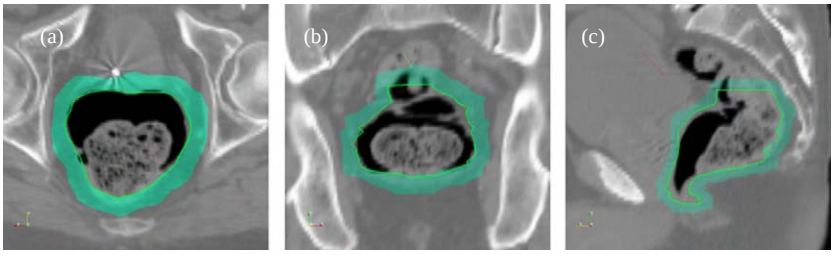

Figure 3. Narrow shell representation of regions of interest (ROIs). The curves represent contours and the shaded regions sketch the narrow shell construct. Illustrated are axial view (a), coronal view (b) and sagittal view (d) of the planning CT image with a single-sided narrow shell surrounding the rectum template contour.

the ROIs such as prostate and rectum for one of the patients studied in this work. A narrow shell was constructed using the method described above for each structure. Typical shapes of the narrow shells for rectum are illustrated in figure 3. The shell width was chosen to be 10 mm in this study.

Upon the construction of shell structure, the shell is warped onto CBCT images by using a BSpline model (Lee *et al* 1996, 1997, Badea *et al* 2008) with a normalized cross correlation metric function defined as

$$f = -\frac{\sum_{i=1}^{N}\left(I_i^A(x)I_i^B(x')\right)}{\sqrt{\sum_{i=1}^{N}\left(I_i^A(x)\right)^2\sum_{i=1}^{N}\left(I_i^B(x')\right)^2}},$$

where $I_i^A(x)$ and $I_i^B(x')$are the intensities of the ith voxels of images A and B, respectively; $x' = Tx$, where T is the transformation matrix. In the narrow shell warping calculation, the input images to the registration software are the narrow shell, $I^A(x)$, and the CBCT image, $I^B(x')$. The narrow shell acts as a shape representation model of an anatomic structure. The task here is to find the deformation, $T(x)$, that maps an arbitrary point x on the fixed image to the corresponding point $x^{'}$ on the moving image (or vice versa) so that the best possible match, as measured by the registration metric, is achieved. The calculation proceeds in an iterative fashion. The limited memory Broyden–Fletcher–Goldfarb–Shannon algorithm (L-BFGS) (Liu and Nocedal 1989) was used for the iterative optimization. The L-BFGS optimizer is well known for its superior performance in dealing with high dimensional problems (Schreibmann and Xing 2005, Schreibmann *et al* 2006). We briefly describe the optimization algorithm in the following.

The BFGS method is derived from Newton's method in optimization which is a class of hill-climbing optimization techniques. It tries to seek the stationary point of a function, where the gradient is 0. Starting from a positive definitive approximation of the inverse Hessian $\mathbf{H}_0$ at $\mathbf{x}_0$, L-BFGS derives the optimization variables by iteratively searching through the solution space. At an iteration k, the calculation proceeds as follows:

(1) determine the descent direction $\mathbf{p}_k = -\mathbf{H}_k \nabla f(\mathbf{x}_k)$;
(2) line search with a step size $\alpha_k = \arg_{\alpha \geqslant 0} \min f(\mathbf{x}_k + \alpha \mathbf{p}_k)$, where α is the step size defined in the L-BFGS software package;
(3) update $\mathbf{x}_{k+1} = \mathbf{x}_k + \alpha_k \mathbf{p}_k$;
(4) compute $\mathbf{H}_{k+1}$ with the updated $\mathbf{H}_k$.

At each iteration a backtracking line search is used in L-BFGS to determine the step size of movement to reach the minimum of f along the ray $\mathbf{x}_k + \alpha \mathbf{p}_k$. During optimization, the iterative

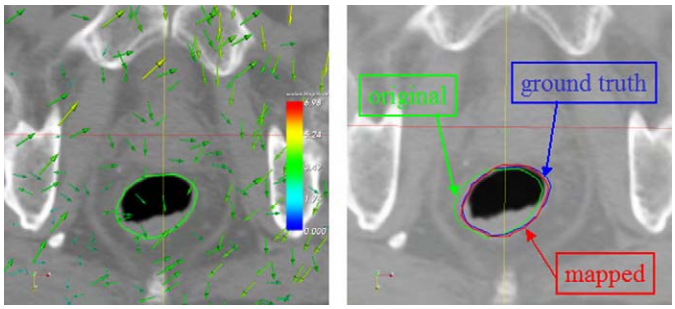

(a) (b)

Figure 4. Digital phantom experiment. (a) Original CT image and manual contour; the vectors overlaid on the image are the displacement field introduced to deform the image. (b) Digitally deformed CT image with ground truth contours and mapped contours. The template contour after rigid registration of the two images is also displayed.

calculation continues until the following stopping criterion is fulfilled:

$$\frac{\|\nabla f(\mathbf{x}_k)\|_2}{\max(1, \|\mathbf{x}_k\|_2)} < \varepsilon,$$

or a pre-set maximum number of iterations is reached. In this study we set $\varepsilon = 10^{-6}$ and the iteration number to 200.

2.3. Evaluation of algorithm performance

Evaluation of a contour propagation algorithm is often a difficult task because of the lack of the ground truth for comparison. A commonly used approach is to visually inspect the mapped contours by a clinician. The use of synthetic images (digital phantoms) is also useful. In this test, the images and existing contours are distorted with known deformation fields, which serves as the ground truth for quantitative evaluation of the model-based contour propagation. In constructing the digital phantom, the deformation field used to deform a planning pelvic CT image was generated as follows. BSpline $8 \times 8 \times 8$ grids were overlaid on the CT image. Three random generators following the Gaussian distribution were called for to provide the displacements for the components of x, y and z at each grid point. The mean value μ of the Gaussian function were all chosen to be 0, but the variances of the three components were set to be

$$\sigma_x^2 = \sigma_y^2 = 5.0 \text{ mm}$$

$$\sigma_z^2 = 2.0 \text{ mm}.$$

Figure 4(a) shows the deformation field overlaid on the original CT image. The manual contour on the original CT image was warped with the same deformation field. This contour served as the ground truth. A comparison of the mapped contour with the ground truth allowed us to quantitatively assess the accuracy of the proposed approach.

2.4. Patient study

The image data sets for five prostate cancer patients were used to further evaluate the proposed technique. The CBCT images were acquired using a Trilogy^{TM} system (Varian Medical

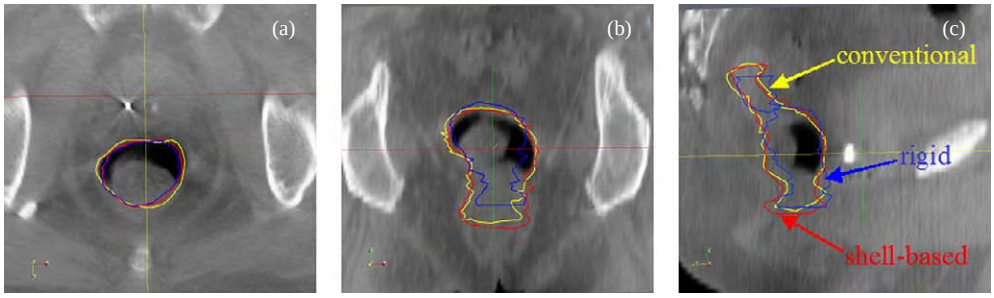

Figure 5. Rectal contours on axial, coronal and sagittal planes obtained with the proposed narrow shell-based (in red) and conventional BSpline approach (in yellow) for the first clinical case. The contours after rigid alignment (in blue) were overlaid on the same CT images.

Systems, Palo Alto, CA). All patient CBCT images were acquired with 90 mA tube current and 120 kV voltage. Under this image acquisition protocol, the dose was around 4cGy for a kV CBCT scan (Wen *et al* 2007). The CBCT image sets for all enrolled patients were reconstructed with a 2.5 mm slice thickness. The planning CT scans were acquired with a GE Discovery-ST CT scanner (GE Medical System, Milwaukee, WI). The size of a CT slice was 512×512. The planning CT images were reconstructed with a 1.25 mm slice thickness for all patients. All CT images were transferred through DICOM to a high-performance personal computer (PC) with Xeon (3.6 GHz) processor for image processing.

3. Results and discussions

3.1. Digital phantom study

The narrow shell constructed based on the planning CT image and the template rectal contour (figure 4(a)) was warped to the digitally deformed images using the technique described above. For convenience, the deformation field used to deform the planning CT images is displayed in figure 4(a) as a vector map. The rectal contour was then extracted upon the successful warping of the shell. The resultant rectum contour is shown in figure 4(b) together with the ground truth contour. The difference between the two sets of contours was found to be insignificant by visual inspection. A quantitative comparison indicated that the mean discrepancy between the two sets of contours was less than 1.3 mm.

3.2. Clinical case study

The proposed approach was applied to five enrolled prostate cancer patients. Figure 5 shows the result of contour propagation for the first clinical case in axial, coronal and sagittal views of CBCT image, respectively. For comparison, the result obtained by registering the whole images using the conventional BSpline method was also superimposed in figure 5. We also observed the convergence behaviors of the two approaches by examining the metric function as a function of the iteration step. Nearly 30 iterations were needed in the conventional registration, whereas only 12 were necessary to obtain converged result in the narrow shell-based approach. In this particular case, both approaches yielded acceptable results because of no substantial change in rectal filling in planning CT and CBCT. The difference between two sets of mapping is well within 2 mm. However, the narrow shell-based calculation was

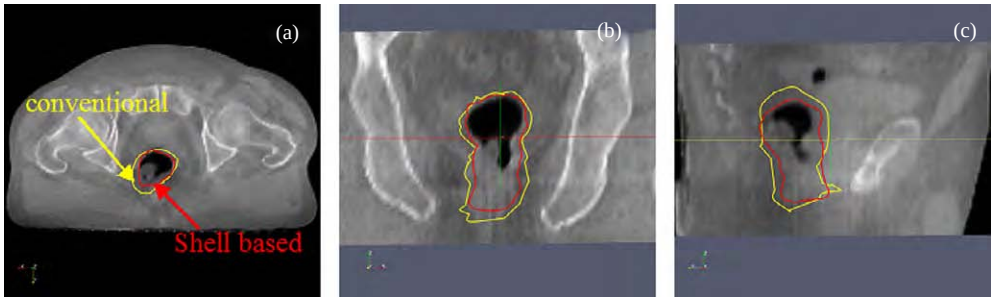

Figure 6. Propagated rectal contour (in red) overlaid on CBCT images in the second patient case. The results based on conventional approach (in yellow) and physician's manual contour were also superimposed on CBCT images as indicated.

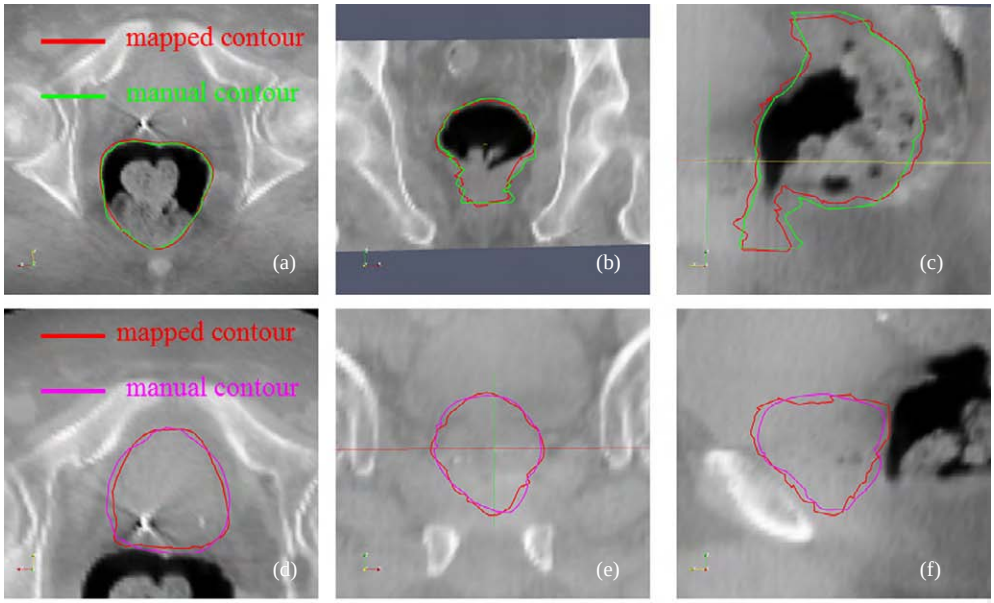

Figure 7. Contour propagation results for the fourth clinical case. (a), (b) and (c) The rectum contours on axial, coronal and sagittal views of CBCT image; (d), (e) and (f) the mapped prostate contours on CBCT images. The manual contours were also overlaid on the same CBCT images.

found to be an order of magnitude more efficient as measured by the computational speed, in addition to the greatly reduced usage of computer memory. Results for the second patient are shown in figure 6. For this patient, however, the rectal fillings in planning CT and CBCT were different and the conventional BSpline approach led to a larger error (mean error ∼8.0 mm) or failed to accurately map the rectum from planning CT to CBCT. The physician's manual contour was also superimposed on the images for visual comparison.

The mapped rectum and prostate contours for another case are displayed in figure 7. Overall, the algorithm performed well for both rectum and prostate. The mean error of the mapped contours was estimated to be around 2 mm for the rectum, and 2.5 mm for the prostate.

The slightly larger error in prostate contour mapping is attributed to the fact that the image contrast in the prostate boundary region was not high. In this case, a careful examination and even a manual modification of the mapped contour by a physician may be needed in clinical operation.

Up to this point, little has been done to register images with the general problem of image content change as studied in this work. Foskey *et al* (2005) and Gao *et al* (2006) studied the topics by using different models. The essence of their work was to introduce 'artificial gas' to mimic the rectal image content or shrink the 'gas' region by deflation. While the introduction of the artificial change could improve the registration accuracy in some special cases, the approaches may fail when the change in rectum content involves solid substances, such as the bowel. A narrow shell model seems to be natural in addressing the issue of image content inconsistence. The technique is conceptually simple, easy to implement and valid for a wide variety of clinical situations.

One of the practical concerns is that the relatively low quality of CBCT images may influence the accuracy of image registration and thus the contour mapping. Paquin *et al* (2008) quantitatively studied the influence of different types of noises on deformable registration and found that the accuracy of image registration does not depend on the global noise unless the noise reaches a certain threshold value. Murphy *et al* (2008) also demonstrated that noise levels in cone-beam CTs that might reduce manual contouring accuracy do not reduce image registration and automatic contouring accuracy.

In principal, the proposed method is also applicable to facilitate the contour warping from planning CT to MV CBCT or images acquired using the tomotherapy devices. However, it is important to emphasize that a prerequisite of any deformable model-based approach is that there are sufficient image features in the neighborhood of the contours to guide the warping of the images. Because of the inherent low contrast of the MV images, the deformable registration of CT and MV CBCT may be challenging. Lu *et al* (2004) have reported successful deformable registration of CT and MV CT images. It will be an interesting subject of future research to examine whether a similar or better accuracy of registration can be achieved when a local deformable registration technique is used for the system.

4. Summary

An automatic contour mapping technique customized for adaptive radiation therapy of prostate cancer has been described. Deformable image registration has been extensively studied. The narrow shell constructed surrounding a ROI contour provides a compact representation of the ROI and greatly facilitates the contour mapping calculation. The chief advantage of the proposed technique is that it is much less prone to the variation in the image contents, which occurs frequently in the pelvic region due to involuntary physiological process. Additionally, the approach is computationally more efficient with lower computer memory consumption and fast computational speed. Both phantom and clinical case studies yielded satisfactory results and suggested that the method may prove to be useful for adaptive radiotherapy of prostate cancer in the future.

Acknowledgments

The authors would like to thank Dr C King, MD, PhD, for his assistance in patient selection and useful discussions of the results. This work was supported in part by grants from the

Department of Defense (W81XWH-08-1-0173, W81XWH-06-1-0235 and W81XWH-05-1-0041) and National Cancer Institute (5R01 CA98523 and 1R01 CA98523).

References

Badea C, Schreibmann E and Fox T 2008 A registration based approach for 4D cardiac micro-CT using combined prospective and retrospective gating *Med. Phys.* **35** 1170–9

Balter J M, Sandler H M, Lam K, Bree R L, Lichter A S and ten Haken R K 1995 Measurement of prostate movement over the course of routine radiotherapy using implanted markers *Int. J. Radiat. Oncol. Biol. Phys.* **31** 113–8

Chao M, Li T, Schreibmann E, Koong A and Xing L 2008 Automated contour mapping with a regional deformable model *Int. J. Radiat. Oncol. Biol. Phys.* **70** 599–608

Chao M, Schreibmann E, Li T, Wink N and Xing L 2007 Automated contour mapping using sparse volume sampling for 4D radiation therapy *Med. Phys.* **34** 4023–9

Court L E, Dong L, Lee A K, Cheung R, Bonnen M D, O'Daniel J, Wang H, Mohan R and Kuban D 2005 An automatic CT-guided adaptive radiation therapy technique by online modification of multileaf collimator leaf positions for prostate cancer *Int. J. Radiat. Oncol. Biol. Phys.* **62** 154–63

Foskey M, Davis B, Goyal L, Chang S, Chaney E, Strehl N, Tomei S, Rosenman J and Joshi S 2005 Large deformation three-dimensional image registration in image-guided radiation therapy *Phys. Med. Biol.* **50** 5869–92

Gao S, Zhang L, Wang H, de Crevoisier R, Kuban D D, Mohan R and Dong L 2006 A deformable image registration method to handle distended rectums in prostate cancer radiotherapy *Med. Phys.* **33** 3304–12

Ghilezan M J *et al* 2005 Prostate gland motion assessed with cine-magnetic resonance imaging (cine-MRI) *Int. J. Radiat. Oncol. Biol. Phys.* **62** 406–17

Huang E, Dong L, Chandra A, Kuban D A, Rosen II, Evans A and Pollack A 2002 Intrafraction prostate motion during IMRT for prostate cancer *Int. J. Radiat. Oncol. Biol. Phys.* **53** 261–8

Ibanez L, Schroeder W and Ng L 2003 *ITK Software Guide* (New York: Kitware Inc.)

Langen K M, Meeks S L, Poole D O, Wagner T H, Willoughby T R, Kupelian P A, Ruchala K J, Haimerl J and Olivera G H 2005 The use of megavoltage CT (MVCT) images for dose recomputations *Phys. Med. Biol.* **50** 4259–76

Lee S, Wolberg G, Chwa K and Shin S 1996 Image metamorphosis with scattered feature constraints *IEEE Trans. Vis. Comput. Graph.* **2** 337–54

Lee S, Wolberg G and Shin S 1997 Scattered data interpolation with multilevel B-Splines *IEEE Trans. Vis. Comput. Graph.* **2** 228–44

Letourneau D, Wong J W, Oldham M, Gulam M, Watt L, Jaffray D A, Siewerdsen J H and Martinez A A 2005 Cone-beam-CT guided radiation therapy: technical implementation *Radiother. Oncol.* **75** 279–86

Li T, Koong A and Xing L 2007 Enhanced 4D cone-beam CT with inter-phase motion model *Med. Phys.* **34** 3688–95

Liu D C and Nocedal J 1989 On the limited memory BFGS method for large scale optimization *Math. Program* **45** 503–28

Lu W, Chen M-L, Olivera G H, Ruchala K J and Makie T R 2004 Fast free-form deformable registration via calculus of variations *Phys. Med. Biol.* **49** 3067–87

Michalski J M 2003 Introduction: locally advanced prostate cancer *Semin. Radiat. Oncol.* **13** 85–6

Murphy M J, Wei Z, Fatyga M, Williamson J, Anscher M, Wallace T and Weiss E 2008 How does CT image noise affect 3D deformable image registration for image-guided radiotherapy planning? *Med. Phys.* **35** 1145–53

Oldham M, Letourneau D, Watt L, Hugo G, Yan D, Lockman D, Kim L H, Chen P Y, Martinez A and Wong J W 2005 Cone-beam-CT guided radiation therapy: a model for on-line application *Radiother. Oncol.* **75** 271–8

Paquin D, Levy D and Xing L 2008 Multiscale deformable registration of noisy medical images *Math. Biosci. Eng.* **5** 125–44

Schreibmann E, Chen G T and Xing L 2006 Image interpolation in 4D CT using a BSpline deformable registration model *Int. J. Radiat. Oncol. Biol. Phys.* **64** 1537–50

Schreibmann E and Xing L 2005 Narrow band deformable registration of prostate magnetic resonance imaging, magnetic resonance spectroscopic imaging, and computed tomography studies *Int. J. Radiat. Oncol. Biol. Phys.* **62** 595–605

Schroeder W, Martin K and Lorensen B 2006 *The Visualization Toolkit: An Objective-Oriented Approach to 3D Graphics* (New York: Kitware Inc.)

Smeenk C, Gaede S and Battista J J 2007 Delineation of moving targets with slow MVCT scans: implications for adaptive non-gated lung tomotherapy *Phys. Med. Biol.* **52** 1119–34

Wen N, Guan H, Hammoud R, Pradhan D, Nurushev T, Li S and Movsas B 2007 Dose delivered from Varian's CBCT to patients receiving IMRT for prostate cancer *Phys. Med. Biol.* **52** 2267–76

Wu Q J, Thongphiew D, Wang Z, Mathayomchan B, Chankong V, Yoo S, Lee W R and Yin F F 2008 On-line re-optimization of prostate IMRT plans for adaptive radiation therapy *Phys. Med. Biol.* **53** 673–91

Xing L, Thorndyke B, Schreibmann E, Yang Y, Li T F, Kim G Y, Luxton G and Koong A 2006 Overview of image-guided radiation therapy *Med. Dosim.* **31** 91–112

Yan D and Lockman D 2001 Organ/patient geometric variation in external beam radiotherapy and its effects *Med. Phys.* **28** 593–602

Yan D, Lockman D, Brabbins D, Tyburski L and Martinez A 2000 An off-line strategy for constructing a patient-specific planning target volume in adaptive treatment process for prostate cancer *Int. J. Radiat. Oncol. Biol. Phys.* **48** 289–302

Yan D, Vicini F, Wong J and Martinez A 1997 Adaptive radiation therapy *Phys. Med. Biol.* **42** 123–32

Yang Y, Schreibmann E, Li T, Wang C and Xing L 2007 Evaluation of on-board kV cone beam CT (CBCT)-based dose calculation *Phys. Med. Biol.* **52** 685–705